Coulomb excitation of the 2^+ state in ^{14}C and the quadrupole deformation of states in ^{194}Pt

by

Christiaan Petrus Brits

Dissertation presented for the degree of Doctor of Philosophy
in the Faculty of Science at Stellenbosch University

Supervisor: Prof. Mathis Wiedeking

Co-supervisor: Dr. Katarzyna Hadyńska-Klęk

                  Prof. Paul Papka

December 2019

Declaration

By submitting this dissertation electronically, I declare that the entirety of the work contained therein is my own, original work, that I am the sole author thereof (save to the extent explicitly otherwise stated), that reproduction and publication thereof by Stellenbosch University will not infringe any third party rights and that I have not previously in its entirety or in part submitted it for obtaining any qualification.

Date: . . . . December 2019 . . . .

Abstract

Coulomb excitation of the 2^+ state in ^{14}C and the quadrupole deformation of states in ^{194}Pt

C.P. Brits

Department of Physics,
University of Stellenbosch,
Private Bag X1, Matieland 7602, South Africa.

Dissertation: PhD. Physics

December 2019

The safe Coulomb excitation experiment of ^{14}C and ^{194}Pt which took place at Florida State University took advantage of the unique beam capabilities, the availability of high-efficiency large volume LaBr$_3$(Ce) detectors and the S3 double sided silicon strip detector. Using the advantageous experimental environment the B(E2: $2_1^+ \rightarrow 0_1^+$) value of the first-excited 2_1^+ state of ^{14}C and the quadrupole deformation of states in ^{194}Pt are investigated.

B(E2: $2_1^+ \rightarrow 0_1^+$) values of neutron-rich even-even C isotopes have been reported up to ^{20}C and provide important information on the evolution of the underlying structural mechanism towards the drip line. They also provide critical constraints for theoretical models as is the case for the experimentally determined B(E2: $2_1^+ \rightarrow 0_1^+$) value for ^{14}C which exhibits persistent inconsistencies with that obtained from theoretical models. The B(E2: $2_1^+ \rightarrow 0_1^+$) value in ^{14}C cannot be reproduced by theoretical models making it indispensable to enhance our theoretical understanding of the C isotopic chain in general. The 2_1^+ state was not observed in the particle-γ data, which may indicate that ^{14}C undergoes single-particle excitation and has a smaller B(E2: $2_1^+ \rightarrow 0_1^+$) value than previously thought.

The A ~ 190 region is very interesting since it has oblate, prolate, γ-soft and spherical shaped nuclei. It is predicted that Pt evolves from prolate deformed $^{180-186}$Pt to γ-soft ^{188}Pt and triaxial ^{190}Pt to oblate $^{192-198}$Pt and finally to spherical ^{204}Pt. From this work, the quadrupole deformation of the 0_1^+, 2_1^+, 4_1^+, 2_2^+, 4_2^+ states are successfully measured with increased accuracy. Additionally it is determined that ^{194}Pt is triaxial oblate which supports the theoretical prediction of the shape evolution in Pt.

Uittreksel

Coulomb opwekking van die 2^+ vlak in ^{14}C en die vierhoekige verforming van vlakke in ^{194}Pt

C.P. Brits

Departement Fisika,
Universiteit van Stellenbosch,
Privaatsak X1, Matieland 7602, Suid Afrika.

Proefskrif: PhD. Fisika

Desember 2019

Die veilige Coulomb-eksitasie eksperiment van ^{14}C en ^{194}Pt aan die Florida State University het voordeel getrek uit die unieke vermoëns, die beskikbaarheid van hoë-doeltreffend groot volume $LaBr_3$(Ce) detektors en die S3 silikon strook detektor. In die voordelige eksperimentele omgewing word 'n poging aangewend om die B(E2: $2_1^+ \rightarrow 0_1^+$) van ^{14}C te meet en die vierhoekige vervorming van vlakke in ^{194}Pt.
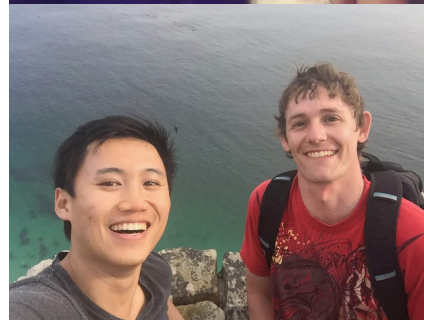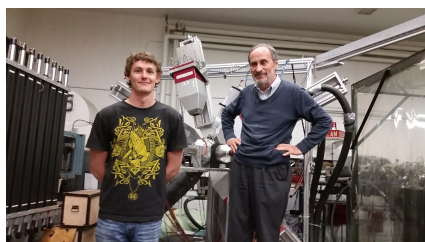
B(E2: $2_1^+ \rightarrow 0_1^+$) waardes van neutronryke gelyke C isotope is aangemeld tot ^{20}C en verskaf belangrike inligting oor die evolusie van die onderliggende strukturele meganisme teenoor die druplyn en kritiese beperkings vir teoretiese modelle. Die eksperimentele vasgestelde B(E2: $2_1^+ \rightarrow 0_1^+$) waarde vir ^{14}C vertoon egter volgehoue teenstrydighede met die waardes verkry uit teoretiese modelle. Die waarde van B(E2: $2_1^+ \rightarrow 0_1^+$) in ^{14}C kan nie gereproduseer word deur teoretiese modelle nie, wat dit onontbeerlik maak om ons teoretiese begrip van C isotopiese ketting in die algemeen te verbeter. Die 2_1^+ staat is nie waargeneem in die deeltjie-γ data nie, wat die moontlikheid uitwys van 'n enkel-deeltjie opwekking en 'n kleiner B(E2: $2_1^+ \rightarrow 0_1^+$) waarde as verwag.

Die A $\sim$ 190 streek is baie interessant aangesien dit afgeplatte, prolate, γ-sag en sferiese kerne bevat. Daar word voorspel dat Pt ontwikkel van die vervormde $^{180-186}$Pt tot γ-sag ^{188}Pt en triaksiaal ^{190}Pt na afgeplatte $^{192-198}$Pt tot uiteindelike spheriese ^{204}Pt. Uit hierdie werk is die vierhoekige vervorming van die 0_1^+, 2_1^+, 4_1^+, 2_2^+, 4_2^+ state suksesvol gemeet met verhoogde akkuraatheid. Daarbenewens word dit vasgestel dat ^{194}Pt triaksiaal afgeplat is wat die teoretiese voorspelling van Pt evolusie ondersteun.

Acknowledgements

"All energy is the same, through its different states and names. Movement creates heat which is also light that waves like sounds which tightens or loosens the atomic bonds of crystals as they hum with strong and weak forces. In mirroring resonance with all of this is magic, the radiant emission of life and death.

This is our role: To weave together those disparate energies. To manipulate and mitigate and, through the prism of our awareness, produce a singular force that cannot be denied. To make of cacophony, symphony. The great machine called Universe is the instrument. We are its tuners." *N.K. Jensin*

Contents

List of Figures

List of Tables

Chapter 1

Introduction

The nucleus has been studied in detail since its discovery by Ernest Rutherford in 1911. Rooms can be filled with what we know about the atomic nucleus; and rooms can be filled with questions on the atomic nucleus. Physics models have been very successful in describing the shape and motion of nuclei in various environments. An atomic nucleus consists of protons and neutrons. These protons and neutrons can move individually or they can move collectively as a group when given energy. This work investigates some specific nuclear properties of 6 protons and 8 neutrons making up a light nucleus: ^{14}C; and 78 protons and 116 neutrons making a heavy nucleus: ^{194}Pt.

^{14}C is widely known to be used in radioactive carbon dating. It makes up ≈ 1 atom per 10^{12} of carbon and has a life time of 5700 ± 30 years [1]. ^{14}C is mainly produced in the atmosphere when cosmic rays interact with ^{14}N. It is also produced in open-air nuclear testing and certain nuclear reactors. It is unstable and undergoes β-decay:

$$^{14}_{6}C \rightarrow\ ^{14}_{7}N + e^{-} + \bar{v}_{e}. \tag{1.1}$$

Platinum is a silver transitional element most famous for use in jewellery and electronics. There is $\approx \frac{5\mu g}{kg}$ platinum in the earth's crust making it a rare metal. Most (80%) of the world's platinum is mined in South Africa [2]. ^{194}Pt is stable and has an isotopic abundance of 32.864%.

The aim of this work is to measure the electric quadrupole transition strength (BE2) for the $2_1^+ \rightarrow 0_1^+$ transition of ^{14}C. Simultaneously, the accuracy of the quadrupole deformation of states in ^{194}Pt can also be improved. This is a pioneering experiment to Coulomb excite a state at 7012 keV. This will also provide a good test for the analysis code GOSIA, which was also never used for a state at 7012 keV.

It is a persistent feature of theoretical models to overestimate the B(E2: $2_1^+ \rightarrow 0_1^+$) value

of ^{14}C. While the transition probability can be calculated from the width measurement of Ref. [3], there are many concerns about the associated lifetime value, see Sec. 1.2 for more detail. The reaction of interest for this work is achieved by bombarding a beam of ^{14}C on a target of ^{194}Pt:

$$^{194}Pt(^{14}C,^{14}C')^{194}Pt'. \tag{1.2}$$

While ^{194}Pt is studied as a by-product in the discussed experiment, it is in an interesting region of nuclear shape transitions where oblate, prolate, γ-soft and spherical shaped nuclei can be observed. It is predicted that Pt isotopes evolve from prolate deformed $^{180-186}$Pt through γ-soft ^{188}Pt, triaxial ^{190}Pt and oblate $^{192-198}$Pt to spherical ^{204}Pt, see Sec. 1.1 for more detail. Due to the fact that ^{194}Pt is well known, it can be used for normalisation purposes of ^{14}C. Simultaneously, a re-measurement of the transition probabilities of ^{194}Pt can be made to lower the uncertainties of the quardrupole deformation of states.

Chapter 1 describes the motivation and objective of the work. Chapter 2 gives an overview of the basic physics and a description of Coulomb excitation theory. Chapter 3 explains the experimental setup and detectors used. Chapter 4 goes over the code developed for the sorting and analysis of the data. Chapter 5 has the general results from all the experiments performed. Chapter 6 contains the GEANT4 line-shape simulation setup and results. Chapter 7 contains the Coulomb excitation analysis results obtained with the GOSIA code. Chapter 8 is the interpretation and conclusion of the work. A brief summary is given in Chapter 9.

1.1 ^{194}Pt

Much of what we know about nuclear structure comes from the electromagnetic interaction. The strong nuclear interaction will determine the distribution and motion of the nucleons. This distribution can then be probed with the much weaker electromagnetic interaction that does not significantly distort the structure of the object under investigation. Any distribution of charges and currents give rise to electric and magnetic fields. These fields can then be used to extract information on the shape of nuclei. The shape of many nuclei is described as non-spherical. This is made apparent by electric quadrupole moments and electromagnetic quadrupole transitions that cannot be explained by single proton transitions [4]. The electric quadrupole moment is one observable that can be measured in a Coulomb excitation experiment to retrieve information on nuclear deformation. This will be elaborated on in Chapter 2.

Nuclear deformation can provide an insight on the properties of nuclei. Filled shells favour a spherical shape while the nucleon-nucleon interaction between nucleons in non-filled shells drives the nuclear shape towards being deformed. The A $\sim$ 190 region is very interesting since it has oblate, prolate, γ-soft and spherical shaped nuclei. γ-soft nuclei are of great interest to the understanding of the underlying mechanisms of deformation [5, 6]. Theoretical work in the N $\sim$ 116 region indicates that nuclei that are transitioning from one shape (e.g. oblate) to another (e.g. prolate) exhibit γ-soft behaviour [5].

A prolate-to-oblate shape transition is predicted to occur at the N $\sim$ 126 shell closure [7]. For platinum isotopes these shape transitions occur for nuclei that are γ-soft. A nucleus is γ-soft when the γ-deformation parameter used to describe the nuclear shape is not well defined. In Yb nuclei it has been shown that the shape evolves from a prolate ^{184}Yb to γ-soft ^{186}Yb, and then to an oblate ^{188}Yb [8]. The ^{194}Pt nucleus has 116 neutrons and that makes it a good candidate for γ-soft behaviour.

Pt nuclei and the surrounding mass region has been the subject of many theoretical studies using:

- Hartree-Fock-Bogoliubov (HFB) with Gogny-D1S and Skyrme SLy4 interaction calculations [5, 6],

- Skyrme Hartree-Fock plus Bardeen-Cooper-Schrieffer (HF + BCS) calculations [8],

- Interactive Boson Model (IBM) [6] calculations and

- Beyond mean field studies (BMF) [7].

A quantitive analysis of the collective character of Pt is shown in Fig. 1.1. The geometrical models for axial rotor, vibrator, γ-unstable (triaxial) are compared to experimental and theoretical results in Fig. 1.1. $^{190-200}$Pt isotopes compare well with a γ-unstable model and ^{204}Pt compares well with a spherical model [7]. ^{204}Pt has N = 126, hence a filled neutron shell, which drives the nucleus towards a more spherical shape.

The potential energy surface (PES) calculations predicted within the BMF model for $^{180-198}$Pt from Ref. [6] are shown in Fig. 1.2 and for $^{190-204}$Pt from Ref. [7] are shown in Fig. 1.3. Here β is the overal deformation parameter and γ is the axial symmetry deformation parameter. These works indicate the evolution of the nuclear shape from prolate deformed $^{180-186}$Pt through γ-soft ^{188}Pt, triaxial ^{190}Pt and oblate $^{192-198}$Pt to spherical ^{204}Pt. One of the nuclei being studied in this work, ^{194}Pt, is predicted to be triaxial oblate.
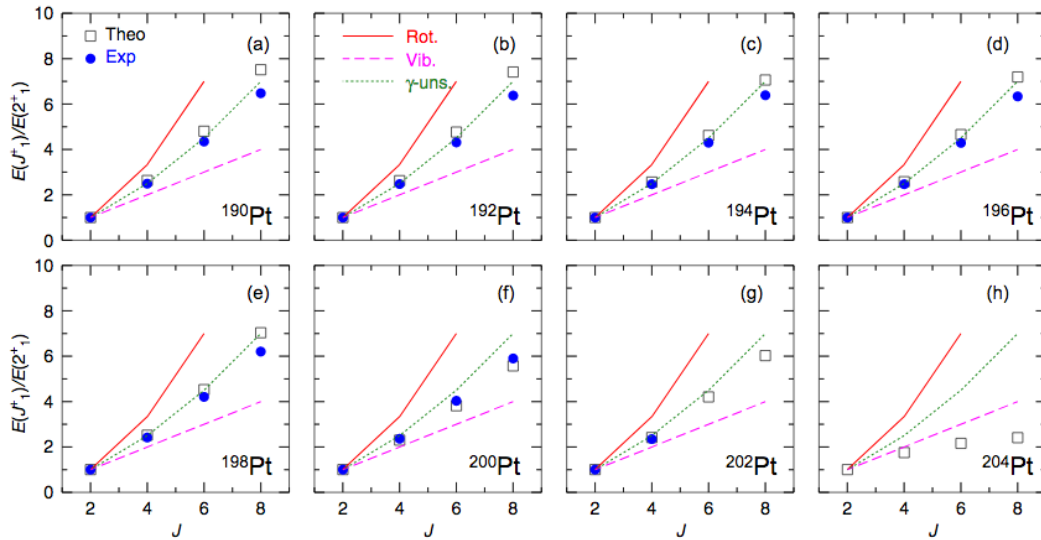
Figure 1.1: The yrast band excitation energies normalised to the 2^+ energies for $^{190-204}$Pt for different spin (J) values. The blue dots are the experimental points and the black boxes are theoretical calculations. The red lines are the theoretical limits for the axial rotor, the magenta lines are the limits for the vibrator model and the green lines are the limits for the triaxial rotor model from Ref. [7].

It is interesting to note that state-of-the-art beyond mean-field calculations have successfully reproduced the collective character of the ground state bands in the osmium isotopic chain [9]. Although much theoretical work has investigated nuclear deformation, a fully microscopic understanding of how nuclear shapes change with nucleon numbers remains a challenge [10].

During a Coulomb excitation reaction both the target and projectile can be excited. It is therefore important that their de-excitation γ-rays not overlap in order for the observed γ-rays to be clearly distinguished during the offline analysis. ^{194}Pt has no known high energies that could overlap with those of ^{14}C. The 2^+_1 state of ^{194}Pt has an excitation energy of 328 keV compared to the excitation energy of 7012 keV for the 2^+_1 of ^{14}C. ^{194}Pt is a good candidate for normalisation purposes for the Coulomb excitation method, since it is well known and has been studied in detail in Refs. [11, 12, 13, 14, 15, 16, 17, 18]. The Coulomb excitation data analysis can be performed using the GOSIA code [19, 20]. This code allows for the extraction of information on the electromagnetic structure of the nucleus of interest. The known information needed as input for the GOSIA code will be presented in Chapter 7 and compared with the results from this work.
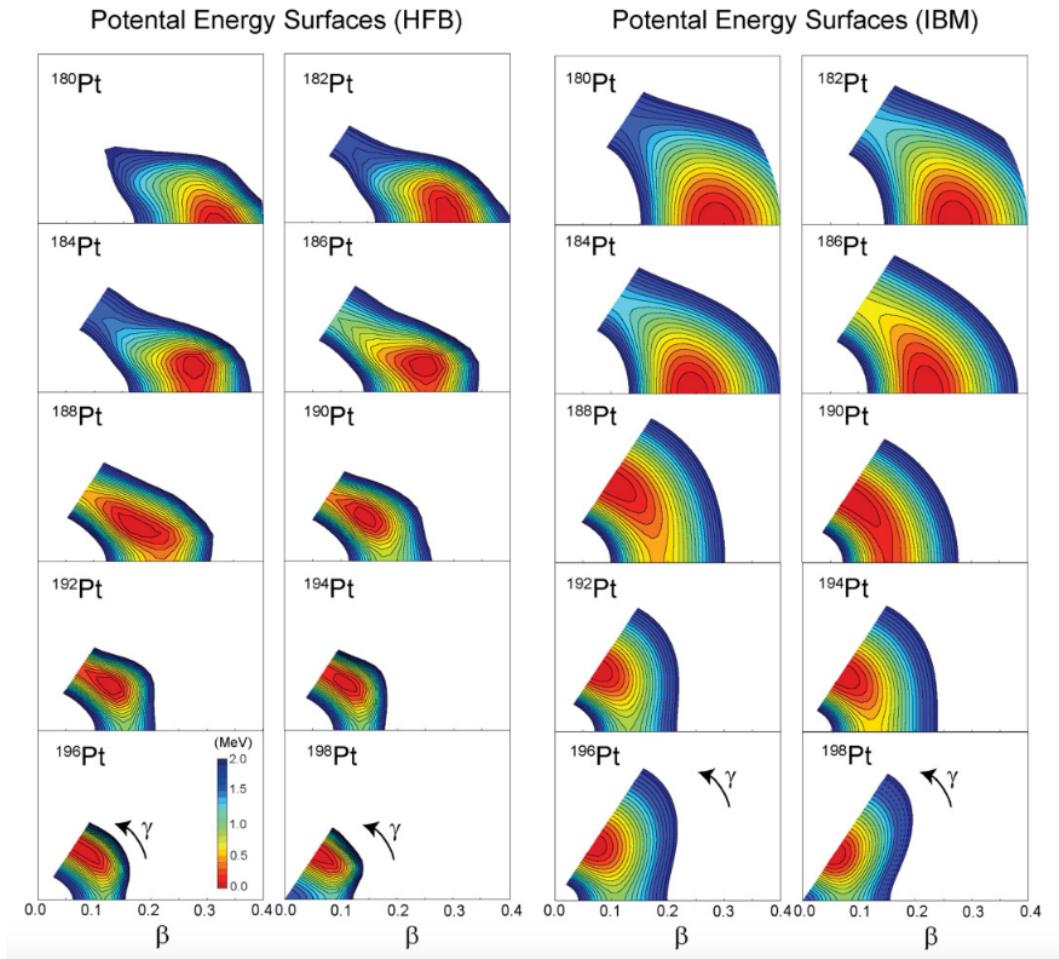
Figure 1.2: Hartree-Fock-Bogoliubov (left) and Interactive Boson Model (right) potential energy surface calculations for $^{180-198}$Pt from Ref. [6].
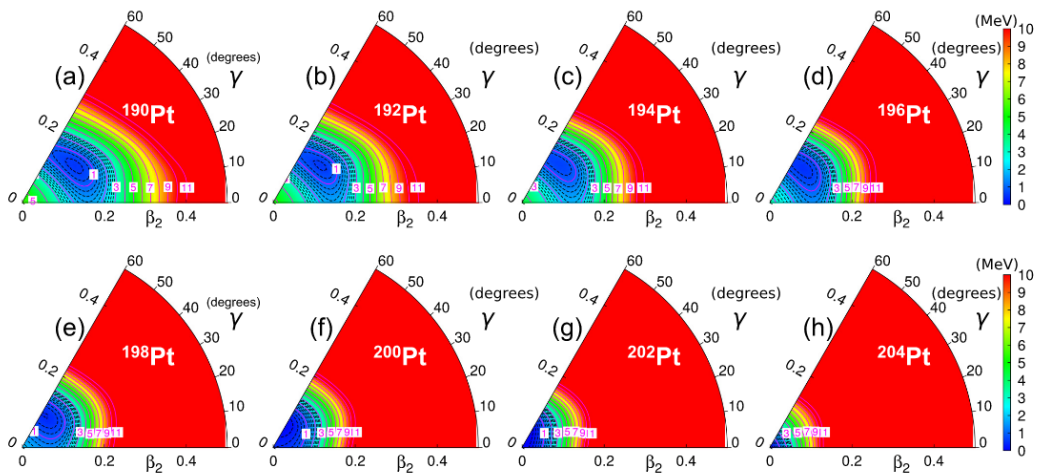
Figure 1.3: Hartree-Fock-Bogoliubov with the Gogny-D1S interaction potential energy surface calculation in the triaxial plane for $^{190-204}$Pt from Ref. [7].

1.2 Carbon isotopic chain: ^{14}C

The Z = 6 carbon isotopic chain has drawn immense interest over the last decade, which was originally due to the report of a "new state of nuclear matter" in ^{16}C with an almost spherical proton core decoupled from a deformed neutron distribution [21, 22, 23]. Further measurements at LBNL [24], MSU [25], Riken [26], and ANL [27] were unable to confirm this exotic behaviour, and placed ^{16}C within expected systematics of neighbouring nuclei instead. Parallel to the ^{16}C efforts, measurements in other neutron-rich carbon isotopes [26, 28, 29] provided an opportunity to systematically investigate the evolution of nuclear structure from stability to the drip line. These experimental results provide stringent constraints on theoretical models and address the role of the valence neutron-proton interaction to successfully describe excited-state properties.

The current knowledge of B(E2: $2_1^+ \rightarrow 0_1^+$) values for the even-even N $\geq$ 6 carbon isotopes from Ref. [30] are summarised in Fig. 1.4. The shell model calculations [30] (orange squares connected by a dashed line), follow the experimentally observed trend quite well for ^{16}C, ^{18}C, and ^{20}C. The similar and relatively low B(E2: $2_1^+ \rightarrow 0_1^+$) values for the first-excited states in ^{16}C and ^{18}C are explained by the dominant neutron excitations within the sd shell [24], while the observed increase in collectivity towards ^{20}C is due to an increase of the proton contribution to the wave function. This behaviour has been discussed in detail using a seniority scheme [31], where the addition of neutrons modifies the tensor force and reduces the proton $p_{3/2}-p_{1/2}$ spin orbit splitting. The seniority scheme from Ref. [31] is shown in Fig. 1.5. It is interesting to note that Ref. [31] suggests that neutrons do not contribute to the B(E2: $2_1^+ \rightarrow 0_1^+$) of ^{14}C, it is purely protons.

Despite the good agreement for neutron-rich carbon isotopes the calculations overestimate the B(E2: $2_1^+ \rightarrow 0_1^+$) values for both, ^{12}C and ^{14}C quite significantly. The increase in B(E2: $2_1^+ \rightarrow 0_1^+$) towards ^{12}C is due to an increase in proton contribution which dominates the 2_1^+ configuration. It should be noted that the similarity of experimental B(E2: $2_1^+ \rightarrow 0_1^+$) values for ^{14}C, ^{16}C, and ^{18}C, is unexpected given the large change in the 2_1^+ energies of these isotopes, shown in Fig. 1.6.

It is also interesting to mention that microscopic particle-vibration model calculations from Ref. [32] exhibit the same features and trends as the shell model results of Fig. 1.4. Results from no-core shell model calculations from Ref. [33] using NN as well as NN + NNN interactions, are shown in Fig. 1.7. In general, the results follow a similar trend as the more "traditional" models with the notable exception that the collectivity of ^{12}C is now correctly reproduced. This work also supports the picture of the 2_1^+ state in ^{16}C being primarily due to neutron excitation, while the 2_1^+ state in ^{14}C is dominated by proton ex-
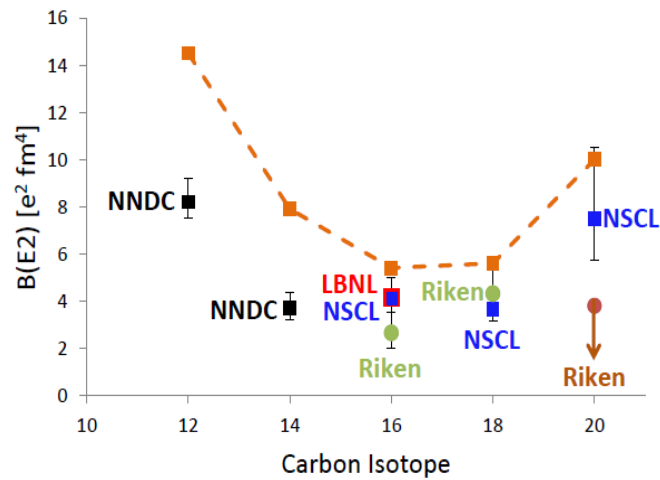
Figure 1.4: A summary of the current knowledge of B(E2: $2^+ \rightarrow 0_1^+$) values for the even-even N ≥ 6 carbon isotopes [30]. The black data points are values taken from the most recent evaluated nuclear data base [1], while other experimental data points are from recent measurements [24, 25, 26, 28, 29]. The orange dashed line connects data points from shell model calculations utilising isospin dependent effective charges [30].
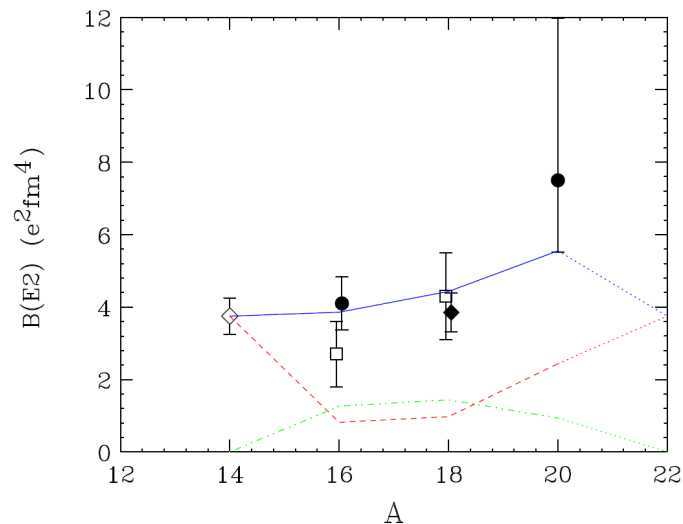
Figure 1.5: Phenomenological treatment from Ref. [31]. of the Z=6 isotope chain is shown as the blue line. The contributions from neutrons (green) and protons (red) are also indicated.
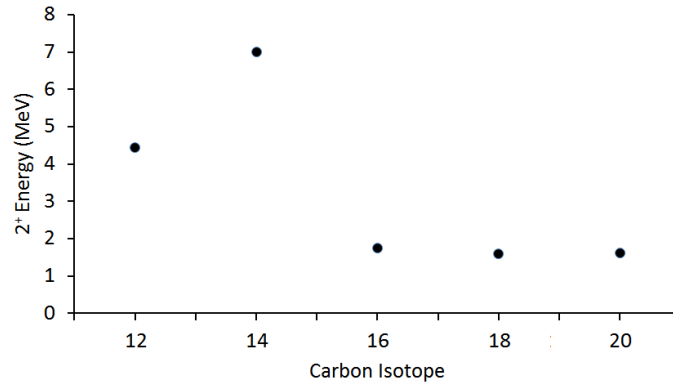
Figure 1.6: Excitation energies of the first-excited 2^+ states in neutron-rich, even-even carbon isotopes.
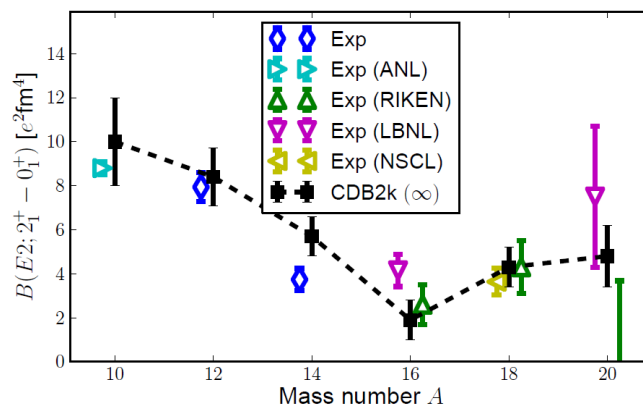
Figure 1.7: No-core shell model calculations (black data points connected by a dashed line) of even-even Carbon isotopes [33].

citation within the p-shell. However, despite the agreement between the experimental and theoretical B(E2: $2_1^+ \rightarrow 0_1^+$) value in ^{12}C, the no-core shell model still overestimates the observed ^{14}C value significantly which is a persistent feature of results from other models.

The E2 properties of nuclei can give powerful information on the collective shape parameters for quadrupole collective modes and this is discussed in Sec. 2.7. The continued overestimate of the B(E2: $2_1^+ \rightarrow 0_1^+$) value in ^{14}C raises important questions that need to be addressed to obtain a complete picture of the structural evolution from the line of stability to the drip line. Experimental constraints on theoretical models are of upmost importance to advance our understanding of nucleonic interactions. As such it is imperative that the disagreement in ^{14}C is carefully investigated to identify the underlying cause of the disagreement, be it experimental or theoretical in nature.

The ENSDF [1] accepted lifetime value for the ^{14}C first-excited 2_1^+ state at 7.012 MeV is 9.0(14) fs. This value is based entirely on one width measurement (50.7(71) meV) from
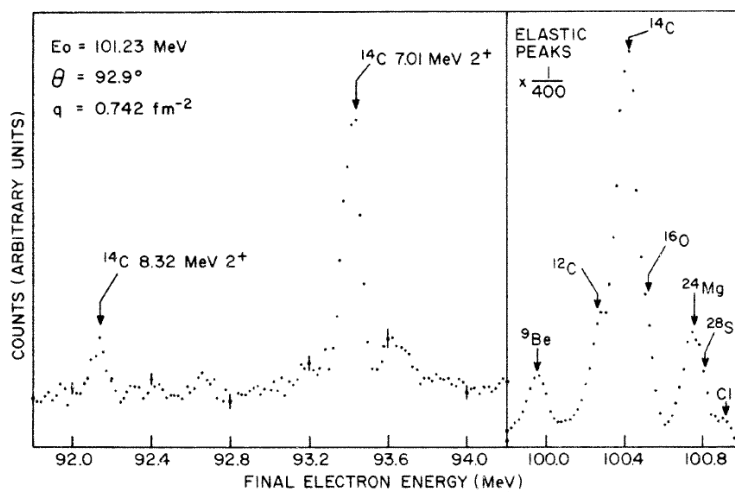
Figure 1.8: Momentum spectrum of electrons scattered off a ^{14}C target from which the lifetime of the 7.012 MeV first-excited 2^+ state was determined in Ref. [3].

an ^{14}C(e,e') experiment [3], shown in Fig. 1.8. These experimental results were unfortunately only published as a conference proceeding and remain the only measurement which provides information on the B(E2: $2_1^+ \rightarrow 0_1^+$) value in ^{14}C. A second measurement of this value is highly desirable as it will provide a critical piece for a better understanding of the structural evolution of the carbon isotopic chain.

Chapter 2

Theory

The Coulomb excitation method is used to obtain information on the collective behaviour of nuclei, probe the interaction between protons and neutrons, the emergence and vanishing of shell gaps and deformation of the nucleus. From this, conclusions can be drawn on the evolution of the structural mechanism and constraints for theoretical models. Refs. [34, 35] give an overview of the theory of Coulomb excitation and Ref. [20] provides an introduction to the GOSIA code used to analyse and simulate Coulomb excitation experiments. The fundamental information on nuclear models given in this chapter is summarised from Ref. [36]. This Chapter is a brief overview of the theoretical background of the Coulomb excitation technique that can be found in Refs. [34, 35].

2.1 Electromagnetic properties of the atomic nucleus

Many forces govern the shape, movement and structure of matter, such as gravity, Coulomb force and the nuclear force. Gravity is an attractive force that two objects experience just by having mass. The Coulomb force is a force that a charged object experiences due to another charge or electromagnetic field. The nuclear force (also known as the strong force or nucleon-nucleon interaction) is the attractive force between nucleons in a nucleus. Generally it becomes repulsive when nucleons are < 0.7 fm apart. At such short distances the nuclear force is stronger than the Coulomb force and can overcome the Coulomb repulsion between protons. The nuclear force is the "glue" that keeps nucleons together to form a nucleus and is responsible for the motion and distribution of nucleons in a nucleus.

The Coulomb force (electromagnetic interaction) is an effective tool to probe the distribution of the nucleons in the nucleus, because the electromagnetic interaction has a much smaller effect on the motion of nucleons compared to the nuclear force. For this work the focus is on the Coulomb force and measures are taken to ensure that the distance

10

between the interacting objects is larger than the range where effects from the nuclear interaction can be observed. The impact of the nuclear force on the excitation process can thus be ignored. The gravitational force between nucleons is negligible because the mass of the nucleons involved are very small and the gravitational force is small compared to the Coulomb force. The Coulomb potential between two nuclei is given by [37]:

$$V(r) = \frac{-Z_1 Z_2 e^2}{4\pi\epsilon_0 r}, \tag{2.1}$$

where the subscripts 1 and 2 refer to the different nuclei, $Z_{1,2}$ is the proton number, e is the electron charge, ϵ_0 is the vacuum permittivity and r is the distance between the nuclei. It is the Coulomb interaction between two nuclei, ^{14}C and ^{194}Pt, that is being investigated in this work through a beam of ^{14}C interacting on a ^{194}Pt target.

2.1.1 Shell model

The distribution and motion of nucleons in a nucleus can be described by the shell model which is a model that is considered to be very successful. Take the example of ^{194}Pt, it has 194 nucleons. Each nucleon is in a potential field that is influenced by every other nucleon in the nucleus (due to the nuclear and Coulomb forces).

In a nucleus a proton (neutron) with spin $-1/2$ will form a pair with another spin $1/2$ proton (neutron). In the ground state of an even-even nucleus all the protons (neutrons) will pair up and the pairs fill up different energy levels. Different levels can have different number of pairs, for example the lowest level, $s_{1/2}$ can have only 1 pair while the next higher level, $p_{3/2}$ can have 2 pairs (a quartet). A simple shell-model scheme is shown on the left-side of Fig. 2.1. For odd-even or odd-odd nuclei in the ground state the highest occupied level will contain the non-paired nucleons. If a nucleon obtains enough energy a nucleon-pair may be broken and a nucleon can move to a higher energy level. If there is an empty level below the nucleon it may de-excite and drop down to a lower level.

Each nucleon also has $\pm\frac{1}{2}$ spin. There is an interaction between the nucleon's spin and its orbit inside the nuclear potential. This spin-orbit interaction cause the levels to split as shown on the right side of Fig. 2.1. Including the spin-orbit interaction means the total angular momentum is composed of the orbital angular momentum λ and the spin S: $j = |\lambda \pm S|$. For example a level with $\lambda = 1$ can now be $j = 1/2$ or $j = 3/2$. This "splitting" of the levels cause shell gaps to appear after 2, 8, 20, 28 etc. nucleons are added. Nuclei with filled shells are more stable because more energy is required to move a nucleon across one of these shell gaps. These magic numbers hold for nuclei at or near the line of stability.
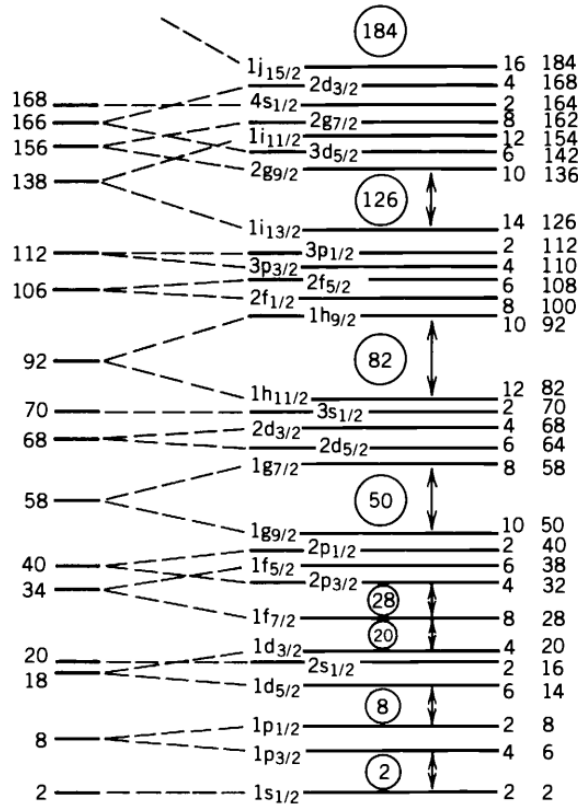
Figure 2.1: The energy levels calculated with the Wood-Saxon potential with and without spin-orbit interactions [37].

2.1.2 Transition probability

Each level, I is quantised and every nucleus has different quantised levels. When a nucleus makes a transition from an energy state E_i to E_f a γ-ray with an energy $E_\gamma = E_i - E_f$ is observed. The energy of a state will have some uncertainty:

$$\Gamma = \sqrt{<E^2> - <E>^2}. \tag{2.2}$$

This uncertainty is called the width Γ of the state. The time a nucleus remains in an excited state before making a transition is called the lifetime τ. The lifetime of a state is related to the width through the uncertainty principle (with $\Delta t = \tau$) by: $\tau = \hbar/\Gamma$. The transition probability W is then inversely related to the mean lifetime [37]:

$$W \propto \frac{1}{\tau}. \tag{2.3}$$

W can be calculated from the nuclear wave function ψ by using Fermi's Golden rule [37, 38]:

$$W = \frac{2\pi}{\hbar} | <\psi_f|\hat{H}|\psi_i> |^2 \rho(E_f), \tag{2.4}$$

where $\rho(E_f)$ is the density of the final states and $|\langle \psi_f | \hat{H} | \psi_i \rangle|$ is the transition matrix element. Transitions can be either electric (E) or magnetic (M) depending on the relative parity, π of the initial and final levels. If there is a difference in parity then the emitted radiation must have odd parity. If there is no difference in parity then the emitted radiation must have even parity. Electric transitions have $\pi = (-1)^\lambda$ and magnetic transitions have $\pi = (-1)^{\lambda-1}$ where λ is the orbital angular momentum of the γ-ray.

A γ-ray must carry at least one unit of angular momentum which leads to the angular momentum selection rule: $|I_i - I_f| \le \lambda \le I_i + I_f$. Only a transition where the angular momentum rule is obeyed can take place. In general, the angular momentum and parity selection rules are given by [37]:

- $|I_i - I_f| \le \lambda \le I_i + I_f$

- $\Delta\pi =$ no, then $\lambda =$ even is electric and $\lambda =$ odd is magnetic

- $\Delta\pi =$ yes, then $\lambda =$ odd is electric and $\lambda =$ even is magnetic

Using these selection rules, transitions can be identified by either Eλ or Mλ. The transition probability expanded for each multipole is known as Weisskopf estimates and is given by [37]:

$$W(E\lambda) = \frac{8\pi(\lambda+1)}{[\lambda(\lambda+1)!!]^2} \frac{e^2}{4\pi\epsilon_0 \hbar c} \left(\frac{E}{\hbar c}\right)^{2\lambda+1} \left(\frac{3}{\lambda+3}\right)^2 cR^{2\lambda}, \quad (2.5)$$

$$W(M\lambda) = \frac{8\pi(\lambda+1)}{[\lambda(\lambda+1)!!]^2} \left(\mu_p \frac{1}{\lambda+1}\right)^2 \left(\frac{\hbar}{m_p c}\right)^2 \frac{e^2}{4\pi\epsilon_0 \hbar c} \left(\frac{E}{\hbar c}\right)^{2\lambda+1} \left(\frac{3}{\lambda+2}\right)^2 cR^{2\lambda-2}, \quad (2.6)$$

where $R = R_0 A^{1/3}$, A is the atomic mass, $R_0 = 1.15 fm$, m_p is the mass of a proton, e is an electron charge, μ_p is a proton magneton and ϵ_0 is the vacuum permittivity. The Weisskopf estimates give an indication of the number of nucleons involved in a transition. The reduced transition probability is given by [37]:

$$B(E\lambda) = \frac{(1.2)^{2\lambda}}{4\pi} \left(\frac{3}{\lambda+3}\right)^2 A^{\lambda 2/3} e^2 b^{2\lambda}, \quad (2.7)$$

$$B(M\lambda) = \frac{10}{\pi} (1.2)^{2\lambda-2} \left(\frac{3}{\lambda+3}\right)^2 A^{(2\lambda-2)/3} \mu_N^2 b^{2(\lambda-1)}, \quad (2.8)$$

where A is the atomic mass, μ_N is the nuclear magneton and b is the unit barn.

2.1.3 Collective motion

Nuclei with an even or odd number of nucleons or a combination thereof have different nuclear properties. Even-even nuclei have a ground state of 0^+ because all the protons

and neutrons pair to give a net spin of 0. Odd-even nuclei have one unpaired nucleon and the orbit it occupies generally determines the spin and parity properties of the ground state. With some oversimplification the nuclear properties for an odd-even nucleus arises from the motion of unpaired nucleons. Similar to odd-even nuclei, odd-odd nuclei have two unpaired nucleons which determine the nuclear structure properties.

The shell model is a powerful model. It can be used to calculate spin-parity assignments, energy levels, electric and magnetic moments and the probability of a transition between two states. The shell model is also successful in describing level structure. The shell model begins to fail when collective motion is considered. Collective motion occurs when all the nucleons determine the structure of the nucleus. Some collective properties such as the energy for the 2_1^+ state for even-even nuclei are shown in Fig. 2.2(a). Panel (b) compares the energy for the 2_1^+ states with a recent model [39]. It should be noted that various models are used to study the collective properties, such as a Shell model calculations from Refs. [40, 41] and BMF calculations from Ref. [42]. The energy of the first 2^+ state is a general property of even-even nuclei and does not depend on the excitation of a single nucleon.

These collective properties are a product of the motion of the entire nucleus; of all the nucleons. Some other collective properties are [37, 36]:

- The ratio $E(4^+)/E(2^+)$, which is ~ 2 for $A < 150$ and 3.3 for $150 < A < 190$

- The magnetic moments of 2^+ states are 0.7-1.0 μ_N

- Electric quadrupole moments are generally small for $A < 150$ and much larger for $A > 150$

Mass $A < 150$ and mass $150 < A < 190$ nuclei have different types of collective structures. Mass $A < 150$ nuclei are best described by vibrations around a spherical core and mass $150 < A < 190$ nuclei are best described by rotations of a non-spherical system.

The B(E2) values for various transition of ^{194}Pt and ^{14}C will be determined through this work. A large B(E2) value indicates that it is a collective excitation while a small B(E2) value will indicate a single particle excitation. By using the B(E2) values for various transitions the deformation of states can also be determined. This will be discussed in more detail in Sec. 2.7
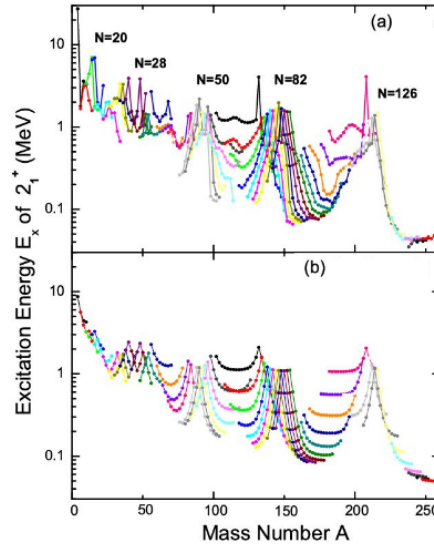
Figure 2.2: The energies of the lowest 2^+ states for even-even nuclei from data (a) [11] compared to an empirical formula (b) discussed in Ref. [39].

2.1.3.1 Vibrations

It may happen that the average shape of a nucleus is spherical, but the instantaneous shape is not. This is known as nuclear vibration. The instantaneous shape is given by [37]:

$$R(t) = R_{av} + \sum_{\lambda \geq 1} \sum_{\mu=-\lambda}^{+\lambda} \alpha_{\lambda\mu}(t) Y_{\lambda\mu}(\theta, \phi), \qquad (2.9)$$

where $Y_{\lambda\mu}(\theta, \phi)$ are the spherical harmonics, $R(t)$ is a point on the nuclear surface at angles (θ, ϕ) and $\alpha_{\lambda\mu}$ is the amplitude. μ is the magnetic quantum number and λ is the different mode of vibration, $\lambda = 1$ is for dipole vibrations $\lambda = 2$ is for quadrupole vibrations etc. The different vibrational modes for a nucleus is shown in Fig. 2.3. Vibrational energy can be quantised with phonons. The quadrupole phonon carries 2 units of angular momentum (λ) with even parity given by $(-1)^\lambda$. By adding a quadrupole phonon to the 0^+ ground state for an even-even nucleus can only give a 2^+ state. By adding two quadrupole phonons to the ground state, simplifying with symmetric combinations, the following combinations can be obtained:

$$\lambda = 4 \quad \mu = +4, +3, +2, +1, 0, -1, -2, -3, -4 \qquad (2.10)$$

$$\lambda = 2 \quad \mu = +2, +1, 0, -1, -2 \qquad (2.11)$$

$$\lambda = 0 \quad \mu = 0 \qquad (2.12)$$

This gives a triplet of states. A simplistic illustration of the vibrational band for 1, 2 and 3 quadruple phonons added to the 0^+ of an even-even nucleus is shown in Fig. 2.4.
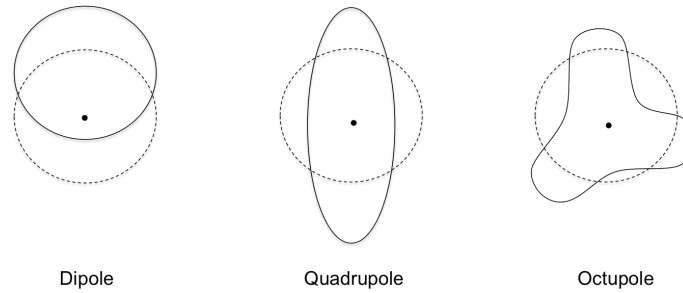
Figure 2.3: The dashed line is the equilibrium shape and the solid line is the instantaneous vibrating nuclear shapes for different modes of vibration.
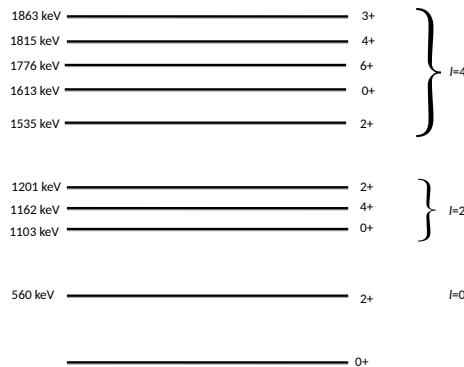
Figure 2.4: A simplistic illustration of the low-lying levels in the even-even 120Te nucleus due to the vibration phonons [43]. Here l denotes angular momentum. The one quadrupole phonon 2^+ state, the two quadrupole phonon 0^+, 2^+, 4^+ and the three quadrupole phonon states 0^+, 2^+, 3^+, 4^+, 6^+ can be clearly identified.

2.1.3.2 Rotation

A rotating spherical nucleus cannot be observed because it is symmetric along all axes. Deformed nuclei with an ellipsoid shape can rotate since they can have two or more different axes. An explicit form of Eq. 2.9 gives the shape of a rotating nucleus [37]:

$$R(\theta, \phi) = R_{av}\left[1 + \beta Y_{20}(\theta, \phi)\right], \tag{2.13}$$

where Y_{20} is the spherical harmonics factor $\frac{1}{4}\sqrt{\frac{5}{\pi}}(3\cos^2\theta - 1)$ and β is the α_{20} parameter, or as it is more commonly referred to, the deformation parameter related to the eccentricity of the ellipse by:

$$\beta = \frac{4\Delta R}{3R_{av}}\sqrt{\frac{\pi}{5}}. \tag{2.14}$$

ΔR is the difference between the semimajor and semiminor axes. Nuclei with $\beta > 0$ are prolate and $\beta < 0$ are oblate. It should also be noted that when all three of the axes are different a nucleus is called triaxial. The triaxiality parameter will be briefly described

1518 keV ——————————— 10+

1025 keV ——————————— 8+

614 keV ——————————— 6+

300 keV ——————————— 4+

91 keV ——————————— 2+

——————————— 0+
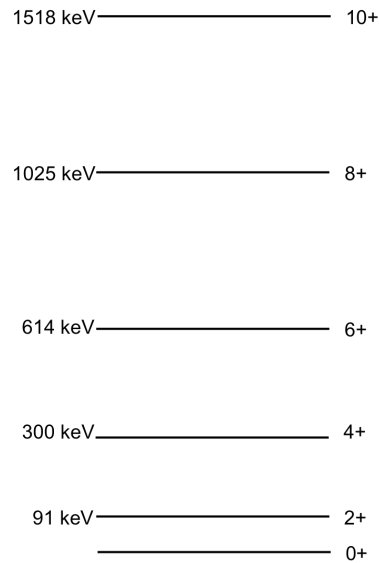
Figure 2.5: A simplistic illustration of the low-lying levels due to the rotation of the ground state band in ^{164}Er [44].

in Sec 2.7. A trademark of deformation is the electric quadruple moment. The electric quadrupole moment can be given in term of deformation by [37]:

$$Q_0 = \frac{3}{\sqrt{5\pi}} R_{av}^2 Z \beta (1 + 0.16\beta), \qquad (2.15)$$

where Q_0 is the intrinsic quadrupole moment and Z is the charge number. The energy of a rotating object is given by:

$$E = \frac{\hbar^2}{2\mathcal{J}} I(I+1), \qquad (2.16)$$

where $\mathcal{J}$ is the moment of inertia and I is the angular momentum quantum number. By adding rotational energy to the nucleus a rotational band will form. The states forming due to rotation of the ground state band in ^{164}Er are shown in Fig. 2.5.

Vibrations behave differently in deformed nuclei, there are two types: β- and γ-vibrations. The γ parameter refers to α_{22} in Eq. 2.9. Using the rugby ball analogy, β-vibrations are pulling and pushing on the ends of the ball and γ-vibrations are pushing and pulling at the sides.

2.2   Theory of nuclear reactions

When a nucleus is impinged on another nucleus many different reaction mechanisms can take place. In general, the type of reactions can be split into two groups: direct reactions and compound reactions. During direct reactions the projectile and target will make

contact and separate almost immediately. During contact some energy or particles can be exchanged. During compound reactions the nuclei will coalesce and form a compound nucleus long enough to share energy between all the nucleons. Some direct interactions are:

- Elastic scattering: The projectile and target will stay in their ground states during the collision, because no energy is exchanged. Elastic scattering is also known as Rutherford scattering.

- Inelastic scattering: The projectile and target exchange energy and they are excited. Coulomb excitation is a form of inelastic scattering.

- Transfer reaction: Particles are exchanged during the collision, for example during the reaction ^{13}C(d,p)^{14}C the deuteron will give a neutron to the ^{13}C producing ^{14}C. During transfer reactions a nucleus can lose nucleons (also known as stripping reactions) or it can gain some (also known as pickup reactions).

- Charge exchange: The projectile and target exchange charge, for example during the ^{13}C(p,n)^{12}N reaction a proton is exchanged for a neutron. The mass number remains the same, however Z changes.

- Fragmentation: One projectile might break or knock out part of the target causing multiple outgoing particles.

- Multistep process: This is when two or more of the above mentioned reaction mechanisms happen.

Compound reaction mechanisms are:

- Fusion: When two particles collide and form a new particle. The resultant particle can then undergo fission or emit γ-rays or particles.

- Fission: When a heavy nucleus breaks up into smaller pieces. This can happen spontaneously or be induced by adding nucleons until the nucleus undergoes fission.

A typical nucleon orbits within the nucleus in $\sim 10^{-22}$ seconds. If the reaction is completed within this time then there is not enough time for the nucleus to dissipate the energy between all the nucleons. A compound nucleus process requires $\sim 10^{-16}$ to 10^{-18} seconds to take place. Direct reactions happen at the surface of the nuclei, however compound reactions involve the whole nucleus.

The focus of this work is the Coulomb excitation (a form of inelastic scattering) of ^{14}C and ^{194}Pt. For this work ^{14}C is utilised for the beam and ^{194}Pt is the target. The Coulomb

excitation process can be divided into single-step excitation where only a single state is excited and a multi-step excitation where many states are populated via excitation of intermediate states.

The single-step Coulomb excitation of the 2_1^+ state in ^{14}C is favoured due to the high energy of the 2_1^+ state at 7012 keV. With the E_{Beam}= 45 MeV used for the Coulomb excitation neither the 2_2^+ state nor the 4_1^+ state will be observed because they are above the neutron separation (S_n) energy of 8176 keV. Above S_n primarily neutrons are emitted making it very difficult to observe these states.

The multistep Coulomb excitation process is favoured for the states of ^{194}Pt. The states are relatively close in energy with the 2_1^+ state at a low energy of 328 keV. The $2_2^+, 4_1^+...$ states are also easier to excite due to relatively large B(E2: $2_1^+ \rightarrow 0_1^+$) values. The particle detector was placed at backward angles, collisions where the particle scatters backwards have more time for the electric fields to interact. This makes multistep Coulomb excitation favourable.

2.2.1   Coulomb excitation

Coulomb excitation is based on an assumption of a purely electromagnetic interaction between collision partners and care must be taken that nuclei do not come close enough to experience the influence of the nuclear force. In Fig. 2.6 a charged particle moves towards a stationary target with velocity v. The particle will reach a minimum distance r_{min} (where $b \neq 0$) before the Coulomb force pushes it away due to the Z of the target and projectile, this distance depends on the impact parameter b. The distance of closest approach d (obtained when $b = 0$) is given by [20]:

$$d = 1.25 \cdot (A_p^{1/3} + A_t^{1/3}) + 5[fm], \tag{2.17}$$

where A_p is the mass number of the projectile and A_t is the mass number of the target. In the experiment relevant to this work of bombarding ^{14}C on a ^{194}Pt target, $d = 15.25$ fm. To ensure that the nuclei never get closer than d, a limit is set on the bombarding energy i.e. the kinetic energy of the projectile must be below the Coulomb barrier. This ensures that any contributions from the nuclear force is negligible. A formula for safe bombarding energy in a head-on collision, called Cline's safe energy criteria, is used to ensure that surfaces of the nuclei are separated by at least 5 fm. This ensures that the influence of the nuclear force on the total reaction cross section is $< 0.1\%$. The safe bombarding energy is given by [20]:
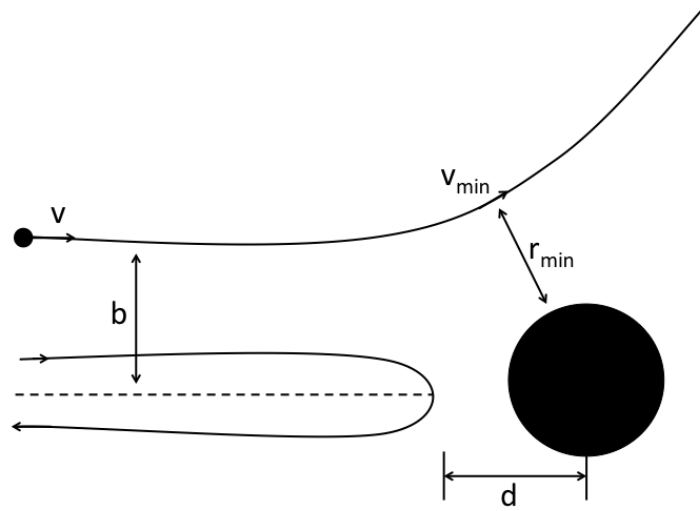
Figure 2.6: Kinematics of Coulomb scattering.

$$E_B(\theta_{CM}) = 0.72 \cdot \left(\frac{Z_p Z_t}{d}\right) \cdot \left(\frac{A_p + A_t}{A_t}\right) \cdot \left(1 + \frac{1}{sin(\theta_{CM}/2)}\right) [MeV]. \tag{2.18}$$

For particles scattering backwards, Cline's criteria becomes:

$$E_B(\theta_{CM} = \theta_{LAB} = 180°) = 1.44 \cdot \left(\frac{Z_p Z_t}{d}\right) \cdot \left(\frac{A_p + A_t}{A_t}\right) [MeV]. \tag{2.19}$$

The maximum safe bombarding energy in this experiment is $E_{Beam} = 47.4$ MeV for particles scattering backwards, hence $E_{Beam} = 45$ MeV is used during the Coulomb excitation experiment. This safe bombarding energy is only applicable when the semi-classical approximation is valid.

2.3 Semiclassical approach

The semiclassical approach can be used when: the incoming particle wavelength is small compared to the classic hyperbolic trajectory, the energy loss between the collision partners is small compared to the bombarding energy and when the interaction is purely electromagnetic. The interaction is purely electromagnetic by ensuring that the bombarding energy is below the safe-energy as discussed in Sec. 2.2.1. The Sommerfeld parameter expresses the ratio of the incoming wavelength to the classical hyperbolic trajectory as [20]:

$$\eta = \frac{2\pi d_{min}}{2\lambda} = \frac{Z_1 Z_2 e^2}{\hbar v_I} >> 1. \tag{2.20}$$

Here v_I is the initial velocity of the incoming projectile with a reduced wavelength λ, subscripts 1 indicates the projectile and 2 indicates the target and $Z_1 e$ and $Z_2 e$ are the

charges of the nuclei. For this experiment of bombarding ^{14}C on ^{194}Pt with the maximum safe-energy of 47.4 MeV gives $\eta = 40$. The final requirement that the energy loss due to atomic and nuclear interaction in the target must be small compared to the bombarding energy can be expressed by:

$$\frac{\Delta E}{E_B} << 1, \tag{2.21}$$

where ΔE is the energy loss in the target. The states of interest are the 2_1^+ of ^{14}C which is at 7.01 MeV and the 2_1^+ and 4_1^+ states of ^{194}Pt which are all below 1 MeV. This makes the energy loss ratio 0.15 for ^{14}C and 0.02 for ^{194}Pt with $E_{Beam} = 47.4$ MeV.

The collision time is of the order $\approx 10^{-21}$s [45]; orders of magnitude shorter than the lifetime of nuclear states normally studied. In this case the lifetime of the ^{14}C 2_1^+ state is 9×10^{-15}s according to the width measurement discussing in Ch. 1. For ^{194}Pt the lifetimes are of the order $\sim$ ps. This enables the separate and sequential treatment of the γ decay and nuclear excitation.

2.4 Coulomb excitation formalism

The electromagnetic interaction potential can be expanded in a multipole series as done in Ref. [46]. The potential is effectively divided into 3 parts: a monopole-monopole interaction part that defines the kinematics, a monopole-multipole interaction part and the multipole-multipole interaction part. The multipole-multipole term is very small compared to the monopole-multipole term and can be neglected. Using this multipole expansion the Schrödinger equation can be expressed as:

$$i\hbar \frac{\partial}{\partial t}|\psi(\mathbf{r}, t) >= (H_{1,2}^0 + V_{1,2}(\mathbf{r}(t)))|\psi(\mathbf{r}, t) >, \tag{2.22}$$

where $V_{1,2}(\mathbf{r}(t))$ is the monopole-multipole interaction between projectile and target and $H_{1,2}^0$ is the free particle hamiltonian. $\mathbf{r}(t)$ is the classical trajectory, determined by the monopole-monopole term, and t is time. The target and projectile can be interchanged so the indexes 1 and 2 will not be shown unless necessary. Let $|\psi(\mathbf{r}, t) >$ be described by:

$$|\psi(\mathbf{r}, t) >= \sum_n a_n(t)|\phi_n(\mathbf{r}) > exp(-iE_n t/\hbar), \tag{2.23}$$

where $|\phi_n(\mathbf{r}) >$ is the free-nucleus wave function and $H^0|\phi_n >= E_n|\phi_n >$. Substituting 2.22 into 2.23 and using orthonormality of the wave functions for the free nucleus $< \phi_k|\phi_n >= \delta_{kn}$ gives a set of differential equations for the excitation amplitude:

$$\frac{da_k(t)}{dt} = \frac{-i}{h} \sum_n a_n(t) < \phi_k|V_{1,2}(t)|\phi_n > exp\frac{it}{\hbar}(E_k - E_n). \tag{2.24}$$

Here, $a_k(t)$ are the complex expansion coefficients. Before the collision it is assumed that the nucleus is in the ground state so $a_k(t \to -\infty) = \delta_{k,0}$. After the collision, the nucleus is described by $a_k(t)$. Expanding the interaction potential $V(t)$ into a multipole series gives [46]:

$$V_{1,2}(t) = \sum_{i=1}^{\infty} \sum_{\mu=-\lambda}^{\lambda} \frac{4\pi Z_{2,1}e}{2\lambda+1}(-1)^{\mu}S_{\lambda\mu}(t)M_{1,2}(\lambda,-\mu), \tag{2.25}$$

where, for electric transitions:

$$S_{\lambda\mu}(t) = \frac{Y_{\lambda\mu}(\theta(t),\phi(t))}{[r(t)]^{\lambda+1}}; \tag{2.26}$$

and for magnetic transitions:

$$S_{\lambda\mu}(t) = \frac{1}{c\lambda}\frac{\frac{d\mathbf{r}}{dt}\cdot(\mathbf{r}\times\Delta)}{[r(t)]^{\lambda+1}}Y_{\lambda\mu}(\theta(t),\phi(t)). \tag{2.27}$$

$Y_{\lambda\mu}$ are spherical harmonics, Δ is the gradient operator, e is the charge of an electron, Z is the charge number, λ is the multipolarity and μ is the momentum projection on the symmetry axis. The matrix elements of the electromagnetic transfer operator $M(\lambda,\mu)$ is for electric and magnetic multipole moments [46]:

$$M(E\lambda,\mu) = \int \rho(\mathbf{r})r^{\lambda}Y_{\lambda\mu}(\theta,\phi)d^3\mathbf{r}$$
$$M(M\lambda,\mu) = \frac{1}{c(\lambda+1)}\int r^{\lambda}\mathbf{j}(\mathbf{r})(\mathbf{r}\times\Delta)Y_{\lambda\mu}(\theta(t),\phi(t))d^3\mathbf{r}. \tag{2.28}$$

$\rho(\mathbf{r})$ is the spatial charge and $\mathbf{j}(\mathbf{r})$ is the current distributions of the free nucleus. By using the Wigner-Eckart theorem the excitation amplitude can be given by inserting Eqs. 2.23 - 2.28 into 2.22 [20]:

$$\frac{da_k(t)}{dt} = -i\frac{4\pi Z_{1,2}e}{h}\sum_{n}a_n(t)exp\frac{it}{h}(E_k-E_n)\sum_{\lambda\mu}(-1)^{\mu}$$
$$\cdot S_{\lambda\mu}(t) < \phi_k|M(\lambda,-\mu)|\phi_n > . \tag{2.29}$$

The reduced matrix elements $(< \phi_k|M(\lambda,-\mu)|\phi_n >)$ contain the information on the nuclear wave functions. The matrix element of an operator $M(\lambda,\mu)$ can be factorised using the Wigner-Eckart theorem [47]:

$$< I_im_i|M(_M^E\lambda,\mu)|I_fm_f >= (I_f\lambda m_f\mu|I_im_i) < I_f||M(_M^E\lambda)||I_i >, \tag{2.30}$$

where $(I_f\lambda m_f\mu|I_im_i)$ are Clebsch-Gordan coefficients and $m_{i,f}$ is the spin projection. Taking into account the orthonormality of Clebsch-Gordan coefficients, the reduced transition probability $B(_M^E\lambda)$ can be given by [20]:

$$B(^E_M\lambda, I_i \rightarrow I_f) = \frac{1}{2I_i+1}|<I_i||M(^E_M\lambda)||I_f>|^2. \tag{2.31}$$

The spectroscopic quadrupole moment, Q_{sp} is related to the matrix element by:

$$eQ_{sp} = \sqrt{\frac{16\pi}{5}}\frac{1}{\sqrt{2I_i+1}}(I_f\lambda m_f\mu|I_im_i)<I_i||M(^E_M\lambda)||I_f> \tag{2.32}$$

The spectroscopic moment Q_{sp} is related to the intrinsic moment Q_0 described in Eq. 2.15 for transitions where $I_i = I_f$ and axial symmetry is assumed by:

$$Q_{sp} = \frac{3K^2 - I(I+1)}{(I+1)(2I+3)}Q_0, \tag{2.33}$$

where K is the projection of the total angular momentum on the symmetry axis. The GOSIA code is one of the tools that can be used to analyse Coulomb excitation experiments. From the analysis, which will be explained in chapter 7, the matrix elements are extracted, from which the spectroscopic quadrupole moment and reduced transition probabilities can be determined.

2.5 De-excitation of states

In a typical Coulomb excitation experiment information from either or both particles and γ-ray decay are required. In the present work both particles and γ-rays are detected. The information obtained are then utilized to determine the Coulomb excitation cross sections and other spectroscopic properties.

Many experiment related effects can influence the γ-decay, namely: deorientation effects, relativistic corrections due to in-flight decay and internal conversion. For thin targets and heavy-ion beams these effects can have a significant impact. These effects will be discussed and then the γ-ray decay will be formulated. The computer science aspect of the GOSIA code will not be discussed.

2.5.1 Deorientation effect

When the projectile and target interact they are ionised. The interaction between the stripped electron shells and the atom causes fluctuating hyperfine fields. These fluctuating hyperfine fields of the de-exciting atom depolarise the nuclear state alignment and attenuates the angular distribution of the de-excitation γ-rays. This effect is known as nuclear deorientation [48, 37]. To account for this a spin and lifetime dependent attenuation coefficient G_k is introduced. With the inclusion of the hyperfine interactions, the basic angular correlations can be expressed in terms of the angular distribution tensor, $R_{k\chi}$ as [20]:

$$\frac{d^2\sigma}{d\Omega_p d\Omega_\gamma} = \sigma_R(\theta_p) \sum_{k\chi} R_{k\chi}(I, I_f) Y_{k\chi}(\theta_\gamma, \phi_\gamma). \qquad (2.34)$$

The angular distribution tensor is defined as:

$$R_{k\chi}(I, I_f) \equiv \frac{1}{2\gamma(I)\sqrt{\pi}} G_k \rho_{k\chi} \sum_{\lambda\lambda'} \delta_\lambda \delta_{\lambda'}^* F_k(\lambda\lambda', I_f I), \qquad (2.35)$$

where $Y_{k\chi}(\theta_\gamma, \phi_\gamma)$ are normalised spherical harmonics, $F_k(\lambda\lambda' I_2 I_1)$ are the γ-γ correlation coefficients, δ_λ is the $I_1 \to I_2$ transition amplitude for a given multipolarity, $\rho_{k\chi}(I)$ describes the initial condition of the nucleus and $\sigma_R(\theta_p)$ is the scattering angle dependent Rutherford cross-section.

2.5.2 Internal conversion

Up to this point it was assumed that an excited nucleus decays by emitting a γ-ray. In reality an excited nucleus can decay by emitting a γ-ray or an electron through internal conversion. During internal conversion the electromagnetic fields interact with an atomic electron causing it to be emitted. Following this process there is a vacancy in the atomic electron shell which is quickly filled by an electron from a higher shell. When an electron transitions from a higher to a lower shell a X-ray is emitted. Internal conversion can compete with γ-ray emission in some cases and it is necessary to correct for that. The probability of internal conversion increases with decreasing transition energy. The total internal conversion coefficient is defined as [37]:

$$c(\lambda) = \frac{\Gamma_{ic}}{\Gamma_\gamma}. \qquad (2.36)$$

This is the ratio of the internal conversion Γ_{ic} to γ-ray decay Γ_γ probabilities. States can be populated by unobserved cascade feeding from above due to internal conversion. To account for this the decay width is increased by $c(\lambda)$ [20]:

$$\Gamma(I, I_f)_{total} = \Gamma(I, I_f)_\gamma (1 + c(\lambda)). \qquad (2.37)$$

2.5.3 Corrections due to in-flight decay

When a nucleus emits a γ-ray while in-flight its wavelength will change. If the γ-ray is emitted while the particle is moving towards the observation point, the γ-ray's wavelength will become smaller (the energy increases). If the γ-ray is emitted while the particle is moving away from the observation point, the wavelength of the γ-ray will become longer (energy becomes smaller). This is known as Doppler shift and it can be described by [20, 49]:

$$E_{ds} = \frac{E_{initial}\sqrt{1 \pm \beta^2}}{1 \pm \beta \cos(\alpha)}, \tag{2.38}$$

where α is the angle between the γ-ray and particle, $E_{initial}$ is the γ-ray energy when the nucleus is stationary, E_{ds} is the energy of the Doppler shifted (and observed) γ-ray and $\beta = v/c$. When the particle is moving towards the observation point then a + sign is used, while a − sign is used when the particle is moving away from the observation point. In the present work the highest observed $\beta \approx 7\%$ therefore non-relativistic corrections are appropriate and were used. With the moving particle and γ-ray velocity and position information the shifted γ-ray can be Doppler corrected during offline analysis.

2.5.4 The experimental geometry

In a typical Coulomb excitation experiment the γ-rays emitted from the nucleus of interest are measured in coincidence with scattered projectile-like or recoil particles. The information on the geometry of the particle and γ-ray detection arrays must be therefore included in the data analysis process. The GOSIA code accounts for such geometrical effects as well as for the physical dimensions of the detectors.

In order to correct for the physical shape of the detectors and the energy loss in the target a special factor is introduced for the γ-ray intensity. This first part of the special factor is the intensity obtained by integrating over the relevant scattering angles θ and energy ranges covered by the particle detectors. This is multiplied by the γ-ray intensity obtained by solving the excitation equation for a point-like nucleus (for the mean θ and energy values).

The observed γ-ray intensities are then corrected for the angular range and the energy loss in the target. The corrected yields are used in the minimisation procedure and compared to the calculated ones.

2.6 Properties of excited states

From the Coulomb excitation experiment the transition strengths are determined. Other properties such as lifetimes, branching ratios, electromagnetic moments and mixing ratios can also be included in the matrix element calculation. These properties are given as starting values for the GOSIA code, discussed in chapter 7.

2.6.1 Electromagnetic moments

A distribution of electric charge and current produces electric and magnetic fields that vary characteristically with distance. The distribution of charge and current gets an electromagnetic multipole moment associated with each characteristic spatial dependence. The electric field originating from the net charge with a spatial dependence of $1/r^2$ is assigned the monopole moment (this is essentially the Coulomb field). The electric field with a spatial dependence $1/r^3$ comes from the dipole moment, similarly the electric field with spatial dependence $1/r^4$ comes from the quadruple moment and so forth. The magnetic moment arises from the current distribution. It is treated similarly to the electric moment, except it does not have a monopole moment. If the distribution is a perfect sphere only the monopole electric field will play a role. A deformed distribution (for example a rugby ball shape) will have multipole moments.

2.6.1.1 Magnetic moments

The magnetic moment μ originates with the motion of charged particles. μ describes the effect of the distribution of current on other moving charges that is classified as "magnetic". The vector potential at a point $\mathbf{r}$ is calculated using [37]:

$$\mathbf{A}(\mathbf{r}) = \frac{\mu_0}{4\pi} \int \frac{\mathbf{j}(\mathbf{r}')dv'}{|\mathbf{r} - \mathbf{r}'|}, \tag{2.39}$$

where $\mathbf{j}(\mathbf{r}')$ is the current density, $\mathbf{r}$ is the distance from the origin to the observation point and $\mathbf{r}'$ is the distance from the origin to the current distribution. After a multipole expansion the vector potential becomes:

$$\mathbf{A}(\mathbf{r}) = \frac{\mu_0}{4\pi} \frac{\boldsymbol{\mu} \times \mathbf{r}}{r^3} + \dots, \tag{2.40}$$

where μ is given by:

$$\mu = \frac{1}{2} \int \mathbf{r}' \times \mathbf{j}(\mathbf{r}')dv'. \tag{2.41}$$

2.6.1.2 Electric moments

The electric moment originates from the distributions of charges. The electric potential $V(\mathbf{r})$ is given by [37]:

$$V(\mathbf{r}) = \frac{1}{4\pi\epsilon_0} \int \frac{\rho(\mathbf{r}')dv'}{|\mathbf{r} - \mathbf{r}'|}. \tag{2.42}$$
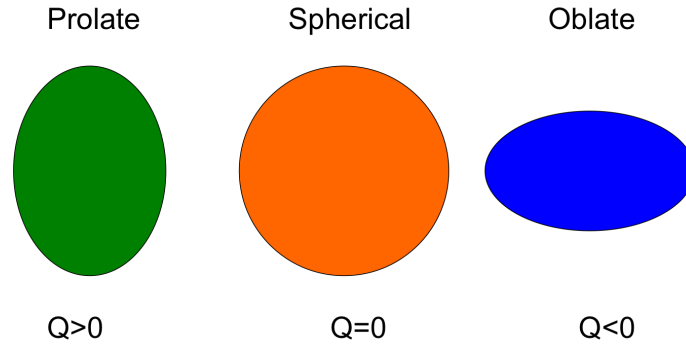
Figure 2.7: The different shapes of a nucleus and their dependence on their spectroscopic quadrupole moment Q_{sp}.

The electric potential can be expanded assuming that the observation point is far away from the nucleus $(r >> r')$ with a multipole expansion giving:

$$V(\mathbf{r}) = \frac{1}{4\pi\epsilon_0} \left[\frac{1}{r} \int \rho(\mathbf{r}')dv' + \frac{1}{r^2} \int \rho(\mathbf{r}')r'cos(\theta)dv' + \frac{1}{r^3} \int \rho(\mathbf{r}')r'^2 0.5(3cos^2(\theta) - 1)dv' + \ldots \right]. \tag{2.43}$$

The third term in this expansion is the electric quadruple (eQ) term, shown in Eq. 2.32. This term gives information on whether a nucleus its spherical or non-spherical. For the K=0 band when $Q_0 = 0$ the nucleus is spherical, when $Q_0 < 0$ the nucleus is oblate and when $Q_0 > 0$ the nucleus is prolate. The different shapes are illustrated in Fig. 2.7.

2.6.2 Branching ratio

Nuclear levels may decay in more than one way, for example Fig. 2.8 has a level A that can branch (decay) to either level B or level C. The ratio of the probability for a γ-rays to decay to the A or B states are called the branching ratio. The branching ratio is defined by [50]:

$$BR = \frac{P(^E_M\lambda, I_i \rightarrow (f1)}{P(^E_M\lambda, I_i \rightarrow (f2)} = \frac{E_{\gamma 1}^{2\lambda+1} < I_{f1}||M(^E_M\lambda)||I_i >}{E_{\gamma 2}^{2\lambda+1} < I_{f2}||M(^E_M\lambda)||I_i >}, \tag{2.44}$$

where $E_{\gamma 1}$ and $E_{\gamma 2}$ are the energies of the γ-rays, λ is the multipolarity, $P(^E_M\lambda)$ is the probability of a decay and $< I_{f1}||M(^E_M\lambda)||I_i >$ is the reduced matrix transition element from state I_i to I_f.

2.6.3 Mixing ratio

The selection rules allow for a transition to have more than one multipolarity. The ratio of these multipolarities is known as the mixing ratio. For example a $3^+ \rightarrow 2^+$ transition with $\Delta J = 1$ can be M1 or E2. In such a case the transitions are competing and this
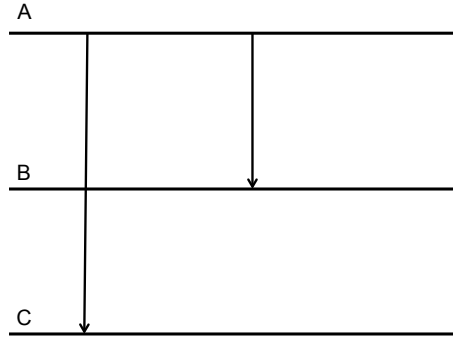
Figure 2.8: A simplified schematic of one level that can decay to one of two lower levels.

needs to be accounted for when fitting the matrix elements to the experimentally observed γ-ray yields. The mixing ratio δ for an E2 and M1 transition is given by [50]:

$$\delta(E_2/M_1) = 0.835E_\gamma[MeV]\frac{<J_1|E_2|J_2>}{<J_1|M_1|J_2>} \tag{2.45}$$

2.6.4 Lifetime

Lifetime measurements provide information on transitional reduced matrix elements. The lifetime can be expressed explicitly by inserting Eqs. 2.5, 2.6 and 2.31 into Eq. 2.3 [50]:

$$\tau = \left(\sum_{\lambda,f} |i^{n(\lambda)}\sqrt{\frac{8\pi(\lambda+1)}{\lambda\hbar((2\lambda+1)!!)^2}\left(\frac{E_\gamma}{\hbar c}\right)^{2\lambda+1}\frac{1}{\sqrt{2I_i+1}}} <I_f||M(^E_M\lambda)||I_i>|^2\right)^{-1}. \tag{2.46}$$

The lifetime is related to the half-life by:

$$T_{1/2} = \tau ln(2) \tag{2.47}$$

2.7 Quadrupole sum rule method

Information on the charge distribution of the nucleus in specific states can be extracted by using the quadrupole sum rule method described in Refs. [51, 52, 53]. By using the quadrupole sum rule method the electric multipole transition operator's $E(\lambda = 2, \mu)$ components can be represented by using parameters Q, the overall quadrupole deformation parameter and δ, which is related to the triaxiality parameter. Q and δ are similar to the parameters used in Bohr's model: the elongation parameter β as discussed in Sec. 2.1.3.2 and the triaxiality parameter γ. The distribution plot for the δ and $<Q^2>$ parameters are shown in Fig. 2.9.
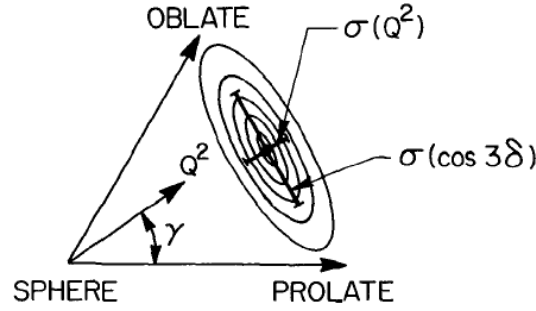
Figure 2.9: Distribution plot for the δ and $< Q^2 >$ parameters required to define the E2 properties [52]. Here σ represents the variance of the properties.

The expectation values of the quadrupole rotational invariants $< Q^2 >$ and $< Q^3 cos(3\delta) >$ can be calculated by using the set of E2 matrix elements. The set of matrix elements are expanded over all possible intermediate states by using Wigner's 6j symbols [38]:

$$\frac{1}{\sqrt{5}} < Q^2 >=< I_i||[E2 \times E2]_0||I_i >=$$

$$\frac{1}{\sqrt{2I_i + 1}} \sum_j < I_i||E2||I_j >< I_j||E2||I_i > \left\{ \begin{array}{ccc} 2 & 2 & 0 \\ I_i & I_i & I_j \end{array} \right\}, \tag{2.48}$$

where $< Q^2 >$ is proportional to the sum of squared E2 matrix elements over the intermediate state that can be reached with one E2 transition from $|I_i >$ to $|I_j >$. This is shown graphically in Fig. 2.10 and presented for the example of calculating $< Q^2 >$ for the 0_1^+ state:

- $2_1^+ \to 0_1^+$ would be the matrix elements: $< 0_1^+||E2||2_1^+ >< 2_1^+||E2||0_1^+ >$

- $2_2^+ \to 0_1^+$ would be the matrix elements: $< 0_1^+||E2||2_2^+ >< 2_2^+||E2||0_1^+ >$.

Similarly, $< Q^3 cos(3\delta) >$ is calculated from the triple product of $E2$ matrix elements where $|I_i >$ is the initial state and $|I_j >$ and $|I_k >$ are the intermediate states:

$$< Q^3 cos(3\delta) >=< I_i||([E2 \times E2]_2 \times E2)_0||I_i >=$$

$$\mp \frac{\sqrt{35}}{\sqrt{2}\sqrt{2I_i + 1}} \times \sum_{jk} < I_i||E2||I_j >< I_j||E2||I_k >< I_k||E2||I_i > \times$$

$$\left\{ \begin{array}{ccc} 2 & 2 & 2 \\ I_i & I_j & I_k \end{array} \right\}. \tag{2.49}$$

This is illustrated graphically in Fig. 2.11. The invariants are calculated exactly for model calculations and approximated from experimental data making them equivalent to
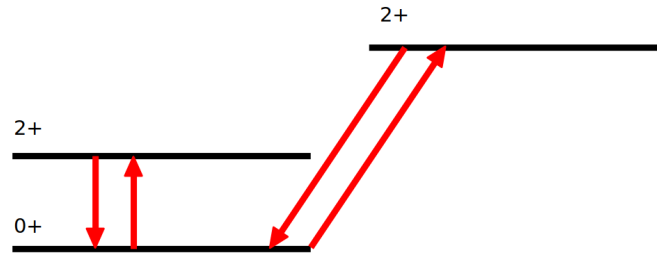
Figure 2.10: Example of the transitions involved in calculating $< Q^2 >$ for the 0_1^+ state. The arrows indicate transition, up arrows signify an excitation and down arrows signify a de-excitation.
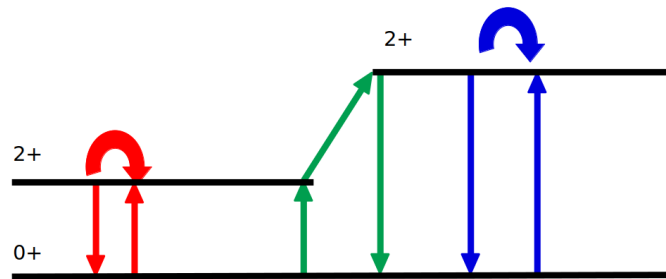
Figure 2.11: Example of the transitions involved in calculating $< Q^3 cos(3\delta) >$ for the 0_1^+ state in even-even nuclei. The arrows indicate transitions, up arrows signify an excitation, down arrows signify a de-excitation and circular arrows indicate de-orientation.

observables. Other deformation parameters such as β and γ can be calculated from the invariant information. β is calculated with [37]:

$$\beta = \sqrt{\frac{Q^2}{q_0^2}}, \tag{2.50}$$

where

$$q_0 = \frac{3}{4\pi} Z R_0 A^{1/3}, \tag{2.51}$$

and A is the atomic number, Z is the number of protons and R_0 is the nuclear radius. The parameter γ can be obtained from the angle between the semi-major and semi-minor axis with:

$$\gamma = \frac{\arccos(\cos(3\delta))}{3} = \delta. \tag{2.52}$$

Chapter 3

Experiment

The experiment of interest is the Coulomb excitation reaction ^{194}Pt(^{14}C,^{14}C')^{194}Pt which was performed together with multiple supporting experiments. The list of all experiments performed for this work, with a short description, is presented below:

- A safe Coulomb excitation reaction: ^{194}Pt(^{14}C,^{14}C')^{194}Pt. A 45 MeV ^{14}C beam with a charge state of 5^+, current of $\sim$ 15 enA ($\sim$ 3 pnA) impinging on a 2 $\frac{mg}{cm^2}$ thick ^{194}Pt target. This was the key measurement and it took $\approx$17 days of data taking.

- γ-ray calibration up to E_γ 4.8 MeV: ^{nat}Zn(p,x)^{xx}Ga reaction. A 8.5 MeV proton beam impinging on a 0.1mm thick ^{nat}Zn target. In this reaction various Ga isotopes were produced, consequently, γ-rays up to 4.806 MeV from ^{66}Ga can be used for the energy calibration. The measurement was performed before and after the ^{14}C run to produce the calibration data that can be used to correct for any peak drift that could occur. This was an activation experiment with 34 minutes of irradiating the target and a counting time of 18.07 hours for the first measurement. The second Ga measurement was performed with 1 hour of irradiation and 24.43 hours of acquisition time. Approximately 42 hours were used for both Ga experiments.

- γ-ray calibration up to 7 MeV: ^{13}C(d,p)^{14}C transfer reaction. A 6 MeV deuteron beam impinged on a 1 $\frac{mg}{cm^2}$ thick ^{13}C target. This reaction populates states in ^{14}C. The decay of ^{14}C gives the response function and the efficiency calibration for the detectors in the 6-7 MeV energy range. The data were collected for 4.3 hours before and 5.7 hours after the ^{14}C experiment and a total of 10 hours of beam time was used.

- A safe Coulomb excitation reaction: ^{194}Pt(^{12}C,^{12}C')^{194}Pt. A 48 MeV ^{12}C beam bombarded a 2 $\frac{mg}{cm^2}$ thick ^{194}Pt target. This reaction provided the data necessary to developed and test the software. A total beam time of 16.27 hours was used for this experiment.

- Calibration with a certified ^{152}Eu source. Before and after the ^{14}C experiment the source was placed in the target position for the energy and efficiency calibration. The total acquisition time is 3.97 hours.

- Particle detector calibration. A ^{14}C beam of 30, 38, 45 and 52.6 MeV energies where used.

- Background measurement: The natural background was measured before and after the ^{14}C experiment to produce spectra that could be used for background subtraction. The total acquisition time was 17.57 hours.

3.1   Particle Accelerator

The John D. Fox Superconducting Linear Accelerator laboratory at the Florida State University, USA, has two possible ion injection sources. The source can be injected from either a Source of Negatively Charged Ions by Caesium Sputtering (SNICS) [54] or from a radio-frequency (RF) discharge source.

The ^{14}C source is found in a solid form so it is injected to the accelerator system using the SNICS method. A schematic of the SNICS used is shown in Fig. 3.1(a). Caesium is vaporised in the oven, then ionised using the hot ioniser and accelerated towards the cathode. A beam of negatively charged ions is created by the vaporised caesium that hits the cathode (in this case the cathode is made of ^{14}C material), and "sputter" the particles to form a beam in the process.

The RF discharge source uses gaseous materials to produce a beam. A schematic of this with a He source is shown in Fig. 3.1(b). The Ga experiment used a proton beam and the ^{13}C experiment used a deuteron beam. Both experiments used the RF-discharge source injector. The gas is ionised through heat and a time varying electric field is applied to accelerate the particles. The ionised particles will exchange charge with the Rb vapour, becoming negatively charged. The negative ions are then focused and directed into the Tandem accelerator.

From either of the sources, a beam of negative ions is accelerated across towards the positive high voltage at the centre of the tank where the C stripper foil is placed. The ions will pass through the stripping foil, which removes (n+1) electrons. The beam now contains positive ions that are further accelerated away from the positive high voltage at the stripper foil. A picture of the 9 MV Tandem is shown in Fig. 3.2.

(a) SNICS   (b) RF-discharge
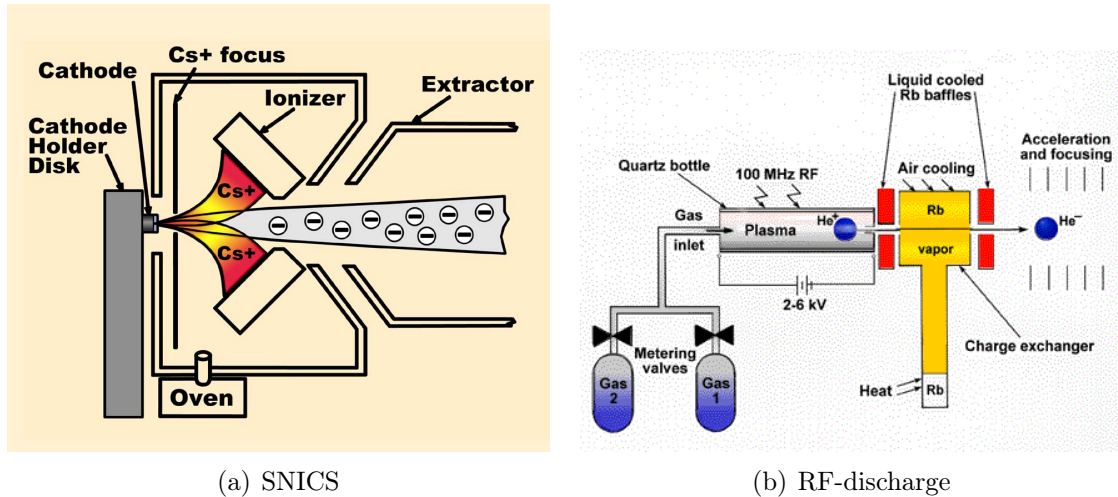
Figure 3.1: The SNICS injection source (a) and the RF-discharge injection source (b) [55].

Figure 3.2: 9 MV tandem accelerator at John D. Fox Superconducting linear Accelerator Laboratory.

3.2 Setup

This work was performed in a collaboration between many parties and countries: iThemba LABS, Stellenbosch University, University of Western Cape, University of Oslo, Florida State University (FSU), Lawrence Berkeley National Laboratory (LBNL), Lawrence Livermore National Laboratory (LLNL) and the United States Army Research Laboratory in Washington, USA. The experimental setup was assembled between January-March 2017 and the measurements were performed at the John D. Fox Superconducting linear Accelerator laboratory at FSU between 6-27 March 2017.

The layout of the John D. Fox Superconducting linear Accelerator laboratory at FSU is shown in Fig. 3.3. The facility operates on a two stage accelerator basis: ions can be
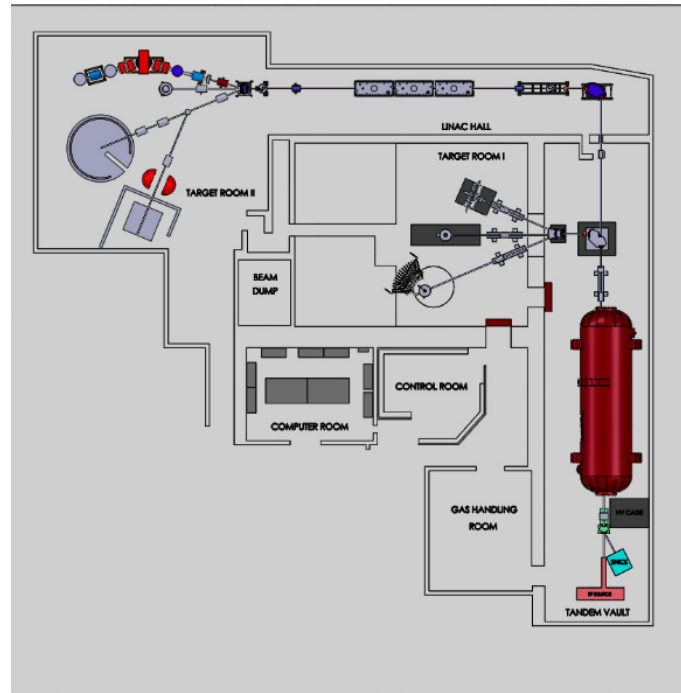
Figure 3.3: The layout of the John D. Fox Superconducting linear Accelerator laboratory at FSU [55].

accelerated by a 9 MV Super-FN tandem van de Graaf accelerator and if needed further accelerated by a 8 MV superconducting linear accelerator (linac). For the experiments performed the linac was not needed to reach the required energies and target room 1 was utilised.

Figure 3.4(a) shows the setup upon arrival at FSU and the completed setup is shown in Fig. 3.4(b). The 4 large volume 889mm x 203mm $LaBr_3(Ce)$ (referred to as the Oslo $LaBr_3(Ce)$ for short) were loaned from the University of Oslo, Norway. The 2 BGO suppressed HPGe Clover detectors and 1 single crystal HPGe detector were provided by FSU. A S2 particle detector was also provided by FSU for the $^{13}C(d,p)$ experiment. The scattered particles must be stopped in the detector so a 1002μm thick S2 detector with 16 sectors and 48 rings was used. The S2 particle detector is the only difference between the setup of the $^{13}C(d,p)$ and safe Coulomb excitation experiments. Two 127mm x 64mm $LaBr_3(Ce)$ (referred to as the Army $LaBr_3(Ce)$ for short) were loaned from the United States Army Research Laboratory in Washington, USA. A 140μm S3 silicon detector with 32 sectors and 24 rings was loaned from the University of Western Cape, South Africa. The target chamber and the electronics for the silicon detector were loaned from iThemba LABS, South Africa.

Four Pixie 16 XIA cards [56] where used to digitise the signals from the detectors. All the outputs from the Pixie cards are then stored on a hard drive to be analysed offline.

(a) before
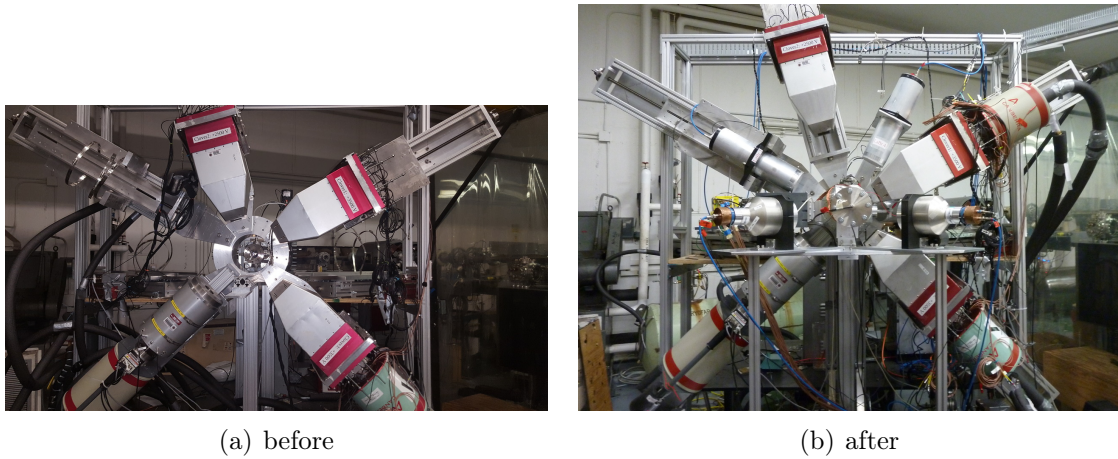
(b) after

Figure 3.4: The experimental setup upon arrival (a) and after the assembly and setup were completed (b).

All four Pixie 16 cards provide a total number of 64 channels that can be used to record the information. A S3 silicon detector has 24 rings on one side and 32 sectors on the other. This is equivalent to 768 "pixels" that can be used to determine the position of the particle when it hits the S3. A PCB board is attached to the S3 detector to split the individual signals from the detector into separate cables. In total the S3 detector needs 56 channels and adjacent sectors where combined to form 16 sectors instead of 32. This left 4 channels available for the $LaBr_3(Ce)$, 8 channels for the clovers, 2 for the BGOs, 1 channel for the FSU HPGe and 24 for the S3 rings. The HPGe clovers were Compton suppressed during the data taking.

Initially, a ^{206}Pb target was intended to be used for the experiment since the Coulomb force increases proportionally to Z_{target}, however a huge background in the low energy particle spectrum was observed (originating from the fusion evaporation reaction on oxygen and carbon target contaminants), consequently many unwanted γ-ray lines were observed. The count rate was very high with an estimated data rate of 10 GB/hour. Due to the high count rate and unresolvable spectrum the target was changed to ^{194}Pt. The 1 mg/cm^2 ^{13}C and 2 mg/cm^2 ^{194}Pt targets used for the experiments are shown in Fig. 3.5 together with the ^{206}Pb and ^{58}Ni targets. The ^{194}Pt target was made at iThemba LABS by Dr. N. Kheswa through rolling. On the ^{194}Pt target the beam spot can be seen as a dark spot on the target. The ^{58}Ni target was intended as a backup and was not used.

The angles to the center of the crystals of the γ-ray detectors were determined as shown in Figs. 3.6(a) and 3.6(b). The figures are merely a visual representation of the angles. The ϕ angles from the silicon S3 detector were taken from the 24 rings. Each ring is $\approx$ 0.88mm wide and is separated from the neighbouring ring by 0.1mm. The opening hole in the middle of the detector has a radius of 11mm and the detector was placed 32 ± 1

(a) (b)
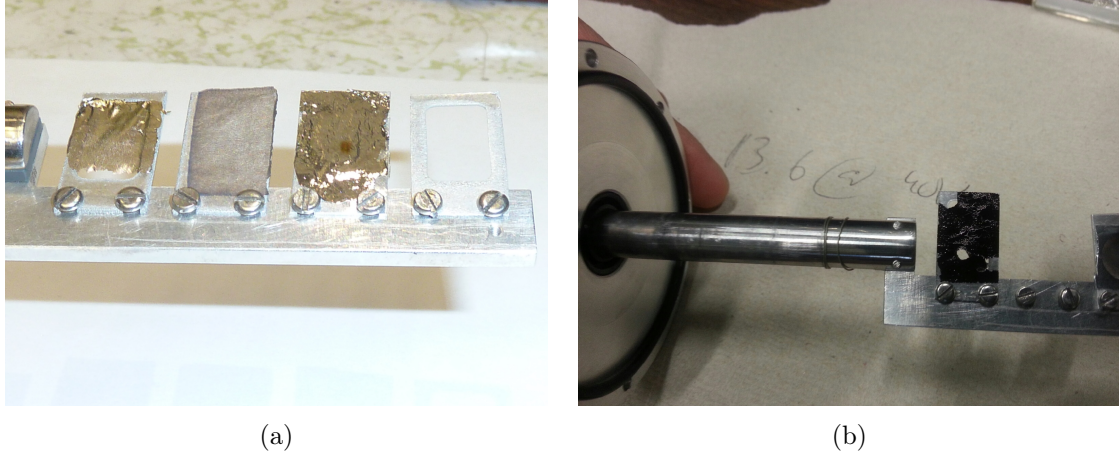
Figure 3.5: Targets prepared for the experiment are from left to right: ^{58}Ni (not used), ^{206}Pb (not used), ^{194}Pt and an empty frame (a). The ^{13}C target had to be mounted separately (b).

mm from the target, upstream. The θ angle can then be calculated using the following equation:

$$\theta_i = \frac{tan^{-1}\left(\frac{r_{i,min}}{d}\right) + tan^{-1}\left(\frac{r_{i,max}}{d}\right)}{2}, \tag{3.1}$$

where $r_{i,min}$ is the inner distance (from the center of the detector), $r_{i,max}$ is the outer distance of a specific ring and d is the distance between the target and the particle detector. The ϕ angles from the particle detector were taken from the S3 sectors. Figure 3.6(c) is a visual representation of the ϕ angles and sector division. The S3 sectors were facing upstream and the rings downstream. The PCB connector was attached to the cables towards $\phi = 0°$. The distances between the target and detectors and their relevant angles are shown in Tab. 3.1. The S3 particle detector angles are shown in Tab. 3.2.

3.3 Electronics

The typical signal used in a traditional analog chain is shown in Fig. 3.7. The weak signal from the detector is amplified with the pre-amplifier to provide a signal that has a sustainable signal to noise ratio. This enables the signal to travel tens (generally up to a hundred) meters with an acceptable signal to noise ratio [57]. The signal can then be shaped further, for example with a fast amplifier that is used to measure time or a shaping amplifier that is generally used to measure the energy. The voltage amplitude of the signal is used for the energy measurement. A constant fraction (CFD) or leading edge discrimination (LED) is used to determine if the signal is something of value or if it should be discarded as background [57]. The signal coming from the discriminator will be a logic pulse. For this experiment all the shaping of the signal is done digitally by the

Table 3.1: The distance from the γ-ray detectors to the target along with each detector angles.

Detector	Distance (mm)	θ (deg)	ϕ (deg)
LaBr$_3$(Ce) 1	246 (5)	90	29
LaBr$_3$(Ce) 2	248 (5)	135	0
LaBr$_3$(Ce) 3	219 (5)	135	180
LaBr$_3$(Ce) 4	237 (5)	90	118
Clover 1 red	234 (5)	85	146
Clover 1 blue	234 (5)	85	156
Clover 1 green	234 (5)	95	146
Clover 1 black	234 (5)	95	156
Clover 3 red	231 (5)	95	226
Clover 3 blue	231 (5)	95	216
Clover 3 green	231 (5)	85	226
Clover 3 black	231 (5)	85	216
Single Crystal HPGe	250 (5)	90	314

Pixie-16 card.

The back-scattered projectiles are detected when they interact with a MICRON semiconductor S3 particle detector [58]. The interaction process and the way an electric signal is produced will be discussed in detail in section 3.4. The signal coming from the detector is typically small (mV) and needs to be amplified to ± 1 V. The signal path for the particle detector is the following: first, it is generated in the S3 detector, then amplified in a Mesytec MPRS-16 pre-amplifier, digitised and shaped in the Pixie-16 card and then stored on a disk to be further analysed offline.

The γ-rays following the decay of the states populated in the reactions described in this thesis are detected in the scintillation LaBr3(Ce) detectors or in the semi-conductor HPGe detectors. Similar to the particle detector signal path, the signal is generated in a detector crystal, amplified by internal pre-amplifiers, digitised by a Pixie card and stored for offline analysis. The layout of the electronics is shown in Fig. 3.8. All gates and coincidences are applied during the offline analysis.

A time window of 10μs was used and all events in this time window are recorded. The time window starts when the pulse amplitude reaches a trigger threshold. A leading edge trigger was used in this work. A threshold is typically set between 10-20% of the signal amplitude, but it depends on the amount of electronic noise. The trigger will reduce electronic noise and prevent low energy events from being recorded. This type of trigger

Table 3.2: The data for calculating the angles from the S3 particle detectors' rings. Two adjacent sectors were combined.

ring	r_{min} (mm)	r_{max} (mm)	θ (°)	sectors	ϕ (°)
1	11.5	12.4	159.5	32+1	270
2	12.5	13.4	157.9	2+3	247.5
3	13.5	14.3	156.4	4+5	225
4	14.4	15.3	154.9	6+7	202.5
5	15.4	16.3	153.5	8+9	180
6	16.4	17.3	152.1	10+11	157.5
7	17.4	18.3	150.7	12+13	135
8	18.4	19.3	149.4	14+15	112.5
9	19.4	20.3	148.1	16+17	90
10	20.4	21.2	146.8	18+19	67.5
11	21.3	22.2	145.6	20+21	45
12	22.3	23.2	144.4	22+23	22.5
13	23.3	24.2	143.2	24+25	0
14	24.3	25.2	142.1	26+27	337.5
15	25.3	26.2	141	28+29	315
16	26.3	27.2	139.9	30+31	292.5
17	27.3	28.1	138.9		
18	28.2	29.1	137.9		
19	29.2	30.1	136.9		
20	30.2	31.1	136		
21	31.2	32.1	135.1		
22	32.2	33.1	134		
23	33.2	34.1	133.4		
24	34.2	35.0	132.6		

(a) θ angles

(b) ϕ angles

(c) S3 θ angles
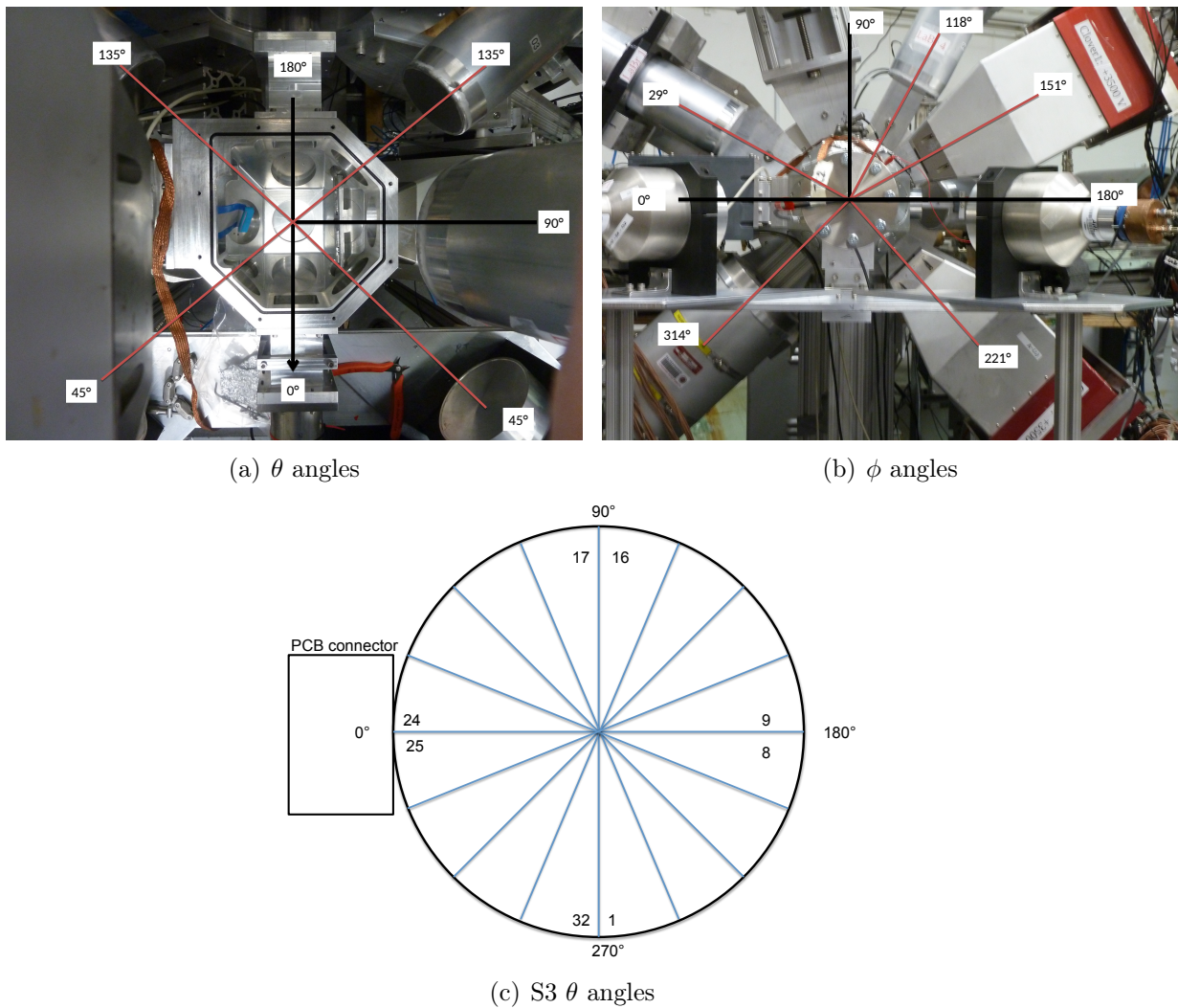
Figure 3.6: Visual representation of the angles of the detectors used in the Doppler correction calculations. The beam is moving out of the page in panel (b).
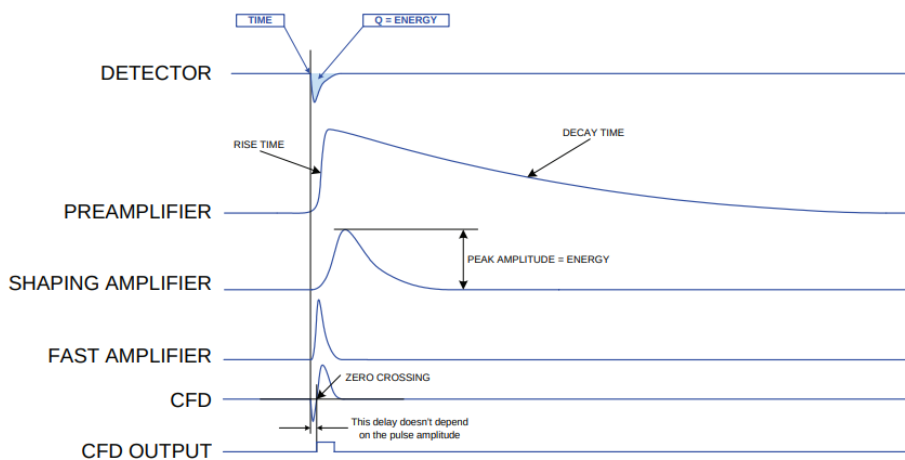
Figure 3.7: The signals used in a traditional analog chain taken directly from Ref. [57].
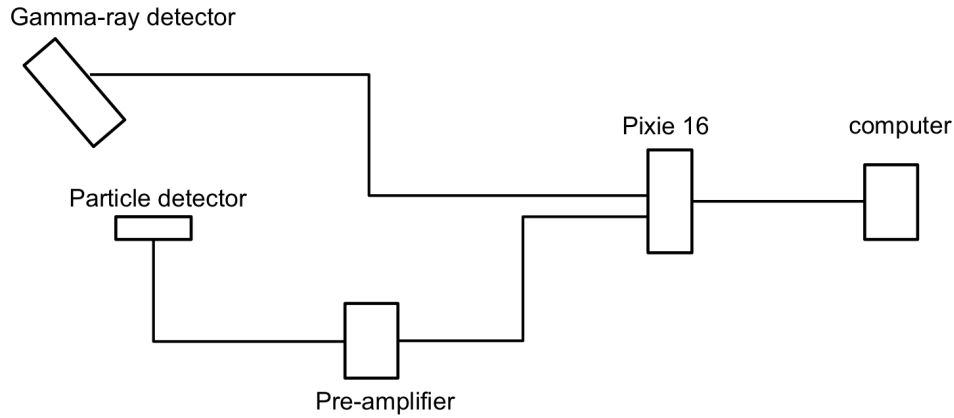
Figure 3.8: Layout of the electronics used.
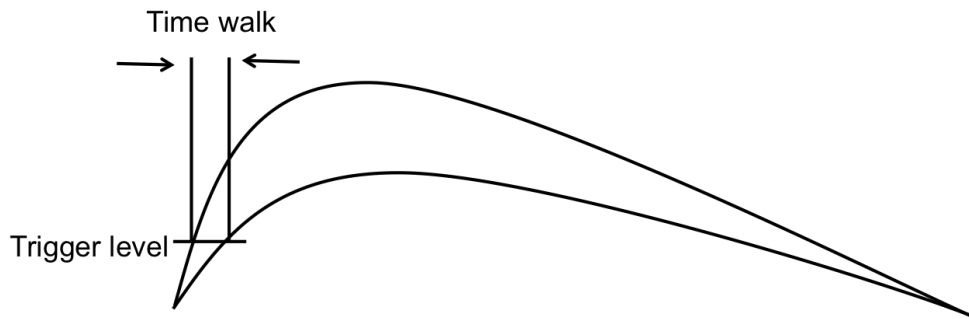
Figure 3.9: The amplitude at the trigger level may be different for signals with different amplitudes, this is known as the time walk effect.

is in general faster compared to the other timing methods (for example the constant fraction triggers), but the amplitude of each signal at the trigger level may be different which may lead to a time walk effect. This is illustrated in Fig. 3.9.

3.4   Detectors

The available radiation detectors come in many shapes, sizes and materials. Detectors are sensitive to the interaction with any of the following fields: γ-rays, electrons, neutrons or charged particles, resulting in a measurable charge deposition. The deposited charge must then be collected in a form that the electronic equipment connected to the detector can interpret as a signal. Different types of radiation interact in various ways with individual types of detector material. In this section the $LaBr_3(Ce)$, HPGe and silicon detectors will be discussed and how the relevant radiation can interact with them to form a signal. All information summarised below can be found in more detail in Ref. [59].

3.4.1   Interaction

3.4.1.1 γ-rays

The γ-rays are electromagnetic radiation. A signal is produced indirectly as the detector collects the energy from the interactions of the γ-ray with the detector medium. For HPGe and Si detectors the charges produced by the energetic electrons released by the interaction are collected. For LaBr$_3$(Ce) the light from the de-excitation of ionised molecules are collected. Depending on the energy, the γ-rays can interact with matter primarily in three ways: photoelectric absorption effect, Compton scattering and pair production.

The photoelectric absorption effect occurs when a γ-ray interacts with an atom and is completely absorbed by it. In its place a photoelectron is emitted with an energy proportional to the energy of the absorbed γ-ray. For γ-rays of hundreds of keV's most of the γ-ray energy will be carried away by the photoelectron. This process leaves the atom ionised and it can later capture a free electron or rearrange the electrons to fill the electronic vacancy. When the electrons are rearranged, an X-ray is emitted. In most cases the X-ray will undergo photoelectric absorption before contributing to the signal. Photoelectric absorption is dominant up to a few hundreds of keV.

Compton scattering is a γ-ray scattering off an electron. Depending on the angle of the scattering, the electron receives a portion of the γ-ray energy in a form of kinetic energy. For small scattering angles the transferred energy is also small. The γ-ray can undergo multiple scattering events before having deposited its total energy. It is also possible that the γ-ray escapes the detector before depositing all of its energy. These processes form the Compton background. The highest energy γ-rays deposit in a single Compton scattering event before escaping the detector forms the Compton edge. This occurs when the γ-ray scatters backward at 180°. The Compton scattering formula is given by [59]:

$$hv' = \frac{hv}{1 + \frac{hv}{m_0 c^2}(1 - cos\theta)}, \tag{3.2}$$

where mc^2 is the rest mass energy of an electron (511 keV), hv is the energy of the incoming γ-ray and hv' is the energy of the scattered γ-ray.

If the incident γ-ray has more than the threshold 1.022 MeV energy, corresponding to twice the rest mass energy of an electron, pair production is possible. Pair production is dominant between 5-10 MeV. The incoming γ-ray interacts with the electric field of the nucleus and an electron-positron pair is produced. This interaction happens in the intense electric field near the protons. Any energy above the required threshold of 1.022

MeV energy will be transferred as kinetic energy of the electron-positron pair. Positrons will slow down and combine with a free electron and annihilate by emitting two annihilation photons in opposite directions. The annihilation photons will be absorbed by the detector by one of the methods described above. It is possible that one or both of the annihilation photons escape the detector. If one escapes, the spectra will show the so-called single escape peak and the energy deposited will be the incident γ-ray energy minus 511 keV. If both annihilation photons escape, it is a double escape event and 1.022 MeV of energy will be left undetected.

The size of the detector has a large influence on the probability that an annihilation photon can escape. The mean free path of the annihilation photon is generally several cm in detectors mediums. If the detector is small (1 or 2 cm) then all annihilation photons will escape and only single interactions events will be recorded. This means that only double escape events, Compton scattering and photoelectric absorption will be recorded. If the interaction happens near the centre of a detector, larger than several cm, a large portion of γ-rays will undergo full energy deposition. In practice, some interactions will take place close to the surface and some γ-ray energy will be left undetected. A larger detector has a larger probability to register the full energy. Very large detectors are very expensive and rarely used. Intermediate size detectors are most commonly used where Compton background, single and double escape events and full energy deposition events are all present.

3.4.1.2   Charged particles

When a charged particle interacts with a semi-conductor detector it will interact simultaneously with many electrons in its close proximity. Due to the Coulomb force the nearby electron will be excited to a higher level or it will receive enough energy to escape the atom. This will happen with all atoms around the charged particle path. After each interaction the charged particle will have less energy until finally all the energy is deposited into the detector.

3.4.2   Scintillation detector

3.4.2.1   LaBr$_3$(Ce)

The LaBr$_3$(Ce) detectors, shown in Fig. 3.10, are scintillation detectors. They become fluorescent when incoming ionising radiation interacts with the detector medium. Fluorescence is the prompt emission of light and should not be confused with phosphorescence or delayed fluorescence. Phosphorescence or delayed fluorescence also emit light but the

Figure 3.10: A LaBr$_3$(Ce) crystal (left) and photo multiplier tube (right).

emission time is generally longer. Light that is emitted after the prompt emission forms the background and is indistinguishable from random noise.

Photons which are emitted as a result of the interaction in the detector medium are converted into electrons and then amplified. This is done in a photo-multiplier tube (PMT). The process of converting photons into electrons in the photocathode occurs in three sequential steps. First, the photon is absorbed in the photoemissive material and the energy is transferred to an electron. This occurs by exciting the electron from the valence band into the conduction band. Once an electron is in the conduction band it has sufficient energy to move through the material and an electric current is induced. Secondly, the electron moves to the surface of the photocathode. It must reach the surface in a short time (ps) before the phonon interactions have reduced its energy to a point where the next step is not possible. The electron will encounter collisions with other electrons and will still need to break the potential barrier once it has reached the surface. Lastly, the electron escapes from the surface of the photocathode if it has sufficiently high energy. Only a few electrons (hundreds) are involved in a single photoelectron pulse. This is not enough to produce a signal which can be read by typical electronics. The dynodes provide a multiplier section where the few initially emitted electrons turn into a cascade of 10^7 or 10^9 electrons. The number of cascade electrons depend on the initial energy, conversion factor and voltage. The cascade electrons are generally enough to produce a pulse which can be processed by the electronic modules. The electrons are finally collected by the anode. A PMT is illustrated in Fig. 3.11.

The scintillation material can have a nonlinear response caused by numerous interactions leading to the production of many electrons of different energies. Since the response of the
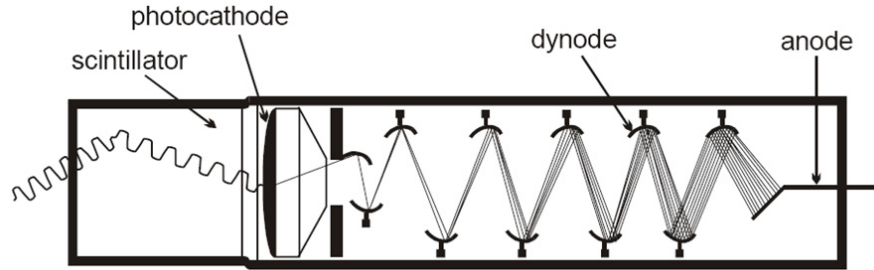
Figure 3.11: Diagram of a photo-multiplier tube [60].

crystal is not linear with electron energy, the total light yield differs from event to event. This effect can have a large impact on the energy resolution and the energy calibration. For this, a more complex polynomial calibration function needs to be used.

Due to their high brightness with >65000 photons/MeV, high density material (5.1g/cm^3) and fast decay time of 16 ns [61] the LaBr$_3$(Ce) detectors are highly valuable and widely used in nuclear spectroscopy. A major drawback to LaBr$_3$(Ce) is the intrinsic activity from the radioactive ^{138}La and ^{227}Ac crystal impurities which account for 1-2 counts/cm^3· s. The effect the mentioned impurities have on the γ-ray spectra and how it is dealt with is discussed in chapter 4. LaBr$_3$(Ce) material is hygroscopic, hence the absorbed moisture can form a layer on the surface that absorbs scintillation light, which consequently can decrease the effective scintillation of the crystal [62]. When it absorbs moisture it can also change the crystal causing cracks. This means all aspects of the crystal growth, storing, transfer, cutting, polishing and characterisation becomes more challenging. The LaBr$_3$(Ce) crystal is hermetically sealed in an aluminium casing with a quartz light guide window. Optical grease is applied between the quartz light guide and the window (for example boron silicate) of the PMT. The optical grease will have a refractive index that allows the light to pass through the quartz and the boron silicate window and not refract out of the PMT.

3.4.2.2   BGO

Another scintillation detector commonly used is Bi$_4$Ge$_3$O$_{12}$ (BGO). This material has a high density of 7.13 g/cm^3 [59] and due to the large atomic number of Bismuth (Z=83), the probability for photoelectric absorption of γ-rays is high in BGO material. Therefore, a BGO crystal is typically a very good counting detector.

The light yield is very low compared to other detectors and it has a refractive index of 2.15 [59]. This gives a BGO detector rather poor energy resolution. However, the
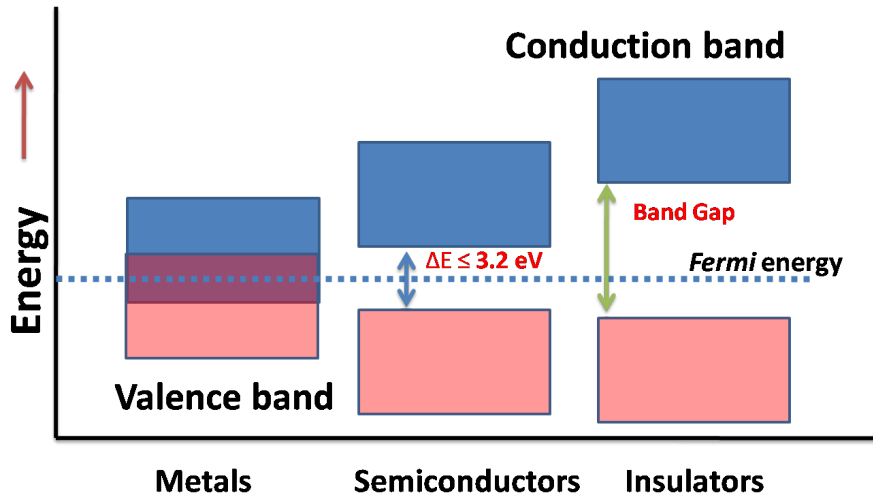
Figure 3.12: Band structure of a conductor, semi-conductor and insulator [63].

high efficiency of this detector makes it a very good shield for other detectors. A BGO detectors can be placed around other detectors, for example a HPGe crystal. It can then detect the single escape, double escape or Compton scattered γ-rays that escaped the HPGe detector. These escape events can then be vetoed from the HPGe spectrum resulting in a significant background reduction.

3.4.3 Semi-conductor

Electrons in solids occupy different energy bands. The valence band corresponds to bound electrons. The next higher-lying conduction band consists of electrons that can move through the atomic lattice. Typically, only electrons with an energy close to the Fermi energy can be involved in the conduction process. The Fermi level is the energy of the highest level occupied by electrons. Incoming γ-rays will excite electrons from the valence band to the conduction band. The band gap is the energy separating the valence and conduction band. It is different for insulators, conductors and semi-conductors. For insulators electrons need usually about 5 eV to cross the band gap, whereas in a conductor only an incremental amount of energy is required. The band structure is shown in Fig. 3.12.

When the radiation interacts with a semi-conductor material it excites an electron from the valence band into the conduction band. This creates an electron-hole pair. Under the effect of an electric field the electrons will be accelerated towards the anode and the holes towards the cathode. In High Purity Germanium (HPGe) detectors or in silicon detectors the hole mobility is within a factor of 2 or 3 of the electron mobility. In HPGe and silicon detectors the complete integration of the current form the output pulse (the mobility of the holes is one of the factors that make a semi-conductor slower compared

(a)

(b)
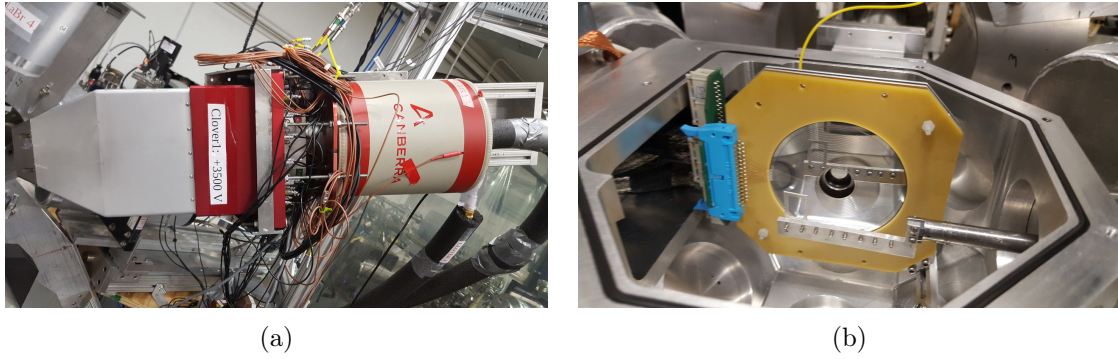
Figure 3.13: High purity Germanium clover detector with a BGO shield (left) and S3 silicon detector in the chamber (right). The PCB board can be seen attached to the S3.

to a scintillator). A HPGe clover detector with its BGO shield and S3 silicon detector are shown in Fig. 3.13. A HPGe clover has four single crystals and is commonly used in conjunction with a BGO anti-Compton shield. If a BGO detects γ-rays a short time ($\sim$ ns) after a γ-ray is detected in one of the HPGe crystals, that event is ignored. This reduces the Compton background by removing events where energy was just partly deposited into one of the crystals.

Semi-conductor detectors can generally be divided into 2 groups: n-type and p-type. P-type symbolise that the material is doped with electron accepting impurities. N-type material is doped with electron donor impurities. N-types readily give electrons and p-types readily accept electrons. This means that in a p-n junction there is a potential difference and charge carriers will move across the junction. This causes negative ions to form at the n-type and positive ions to form at the p-type. This creates an electric field that forms a depleted region. In the depleted region there are no free electrons or holes and the exchange of electrons is inhibited. This is illustrated in Fig. 3.14. A voltage bias can be applied to increase the depleted region to cover the whole active region of the detector. The only way to make an electron-hole pair is by ionising radiation that interacts with the detector. The electron-hole pair is quickly swept away by the electric field which forms an electric pulse. A pre-amplifier then amplifies the pulse so that it can be processed by electronics.

In order to efficiently collect the electrons and holes in semi-conductors a large electric field (thousands of volts for HPGe clovers) has to be applied. Since all detectors have some conductivity a leakage current is observed. The leakage current may drown small signal currents following an ionising event and it is a cause of background noise. Contamination of the surface or radiation damage may cause the leakage current to increase. Radiation can cause an atom to be displaced in the lattice. This can trap the charge carriers and will cause incomplete charge collection. The loss will also vary event-to-event depending on
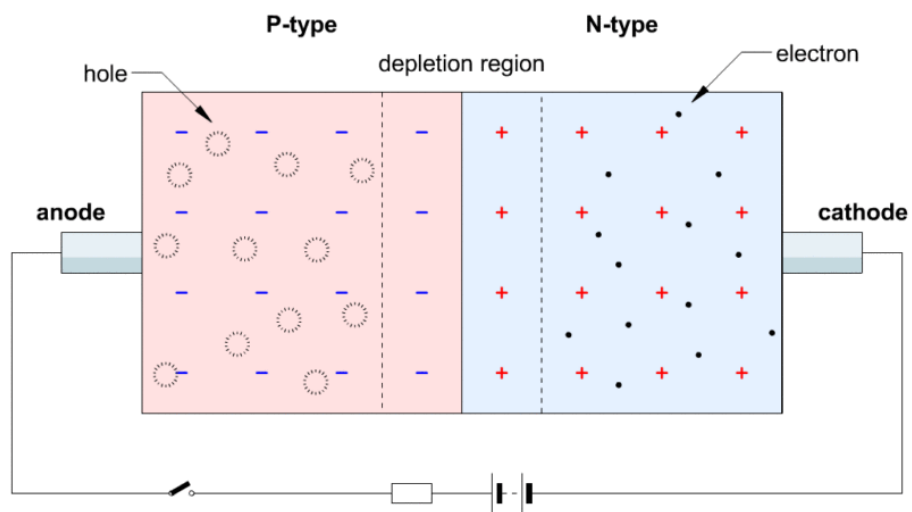
Figure 3.14: Schematic showing the p-n junction [64].

the position of the interaction. This can cause a response of the detector with asymmetric peak shape and worsen the energy resolution.

Chapter 4

Analysis

All the acquired data contain 3 types of information: time, energy and position of the interaction. The data are converted into a TTree format where each type of information is stored in its own "leaf", an indexed row. Let's consider the energy leaf as an example. It may have the following sequence of numbers: 0 3000 125 1400. 0 is the index number, 3000, 125 and 1400 are the energy values corresponding to the signal amplitudes from the γ-rays or particle detectors. It is important to note that index 0 of the energy leaf corresponds to index 0 in the time and position leaves. The combined information of the first entry from all the three leaves for a time window is illustrated in table 4.1. For the analysis of the raw and sorted data the ROOT [65] framework is used to sort the data event-by-event.

4.1 Timing

The timing information is very important since it is the biggest determinant for selecting coincidence events and so-called "good" or "bad" events. All the events in a given event time window of 10μs are sorted according to the time. It should also be noted that time always starts from 0 for each event and each channel is 10 ns wide. The first particle or the first γ-ray detected will have time equal to 0 and all events for the next 10μs are recorded. Based on the time information, the coincidence and "good" or "bad" γ-rays will be identified, validated, subtracted or excluded as discussed in Sec. 4.6. Since

Table 4.1: Simplified data format.

leaf	index	first entry	second entry	third entry
energy	0	3000	125	1400
time	0	0	10	600
position	0	2	2	8
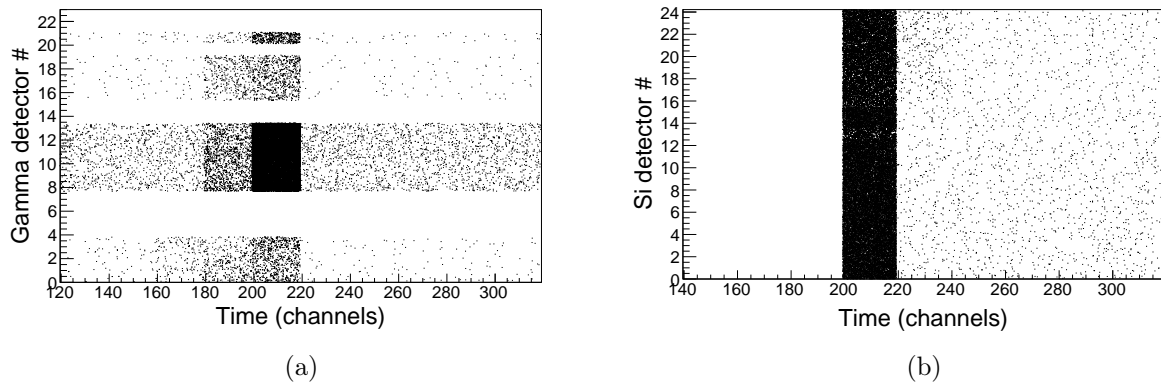
Figure 4.1: The 1 particle + 1 γ-ray (p-γ) coincidence time information for all the γ-ray detectors are shown in (a): 0-4 and 15-19 corresponds to Clover crystals, 8-13 the LaBr$_3$(Ce) detectors are shown and 21 to the single crystal. The time information for the particles from the S3 detector's rings detector are shown in (b). The black strip is the correlated events.

digital electronics was used in the present experiment, the timing of the detectors are expected to coincide. Figure 4.1(a) shows the 1 particle + 1 γ-ray (p-γ) coincidence time information for all the γ-ray detectors. Figure 4.1(b) shows the time information for the particles from the S3 detector's rings, most of the single particles are detected within 200 ns. The time peaks (black strip) are indeed aligned between channel 200-220 and no time calibration is required for the S3 particle or γ-ray detectors.

The timing peaks are artificially aligned at channel 200, so channel number 200 corresponds to time equals to 0. For convenience, in this section the time is presented in channels. The timing spectra of single γ-ray events are shown in Fig. 4.2, for the HPGe clover in panel 4.2(a), the single crystal HPGe in 4.2(b), the Army LaBr$_3$(Ce) in 4.2(c) and the Oslo LaBr$_3$(Ce) in 4.2(d). The peak at 200 is the prompt peak containing all the interesting information. The second peak that can be observed in all the time spectra are events coming from the beam stop that is only ≈ 1.5 m away. ^{14}C traveling at $\approx 7\%$ of the speed of light will take ≈ 80 ns to travel 1.5 m. The returning γ-ray (traveling at the speed of light) only needs 5 ns to cover the 1.5 m. The time spectrum of the Army LaBr$_3$(Ce) shows a second peak only 40 ns away from the prompt peak. That is because the Army LaBr$_3$(Ce) was positioned at forward angles, so the flight path to the beam stop was smaller.

The single γ-ray events that are measured are of little interest because it is difficult to distinguish background from ^{194}Pt or ^{14}C events. The p-γ coincidence events are required, because the added particle information can be used to distinguish between background and possible ^{194}Pt or ^{14}C events. The particle information is also required for Doppler correction, this will be discussed in Sec. 4.7.

(a) Clover

(b) Single Crystal

(c) Army LaBr$_3$(Ce)
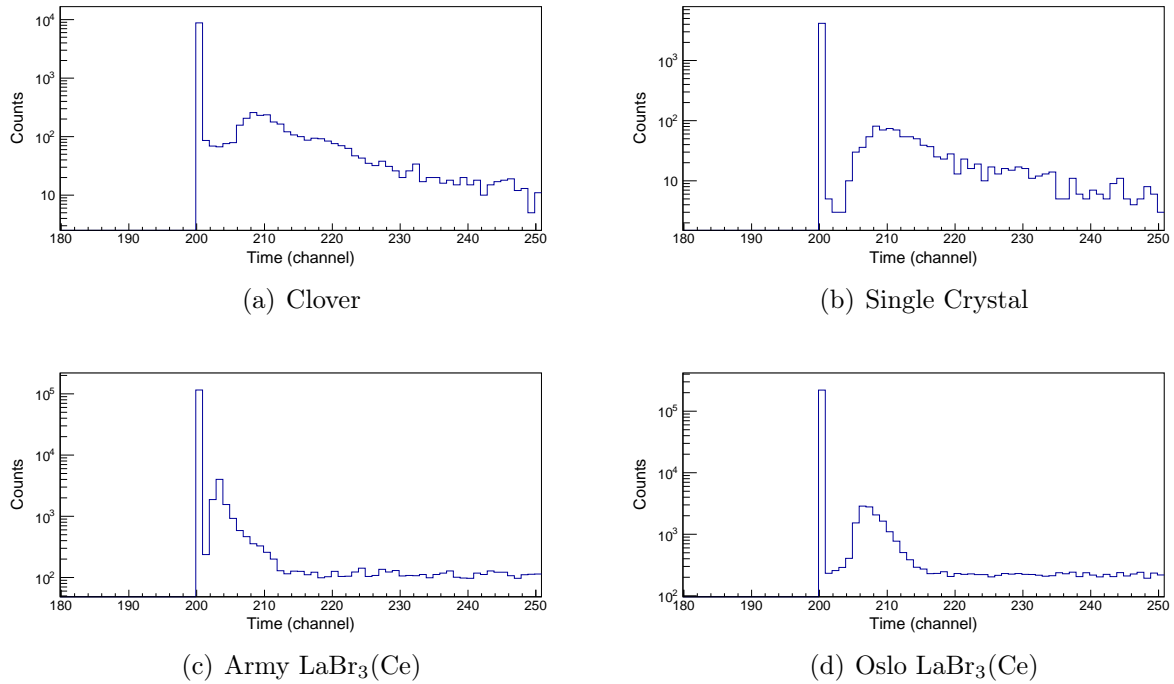
(d) Oslo LaBr$_3$(Ce)

Figure 4.2: The different time spectra for the single γ-ray spectra for a HPGe clover (a), HPGe single crystal (b), Army LaBr$_3$(Ce) (c) and Oslo LaBr$_3$(Ce) (d).

The "good" p-γ coincidence events are selected based on the time between a "good" particle hit and a corresponding "good" γ-ray signal. Only events with the particle and γ-ray observed in the prompt peak are considered as "good" events. The p-γ time spectra for one detector is shown in Fig. 4.3(a). The width of the prompt peak differs between reactions, for the example shown in Fig. 4.3(a) only p-γ events within 16 channels (160 ns) are taken as a "good" event. For the software optimisation and testing purposes the 0 channel of the p-γ time spectrum is artificially set to 1000. The prompt gate is consequently set between channels 1000 and 1016. Two p-γ background gates are taken and summed: one between channel 300 and 900, the other one between channel 1300 and 1900. The background spectrum is then normalised to the prompt spectrum and subtracted.

Another way to remove unwanted events is to make sure that both, the ring and the sector detect 1 particle each within 100 ns. The unwanted events could be due to electronic noise or multiple particles hitting the particle detector in different places. By placing a time gate between channel 195 and 205 on the time difference between a ring and sector most unwanted events can be eliminated. The time difference between a ring and sector for the S3 is shown in Fig. 4.3(b).

(a) P-γ time

(b) Ring-sector time
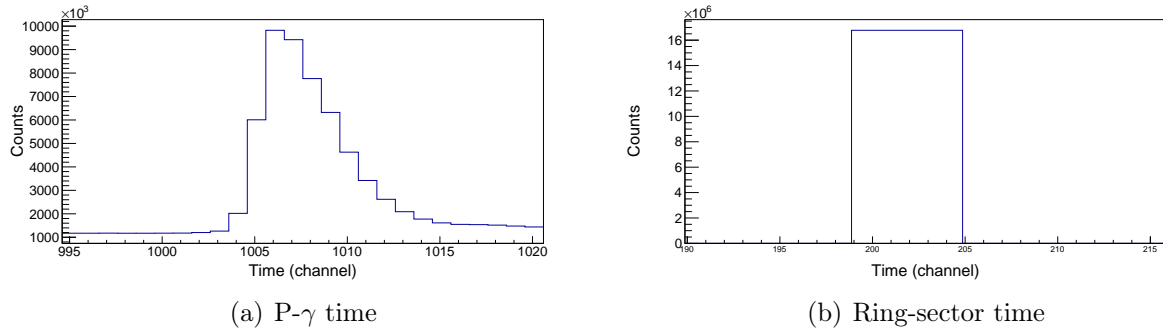
Figure 4.3: The p-γ time difference (a) and the time difference between a ring and sector event (b).

(a)

(b)
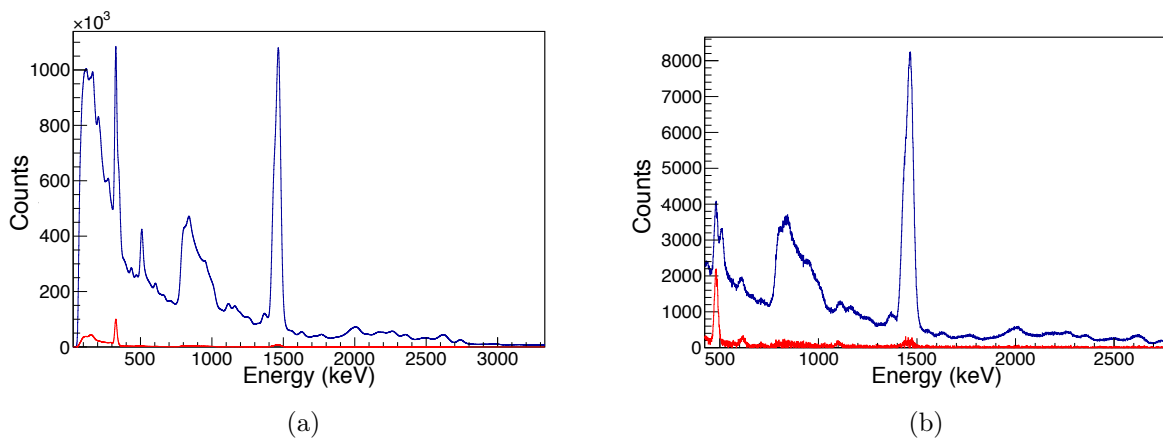
Figure 4.4: Singles spectra shown in blue and p-γ gated spectra shown in red (a). P-γ gated spectra shown in blue and background subtracted p-γ gated spectra shown in red (b).

The results of applying the time conditions are tested step-by-step on a LaBr$_3$(Ce) detector at θ=90° for a subset of the ^{194}Pt(^{14}C,^{14}C') data. The single γ-ray spectrum with no gates applied is presented in blue in Fig. 4.4(a). The red spectrum in the same figure corresponds to the p-γ gated events. For example, the total counts are reduced by $\approx$ 99% (from 1e6 to 8000 counts), for the 1.4 MeV peak which originates from ^{138}La. The p-γ spectrum is hardly visible due to the large count difference. The background is not yet subtracted from any of these spectra in Fig. 4.4(a).

The p-γ gated spectrum is now shown in blue in Fig. 4.4(b). The background spectrum obtained by gating on the background channels of Fig. 4.3(a) is normalised and subtracted to produce the background subtracted p-γ spectrum shown in red in Fig. 4.4(b). After applying all these gates on the spectra most of the unwanted and/or electronic noise signals, considered as "bad" events, are eliminated.

4.2 Calibration

4.2.1 γ-ray energy calibration

The γ-ray calibration was performed using ^{14}C from the ^{13}C(d,p)^{14}C reaction, ^{66}Ga from the ^{nat}Zn(p, γ)^{xx}Ga reaction and a certified ^{152}Eu source. The γ-ray energies used for the calibration is shown in Tab. 4.2. It should be noted that the internal radiation of the LaBr$_3$(Ce) interferes with many of the γ-ray energies and the collected background run must be normalised and subtracted before it can be used for energy calibration. The LaBr$_3$(Ce) internal radiation will be discussed in Sec. 4.3.

The calibration of the HPGe detectors obtained from the ^{66}Ga data up to 4.8 MeV can be extrapolated up to 7.01 MeV, and the energies will still be accurate due to the energy linearity. However, in case of LaBr$_3$(Ce) detectors, using only the ^{66}Ga calibration data results in the calibration being inaccurate by $\sim$100 keV at 7.01 MeV. The calibration can be improved by including the ^{13}C(d,p)^{14}C reaction data which have γ-ray energies up to 7.01 MeV. The calibration from the ^{13}C(d,p) reaction presented some difficulties for the LaBr$_3$(Ce) since the spectra needed to be Doppler corrected. Applying the calibration on a peak before the Doppler correction was performed resulted in over-correction. For example, for the 7.01 MeV peak in channel 8953 before any calibration:

- Channel 8953 $\rightarrow$ calibration $\rightarrow$ 7.01 MeV $\rightarrow$ Doppler correction $\rightarrow$ wrong energy.

Instead the following order is used to ensure correct outcomes:

- Channel 8953 $\rightarrow$ Doppler correction $\rightarrow$ Channel 8816 $\rightarrow$ calibration $\rightarrow$ 7.01 MeV (right energy).

The β velocity value of the projectile was calculated using the reaction kinematics for each level and angle. The channels are Doppler corrected first then calibrated. The Doppler correction procedure is explained in detail in Sec. 4.7. This method can be applied because the percentage shift of the spectrum remains the same regardless if it is applied to channels or to the calibrated spectra. For example:

- Channel 7521 $\rightarrow$ Doppler correction $\rightarrow$ channel 7366 (2.1% shift)

- 4538 keV $\rightarrow$ Doppler correction $\rightarrow$ 4445 keV (2.1% shift).

The linearity of the detectors can be determined as a function of the channels versus the γ-ray energy. Figure 4.5 shows the linearity of the clover crystal (green), the Oslo LaBr$_3$(Ce) (red) and the Army LaBr$_3$(Ce) (blue). Only the Army LaBr$_3$(Ce) detectors

Table 4.2: The γ-ray energies and intensities for each source used for calibration purposes. A source was used for ^{152}Eu, while ^{66}Ga and ^{14}C was populated through a reaction, see text for more details.

Source	Energy (keV)	Intensity (%)
^{152}Eu [66]		
	121.7817 (3)	28.37 (13)
	244.6975 (8)	7.53 (4)
	344.2785 (13)	26.57 (11)
	411.1165 (13)	2.238 (10)
	443.96 (3)	3.125 (14)
	778.9045 (24)	12.97 (6)
	867.378 (4)	4.214 (25)
	964.079 (18)	14.63 (6)
	1112.074 (4)	13.56 (6)
	1212.948 (11)	1.412 (8)
	1299.140 (9)	1.626 (11)
	1408.011 (4)	20.85 (9)
^{66}Ga [67]		
	833.5324 (21)	6.03 (23)
	1039.220 (3)	37.9 (12)
	1333.113 (5)	1.23 (5)
	1918.329 (5)	2.14 (8)
	2189.616 (6)	5.71 (21)
	2422.523 (7)	1.96 (7)
	2751.835 (5)	23.2 (11)
	3228.800 (6)	1.48 (12)
	3380.851 (6)	1.40 (12)
	3791.009 (6)	1.02 (11)
	4085.853 (9)	1.14 (19)
	4295.224 (10)	3.5 (7)
	4806.005 (10)	1.5 (4)
^{14}C [68]		
	6092.4 (2)	1
	7012 (4)	0.99 (7)
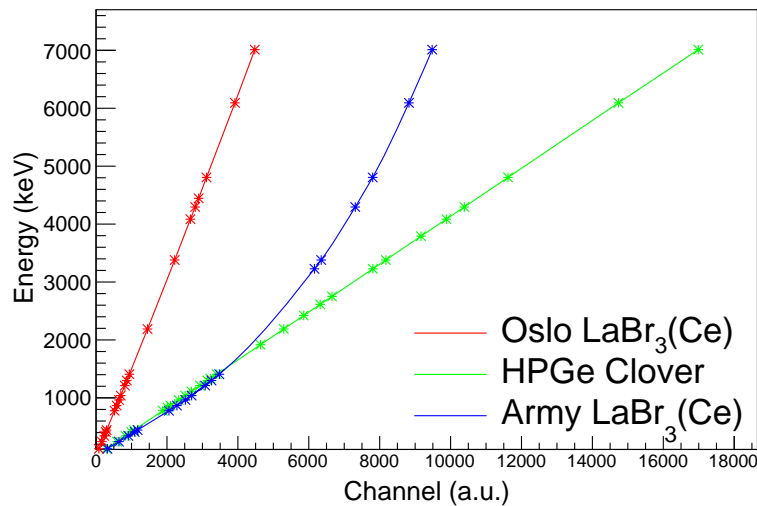
Figure 4.5: The linearity of the HPGe clover crystal (green) is compared to the Oslo (red) and Army (blue) LaBr$_3$(Ce).

appear to have a non-linear energy characteristics, hence a fourth order polynomial function was needed to perform a proper energy calibration of these crystals. Even though the Oslo LaBr$_3$(Ce) appears linear a second or third order polynomial fit was still needed for a good calibration between 0.121-7.01 MeV. For the HPGe detectors a linear calibration was sufficient.

A spectrum calibrated using the transitions observed in ^{66}Ga is shown in Fig. 4.6. The energies which could be clearly identified are presented and the ^{66}Ga decay will be discussed in more detail in Chapter 5. The figure presents the single crystal HPGe in green, the Oslo LaBr$_3$(Ce) in red and Army LaBr$_3$(Ce) in blue. The centroids shown are slightly shifted and differ by a few keV (less than 10 for LaBr$_3$(Ce) and less than 5 for HPGe).

The Army LaBr$_3$(Ce) detectors were arduous to use. During the experiment one of the detectors became unusable. Fig. 4.7 shows the uncalibrated ^{14}C spectra from before and after the experiment for this crystal. This could be caused by a faulty voltage divider or a HV power supply. The other Army LaBr$_3$(Ce) detector was operational, however the resolution was worse compared to other detectors used in the setup – a FWHM of 70 keV at 4.8 MeV in comparison with 43 keV at the same energy for an Oslo LaBr$_3$(Ce) crystal. Taking this into account it was decided to leave the Army LaBr$_3$(Ce) out of the final data analysis.

As discussed in Chapter 3 a peak drift may occur, especially during long experiments. Figure 4.8 shows a γ-ray spectrum for the ^{13}C(d,p)^{14}C data for one LaBr$_3$(Ce) crystal and one HPGe Clover detector. The peak centroids for the Oslo LaBr$_3$(Ce) and HPGe
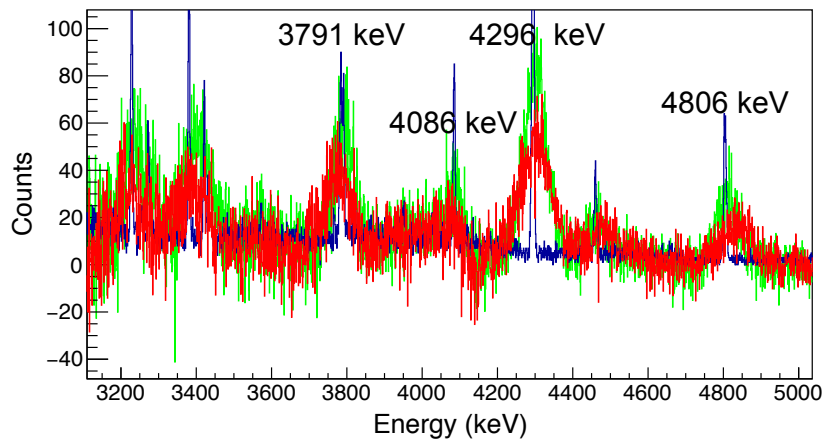
Figure 4.6: Calibrated ^{66}Ga spectra between 3 and 5 MeV for Oslo LaBr$_3$(Ce) spectra (green), single crystal Ge spectra (blue) and the Army LaBr$_3$(Ce) (red).
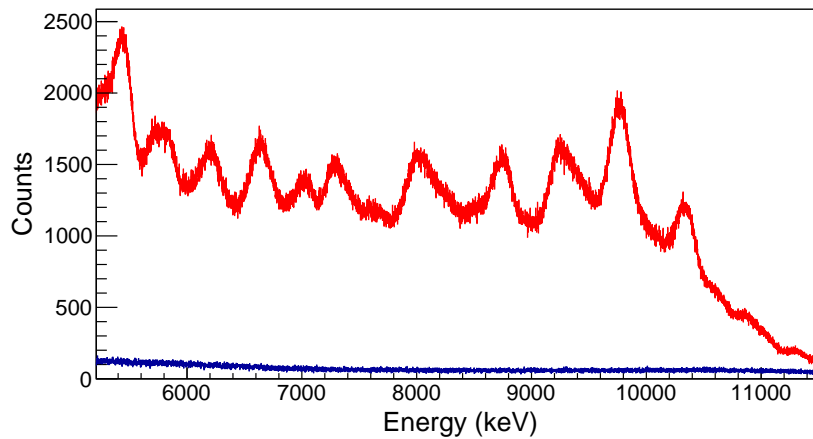
Figure 4.7: An Army LaBr$_3$(Ce) ^{13}C(d,p)^{14}C uncalibrated single spectra from before (red) and after (blue) the experiment. During the experiment this Army LaBr$_3$(Ce) detector stopped working.

peaks did not drift. The ^{13}C(d,p)^{14}C reaction will be discussed in detail in Chapter 5.

4.2.2 Particle energy calibration

The particle spectra are calibrated using ^{14}C beams of different energies (30, 38, 45 and 52.6 MeV) delivered on the ^{194}Pt target. A calibrated spectrum of one ring collected in the ^{194}Pt(^{14}C,^{14}C')^{194}Pt measurement is presented in Fig. 4.9. The spectrum in blue represents the single spectrum and the p-γ gated spectrum is shown in red. The peak at 24-35 MeV corresponds to the energy range where the Coulomb excitation particles are found. The energy calibration is performed only in the region of interest, 30 - 52.6 MeV and cannot be fully trusted below 10 MeV due to a calibration offset of 5 MeV. The region

(a) HPGe Clover
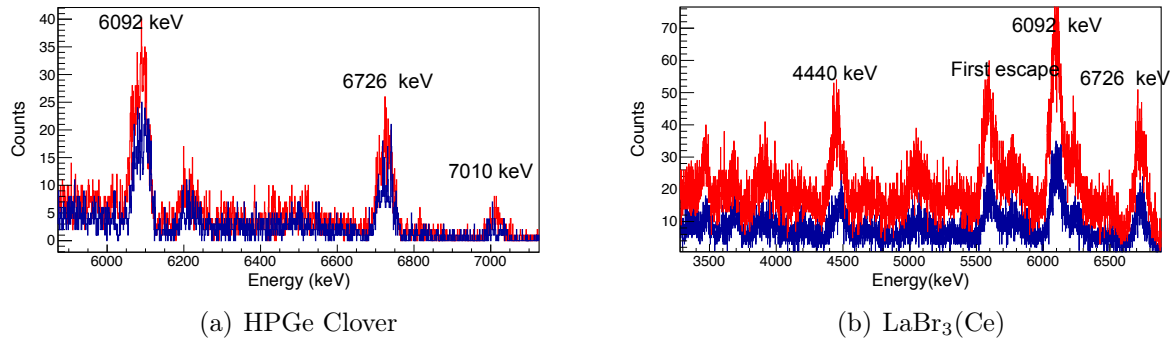
(b) LaBr$_3$(Ce)

Figure 4.8: γ-ray spectra of the ^{13}C(d,p)^{14}C reaction for one LaBr$_3$(Ce) and one HPGe Clover from the first (blue) and last (red) day of the experiment.
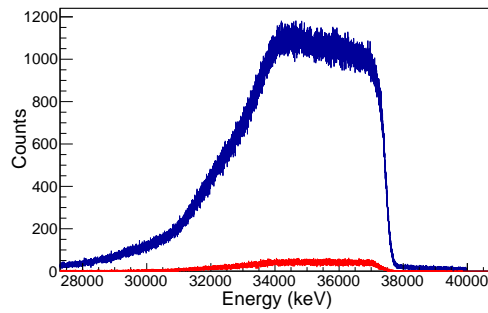
Figure 4.9: Single particle spectrum of one ring (blue) and the p-γ gated spectrum of one ring (red).
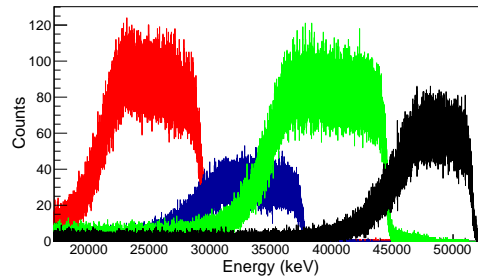
Figure 4.10: The scattered ^{14}C beam of 30 MeV (red), 38 MeV (blue), 45 MeV (green) and 52.6 MeV (black) energies used for calibration.

of interest is above 30 MeV so the nonlinearity in a low energy range of the spectrum is not a problem. The different beam energies collected by one ring are shown in Fig. 4.10.

4.3 Internal radiation of LaBr$_3$(Ce) detectors

Natural Lanthanum contains 0.09% of radioactive ^{138}La [69]. The ^{138}La decays to ^{138}Ba by electron-capture with a probability of 66.4% and emits a 1436 keV γ-ray. ^{138}La can
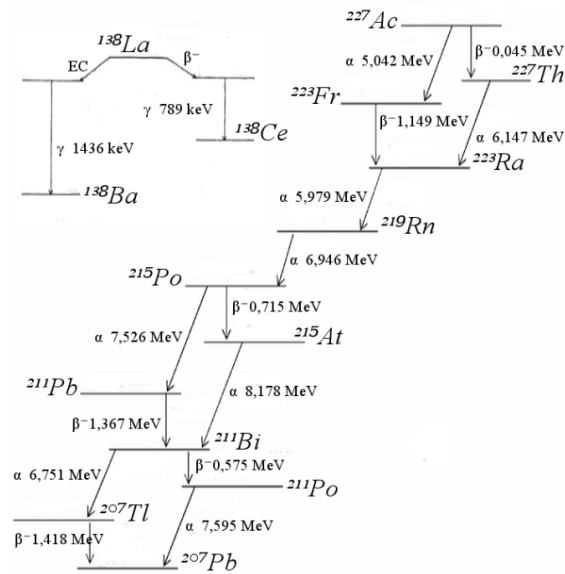
Figure 4.11: The decay schemes of the internal radiation ^{138}La and ^{227}Ac taken from [70].

also decay to ^{138}Ce by β-emission with a probability of 33.6% emitting a 789 keV γ-ray and a β with endpoint energy 255 keV. The β^- decay produces the continuum spectrum around 789 keV. ^{227}Ac contaminants can also be found in the crystal and these contaminants form an α-decay chain: ^{227}Ac will decay to ^{227}Th or ^{223}Fr. From ^{227}Th it decays to ^{223}Ra, ^{219}Rn and then ^{215}Po. ^{215}Po will decay to ^{215}At or ^{211}Pb. ^{215}At and ^{211}Pb decay further to ^{211}Bi and then to ^{207}Tl or ^{211}Po. The final product is ^{207}Pb. The decay chain is shown in Fig. 4.11 taken from Ref. [70]. The energies of the α-particles are all larger than 5 MeV, however they are responsible for the multiple peaks between 1.8 and 2.6 MeV. The interaction of α-particles with the LaBr$_3$(Ce) detector produce less light emission resulting in lower pulse heights which are ~ 0.35 compared to signal heights produced by γ-rays [71, 72]. The internal radiation is presented in Fig. 4.12. Due to the large contribution of the internal radiation any measurement of peak intensity has to be performed carefully.

A background run of 24 hours was taken and subtracted from the source data before any area was calculated, however this does not remove all the background and fitting peaks and subtracting background is not trivial. Figure 4.13 shows the ^{152}Eu source data (blue line) and the background subtracted data (red line). To estimate the background beneath each peak, background areas (where no γ-ray is or should be observed), was identified and fitted with a fifth degree polynomial as shown in Fig. 4.14(a). Using this fit the background remaining beneath each peak is then subtracted. As an example the background remaining beneath the 344 keV peak is shown as the filled black area in Fig. 4.14(b).
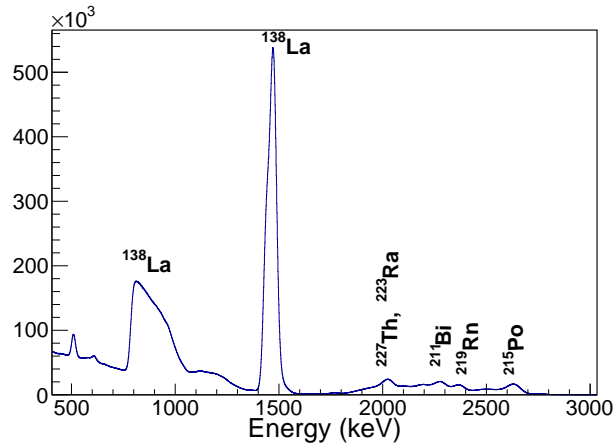
Figure 4.12: A ^{152}Eu spectra measured by a LaBr$_3$(Ce) without background subtraction. The internal radiation of the LaBr$_3$(Ce) can be clearly seen.
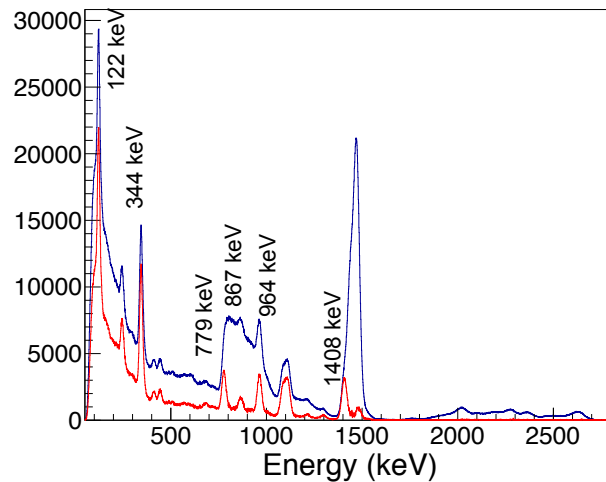
Figure 4.13: The blue spectrum is the source data from ^{152}Eu. The red spectrum is the background subtracted source data.

4.4   Add-back

If more than one γ-ray detector detects a γ-ray in the same event, that event is considered "bad", because it is impossible to say which γ-ray(s) comes from the reaction with the ^{14}C beam and which one(s) is a random detection related to the background. These events are rejected when associated with the LaBr$_3$(Ce) detector, but not with the HPGe clovers.

Each clover detector consists of four crystals and a γ-ray can Compton scatter from one crystal into a neighbouring one. If this happens within 150 ns, the energies are added up and it is considered as one good event. This method is called add-back. If more than two crystals registered a hit such an event is also considered "bad". Add-back drastically increases the efficiency of the clover detectors. Figure 4.15 shows a γ-ray spectrum with

(a) Background fit
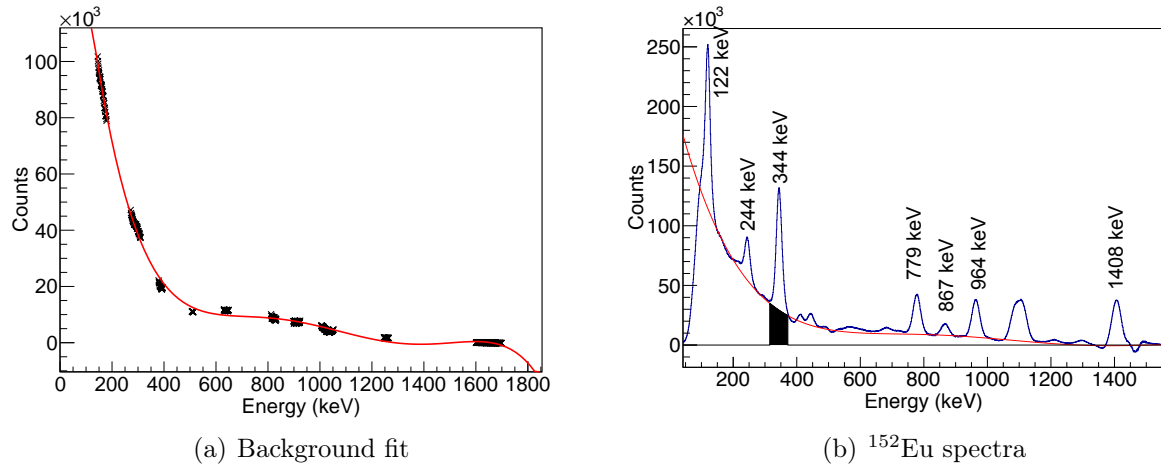
(b) ^{152}Eu spectra

Figure 4.14: The identified background regions (black stars) are fitted with a 5th degree polynomial function (red line) (a) to obtain a background fit that can be used to subtract background. Such a fit is applied to the ^{152}Eu spectra (blue) for all LaBr$_3$(Ce) detectors. The fitted background of this spectrum is shown as the red line. The background remaining in the 344 keV peak that will be subtracted is the filled black area.
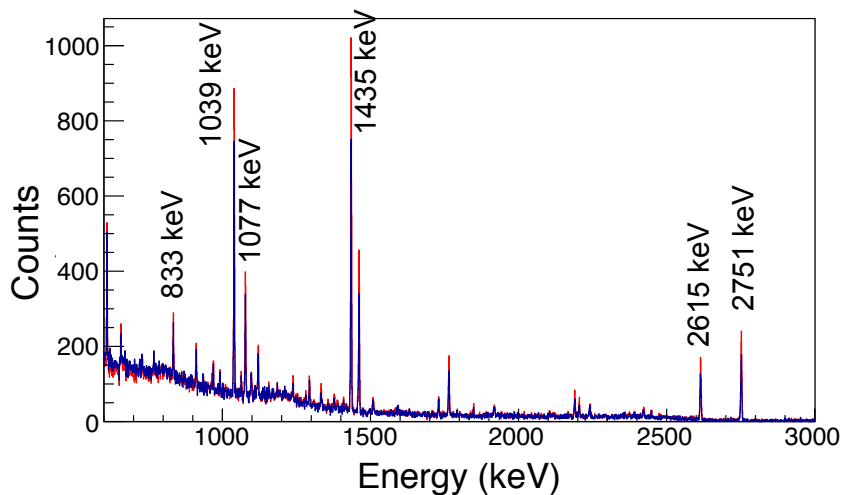
Figure 4.15: A ^{66}Ga γ-ray spectrum without (blue) and with (red) add-back

(red) and without (blue) add-back. For example at 1.4 MeV the counts are increased by 18%.

In the add-back event the time and angle information are used from the first γ-ray registered, because this is the γ-ray that interacted with the detector crystal. The second γ-ray scattered into a neighbouring crystal and its angle and time information is ignored.
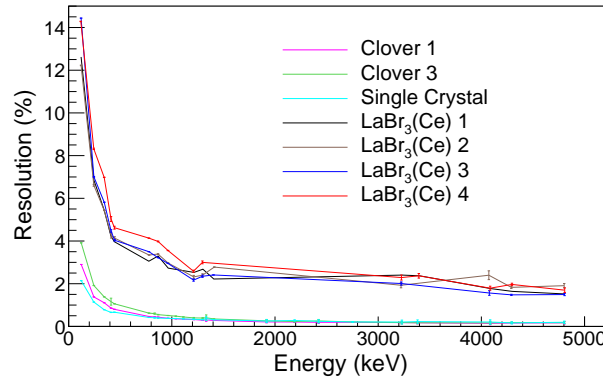
Figure 4.16: Resolution as measured from the ^{152}Eu and ^{66}Ga sources for all detectors.

4.5 Resolution and efficiency

Using the calibrated ^{152}Eu and ^{66}Ga spectra as well as the ^{13}C(d,p)^{14}C [1] spectrum the resolutions and the efficiencies of all detectors can be determined. Figure 4.16 shows the resolutions of the various detectors used. The HPGe detectors have an overall better resolution than the LaBr$_3$(Ce) detectors. The good energy resolution of a HPGe detector plays an important role when two γ-ray transitions are separated in energy by tens of keV. A LaBr$_3$(Ce) detector has much worse resolution and resolving close laying γ-rays is not trivial. The resolution of a detector can be deduced in the following way:

$$\frac{FWHM}{H_0}, \tag{4.1}$$

where FWHM is the full width at half maximum, usually given by 2.35 multiplied by the standard deviation of the gaussian distribution. H_0 is the mean γ-ray energy corresponding to the full-energy peak.

All radiation must undergo interaction over some distance. In some cases the radiation will have multiple interactions and each interaction will be separated by some distance. Some events may not be fully detected if some of the radiation escapes the detector medium. A detector's absolute efficiency is an indication of how many γ-rays are collected out of all the γ-rays emitted. An absolute efficiency takes into account the distance between the source and the detector, the activity of the source, the counting time and the intensity of the reference γ-rays. Intrinsic efficiency is an indication of the amount of γ-rays collected out of all the γ-rays hitting the detector. Intrinsic efficiency takes into account geometry, detector material, physical thickness and the energy of the radi-

---

[1]The ^{13}C(d,p)^{14}C reaction results are discussed in detail in Ch. 5.
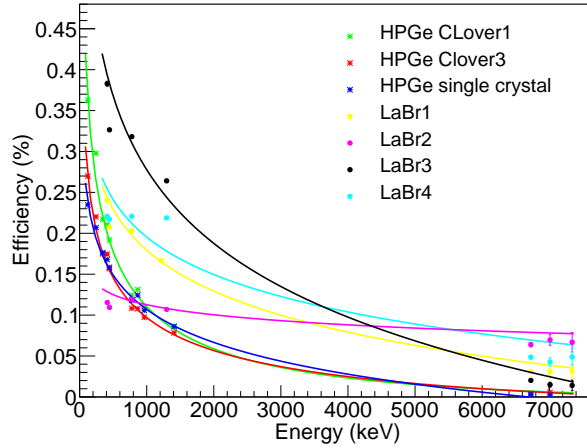
Figure 4.17: Fitted absolute efficiency as measured from the calibrated ^{152}Eu source and ^{13}C(d,p)^{14}C reaction for individual detectors. The LaBr$_3$(Ce) 2 (magenta line) was positioned behind a plastic box filled with cables so the γ-rays were attenuated.

ation. For the purpose of this work only the absolute efficiency with add-back applied is considered. The absolute efficiency can be calculated using the following expression:

$$\epsilon_{abs} = \frac{\text{Counts in full energy peak}}{\text{Activity} \times \text{counting time} \times \text{intensity}}. \tag{4.2}$$

This approach cannot be used with the ^{13}C(d,p) reaction data because the activity is unknown. Instead, the efficiency is calculated from the following:

$$\epsilon_{abs} = \frac{\text{p-}\gamma \text{ counts}}{\text{single particle counts}}. \tag{4.3}$$

The absolute efficiency of the HPGe with add-back and LaBr$_3$(Ce) detectors are shown in Fig. 4.17. The robustness of the LaBr$_3$(Ce) can now be seen in the measured efficiency. The LaBr$_3$(Ce) 2 (magenta line) was positioned behind a plastic box filled with cables so the γ-rays were attenuated, which is negligible at higher energies. None of the LaBr$_3$(Ce) detectors were at the same distance from the target so the efficiency of each one of them is slightly different. Due to the internal radiation of the LaBr$_3$(Ce) material many of the γ-ray spectra are contaminated, which makes the procedure of obtaining an accurate efficiency strenuous. Only those peaks with no contamination were used in the efficiency determination so there are less data points than it would be for other types of detectors. The absolute efficiency is fitted with:

$$\log(\epsilon(E_\gamma)) = \sum_{i=0}^{n} p_i \times (\log(E_\gamma))^i, \tag{4.4}$$

where E is the energy, ϵ is the efficiency and p is the fit parameters. For the combined LaBr$_3$(Ce) the best χ^2 is obtained with $n = 2$ and the fitted equation is given by $\log(\epsilon(E)) = -2.199(\pm 0.54) + 1.05(\pm 0.15)\log(E) - 0.089(\pm 0.01)\log(E)^2$.
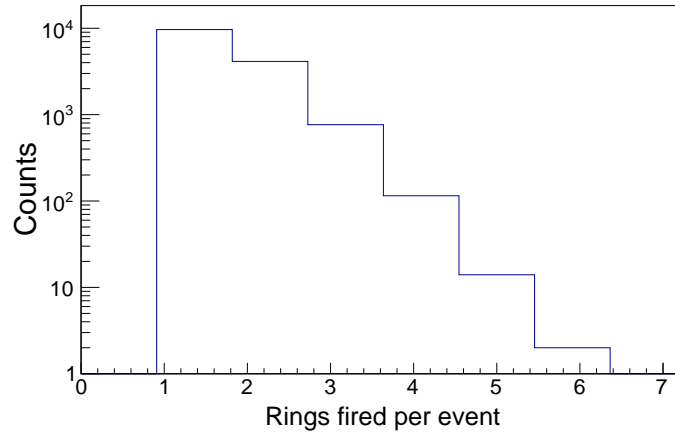
Figure 4.18: The number of rings fired simultaneously in one event for a subset of data. For example, one ring fired 10^4 times, two rings fired 5×10^3 times etc.

4.6 "Good" and "bad" events

The procedure to determine "good" and "bad" events will be explained starting from the particle detector. The S3 silicon detector has 24 rings and 32 sectors that were conjuncted into 16 sectors due to limited available electronic channels. A "good" particle event is validated when a particle hits the silicon detector, the energy is deposited in one sector and one ring in a 100 ns time window (channels from 195 to 215 presented in Fig. 4.3(b)). It can happen that two particles hit the silicon detector within the same time gate and those events are rejected. Therefore only those events where only one particle hit is registered is accepted and all other (multi-hit) events are ignored.

The exception is one particle colliding exactly between two rings or two sectors. In such events the energy is shared between the two adjacent rings or sectors and up to half of the energy can be distributed between them [73]. If this happens, the time between the two hits is small (a few ns). Therefore if a hit is registered in adjacent rings or sectors, the measured energy will be added and the event will be considered as only one particle hit. Similarly to the add-back process, the angle and position of the particle that was recorded first in time is used. This effect contributes to about ~ 1 out of ~ 50 events in the final gated spectrum for a ring, hence such statistics should not be neglected and is taken into consideration in the final analysis. The number of rings fired per event for an ungated subset of the data is shown in Fig. 4.18. The effect of the energy sharing is shown for a subset of gated particle spectra data in Fig. 4.19. The red line shows all the events that are included in the energy sharing. Note that there is an energy threshold set on the silicon detector at 25 MeV. The red data below 25 MeV are therefore only the energy shared events. The blue line in Fig. 4.19 represents the data with energy sharing.
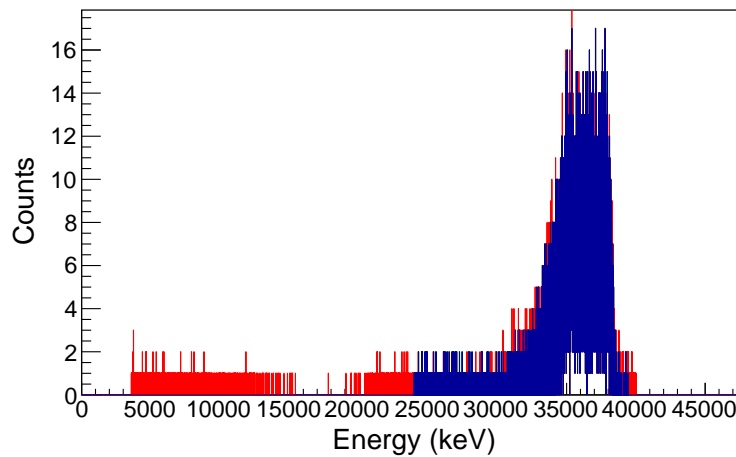
Figure 4.19: Gated data with (red) and without (blue) energy sharing for a subset of data.

When a charge is deposited into a ring/sector a mirror charge (a charge with similar strength but an opposite sign) can be induced in a neighbouring ring/sector. These mirror charges can also be detected in the silicon detector. This effect happens when the particle hits a sector (or ring) and deposits some energy in its volume. The adjacent sectors (or rings) can then receive a mirror charge, a low energy "hit" induced due to polarisation effects. Some energy sharing events may be confused with the mirror charge effects, however this does not influence the obtained spectra since the energies are typically small and eliminated by the energy cut-offs.

The p-γ coincidence, ring-sector particle energy matrix has a significant contribution of background events. The amount of energy deposited in both a ring and sector should be the same within the resolution and the "good" events all lie on the diagonal of this matrix. To reduce all the random and background events a gate is applied around the diagonal line with a width of 2500 keV. Figure 4.20 shows the ring-sector matrix before (a) and after (b) the diagonal gate is introduced. The events not on the diagonal (the "bad" particle events) were not investigated further.

4.7 Doppler correction

After applying the energy calibrations and time gates the "good" or "bad" events are selected and the Doppler correction can be implemented. Due to the γ-ray emission in flight from the excited projectile and recoiling nuclei, a Doppler shift of the observed γ-rays occur. In the Coulomb excitation reaction, the projectile is backscattered and therefore when it decays it moves towards the Oslo LaBr$_3$(Ce) detectors placed in the

(a) Ungated

(b) Gated
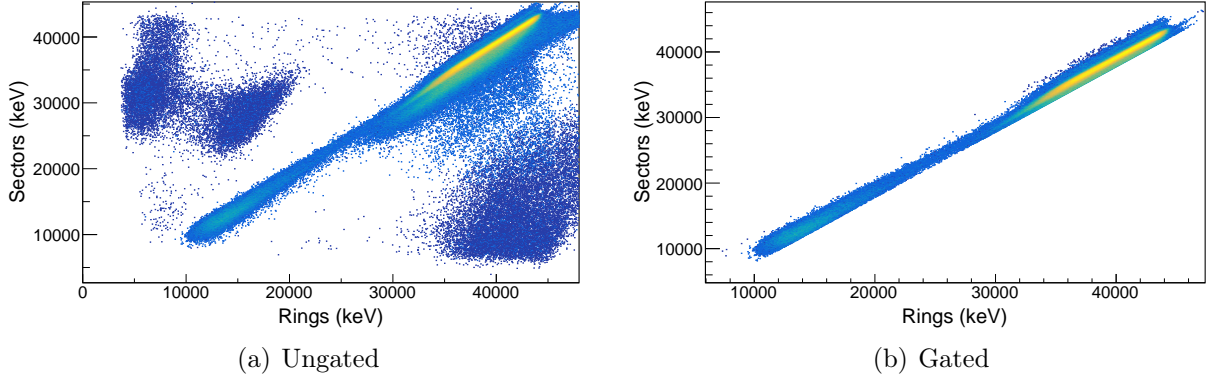
Figure 4.20: Rings-sectors energy matrix for a subset of the data is shown in (a). A diagonal cut is applied to reduce background events for (b).

backwards angles and away from the Army LaBr$_3$(Ce) placed in the forward angles. When a γ-ray is emitted while the particle moves away from the detector (towards the detector) it is shifted towards lower energies (higher energies), respectively. Using Eq. 2.38 the Doppler corrected γ-ray energy is given by:

$$E_{initial} = \frac{E_{ds}(1 - \beta \cos(\alpha))}{\sqrt{1 - \beta^2}}, \tag{4.5}$$

where E_{ds} is the energy of the γ-ray which is measured in the LaBr$_3$(Ce) or HPGe detectors, α is the angle between the direction of the ^{14}C and emitted γ-ray and $\beta = \frac{v}{c}$ is the fraction of the speed of light the charged particle is moving at. β for ^{14}C can be calculated from:

$$\sqrt{\frac{2E_{14C}}{M_{14C}}} = \sqrt{\frac{E_{14C} \times 2}{14 \times 931.5}} = \beta. \tag{4.6}$$

E_{14C} is the energy deposited into the S3 detector and M_{14C} is the mass of the charged particle. The ^{14}C particles have some energy distribution and each event will have a different β velocity. The β value is calculated for each event individually. The event-by-event calculated β distribution of ^{14}C is shown in Fig. 4.21.

To calculate the angle α it is useful to represent the position of the γ-ray and particle in spherical coordinates:

$$\hat{r}_\gamma = \sin\theta_\gamma \cos\phi_\gamma \hat{x} + \sin\theta_\gamma \sin\phi_\gamma \hat{y} + \cos\theta_\gamma \hat{z}$$
$$\hat{r}_{si} = \sin\theta_{si} \cos\phi_{si} \hat{x} + \sin\theta_{si} \sin\phi_{si} \hat{y} + \cos\theta_{si} \hat{z}. \tag{4.7}$$

The angle between the γ-ray and particle is given by the dot product:
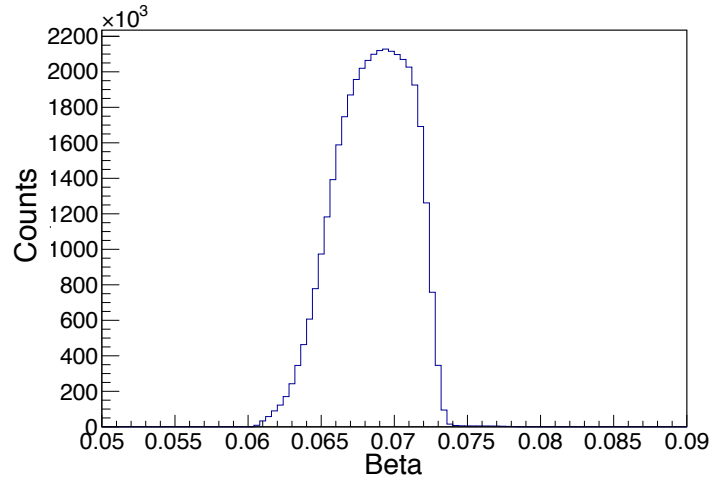
Figure 4.21: The distribution of β for ^{14}C that is used for the event-by-event Doppler correction.

$$
\begin{aligned}
\hat{r}_{si} \cdot \hat{r}_{\gamma} = \cos\alpha &= \sin\theta_{si}\cos\phi_{si}\sin\theta_{\gamma}\cos\phi_{\gamma} + \sin\theta_{si}\sin\phi_{si}\sin\theta_{\gamma}\sin\phi_{\gamma} + \cos\theta_{si}\cos\theta_{\gamma} \\
&= (\sin\theta_{\gamma}\sin\theta_{si})(\cos\phi_{\gamma}\cos\phi_{si} + \sin\phi_{\gamma}\sin\phi_{si}) + \cos\theta_{si}\cos\theta_{\gamma} \\
&= \sin\theta_{\gamma}\sin\theta_{si}\cos(\phi_{\gamma} - \phi_{si}) + \cos\theta_{si}\cos\theta_{\gamma}.
\end{aligned}
$$

$$(4.8)$$

A 7.01 MeV γ-ray travelling at 7% the speed of light will be spread over hundreds of keV due to the Doppler shift, see Ch. 6 for more detail. This makes the testing of the Doppler correction settings non-trivial at 7.01 MeV. The Doppler correction settings can instead be tested by looking at the shift of ^{194}Pt γ-ray lines. Due to the recoil of the ^{194}Pt nucleus after a collision, it should have a β velocity of $\sim 1\%$ of the speed of light. If the forward-moving ^{194}Pt is corrected for the backward moving ^{14}C, the peaks should be shifted in the "wrong" way. For backward LaBr$_3$(Ce) detectors the ^{194}Pt peaks simply shift ≈ 15 keV lower as shown in Fig. 4.22(a). For the clover detectors at 90° the peak is split in two – two crystals are shifted toward higher energies and the other two are shifted towards lower energies, as shown in Fig. 4.22(b) where the blue spectrum is not Doppler corrected for ^{14}C velocity and the red spectrum is. The Doppler shift and corresponding Doppler correction is simulated for a LaBr$_3$(Ce) detector in Ch. 6.
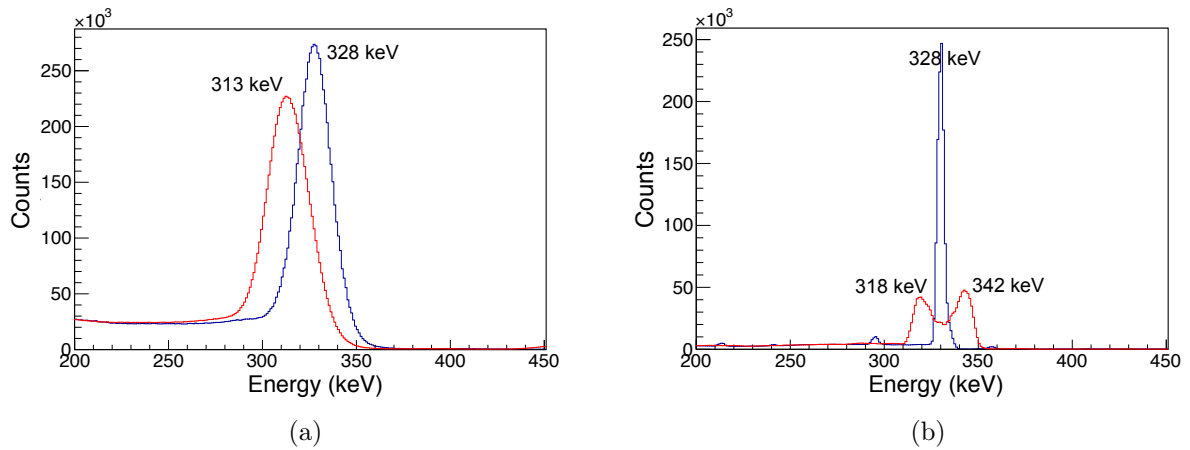
Figure 4.22: Part of the ^{194}Pt spectra without (blue) and with (red) Doppler correction for a LaBr$_3$(Ce) at $\theta = 135°$ (a) and HPGe clover with add-back (b) at $\theta = 90°$. The ^{194}Pt moving with $\beta = 1\%$ is corrected for ^{14}C which moves at $\beta = 7\%$. This is done to test the Doppler correction, see text for more detail.

Chapter 5

Results

Some of the results from the ^{xx}Ga and ^{13}C experiments were briefly described in the previous sections as this data were used for calibration purposes. The results from the various experiments performed are presented and discussed in detail in this chapter.

5.1 $\quad ^{nat}$Zn(p,γ)^{xx}Ga

In the ^{nat}Zn(p,γ)^{xx}Ga activation experiment, a 8.5 MeV energy proton beam was delivered on a 0.1mm thick ^{nat}Zn target. This measurement was performed before and after the Coulomb excitation experiment of ^{14}C to provide the necessary calibration data up to $E_\gamma = 4.8$ MeV, which could also be used to track and correct the γ-ray peak position drift.

Due to the presence of the LaBr$_3$(Ce)'s internal activity, the HPGe clovers are used to show the obtained Ga spectra. The populated states in the ^{66}Ga isotope decay with γ-ray energies up to 4.8 MeV. Therefore this nucleus is relevant for this work. In particular, the 4806 keV (1.86%), 4.461(0.84%), 4.295 MeV (3.82%) and 4085 keV (1.27%) γ-ray transitions. The ^{64}Ga isotope also decays with γ-rays up to 4.7 MeV but due to the short half-life of this nucleus (2.62 minutes) the intensities of the transitions of interest are much lower compared to ^{66}Ga. With just 1 hour of target irradiation and a day of data taking, good statistics were obtained, as presented in Fig. 5.1. Some of the peaks originating from different reaction channels and the background lines are highlighted. It should be noted that ^{67,70}Ga are also observed in the reaction but with the low number of counts they are negligible. The main full energy deposition peaks present in the spectrum that could be used for the calibration purposes are shown in Tab. 5.1. Some contamination from neighbouring nuclei is observed and excluded from the calibration, for example the 3791 keV from ^{66}Ga and 3795 keV from ^{64}Ga, however there remains numerous γ-rays that can be identified with confidence as shown in Tab. 5.1.

Table 5.1: The γ-ray energies and corresponding parent nucleus that could be used for energy calibration purposes.

Energy	Nucleus
4806 keV	^{66}Ga
4461 keV	^{66}Ga
4295 keV	^{66}Ga
4085 keV	^{66}Ga
3381 keV	^{66}Ga
3381 keV	^{66}Ga
3228 keV	^{66}Ga
2751 keV	^{66}Ga
2615 keV	^{208}Tl (from the Th background chain)
2189 keV	^{66}Ga
1436 keV	^{138}La (internal radioactivity from LaBr$_3$(Ce) detectors)
1039 keV	^{66}Ga
789 keV	^{138}La (internal radioactivity from LaBr$_3$(Ce) detectors)
511 keV	Annihilation photon

Table 5.2: The percentage of each isotope of Zn that occurs in nature, the reactions when colliding with protons and the half-lives of the Ga isotopes produced are shown [1].

Isotope abundance [1]	Reaction	half-life [1]
^{64}Zn 49.17%	^{64}Zn(p,γ)^{64}Ga	2.627 (12) minutes
^{66}Zn 27.73%	^{66}Zn(p,γ)^{66}Ga	9.49 (3) hours
^{67}Zn 4.04%	^{67}Zn(p,γ)^{67}Ga	3.2617 (5) days
^{68}Zn 18.45%	^{68}Zn(p,γ)^{68}Ga	67.71 (9) minute
^{70}Zn 0.617%	^{70}Zn(p,γ)^{70}Ga	21.14 (3) minutes

A list of isotopes present in the ^{nat}Zn target and the corresponding reactions with protons are listed in Tab. 5.2 [1]. Even though many reaction channels were observed in the present experiment, the resolution of the clover detectors is good enough to distinguish between the different γ-rays for calibration purposes. In case of the LaBr$_3$(Ce) detectors, not all the peaks could be used due to the presence of the internal radiation and the poor energy resolution of the crystals, however the 1039, 2189, 3228, 3381, 4085, 4295 and 4806 keV γ-ray peaks could be used for the calibration.
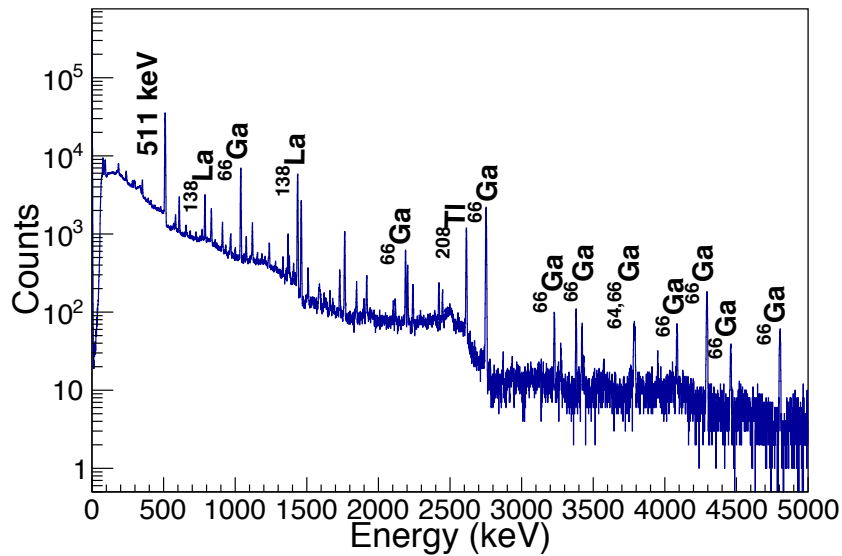
Figure 5.1: Ga spectrum from one clover detector with some γ-rays labelled.

5.2 ^{13}C(d,xx) reactions

5.2.1 ^{13}C(d,p)^{14}C

A 6 MeV deuteron beam impinged on 1 mg/cm^2 ^{13}C target to produce a ^{13}C(d,p) reaction. This measurement was designed to measure the high-energy γ-ray transitions up to the 7 MeV region, which could be used to determine the detector response in a 1n transfer reaction to ^{14}C. In this measurement, a S2 detector was placed at backward angles. The p-γ matrix is presented in Fig. 5.2 (the uncalibrated particle spectrum from one ring on the x-axis and the calibrated γ-ray energies on the y-axis). Different states populated in various nuclei produced in this measurement are also indicated in Fig. 5.3, which is a projection of the matrix onto the x-axis.

By gating on the specific states or on the γ-ray energies in the E_{state}-E_γ matrix the γ-rays decaying from all individual populated states can be identified. The γ-ray energies and states can then be matched with the corresponding emitter. ^{14}C has a state at 6094 keV which decays to the ground state by emitting a single 6092 keV γ-ray. By gating on this state the only γ-ray observed is the 6092 keV transition decaying to the ground state. Even though the particle spectrum is uncalibrated, the γ-ray energies can be used to identify the nucleus and the state they originate from. This is shown – nucleus by nucleus – along with their partial level schemes in Fig. 5.4. Each spectrum is gated on a different state and presents different decays and corresponds to different colours in the partial level scheme from [68] shown in Fig. 5.4(g).
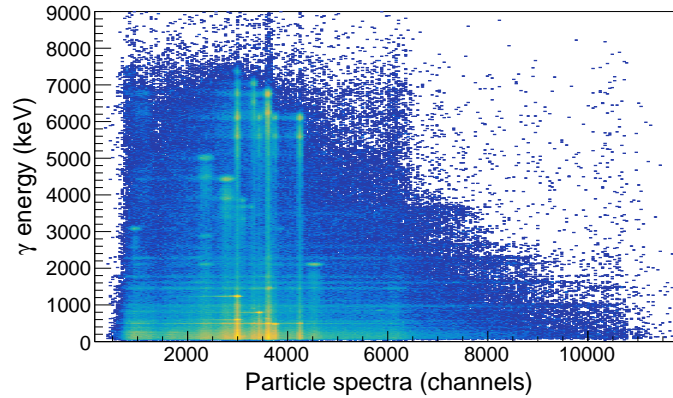
Figure 5.2: The p-γ matrix is shown with the γ-ray energies on the y-axis and the uncalibrated particle spectrum on the x-axis.
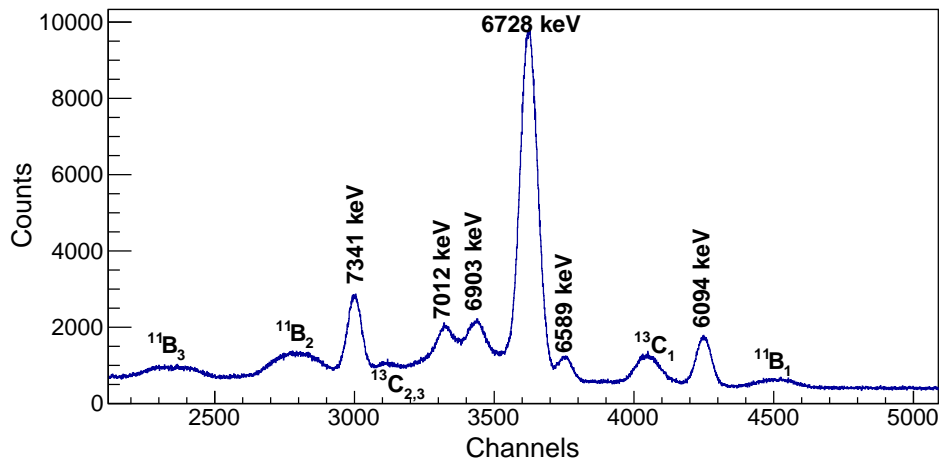
Figure 5.3: The uncalibrated particle spectrum from one ring indicating the different states populated in various nuclei with the ^{13}C(d,p) reaction.

- The 6094 keV (red line) – 1^- state decays only to the ground state, Fig. 5.4(a).

- The 6589 keV (blue) – 0^+ state decays to the 6094 keV state. It cannot decay to the ground state because a γ-ray needs at least one unit of angular momentum, thus a 0^+ decaying to a 0^+ is not possible for a γ-ray, Fig. 5.4(b).

- The 6728 keV (green) – 3^- state decays to the ground state with a 96.4 % intensity and to the 6094 keV state 3.6 %, Fig. 5.4(c).

- The 6903 keV (orange) – 0^- state decays to the 6094 keV state, Fig. 5.4(d).

- The 7012 keV (purple) – 2^+ state decays to the ground state with a 98.6 % branch and to the 6094 keV with 1.4%, Fig. 5.4(e).

- The 7341 keV (black) – 2^- state decays to the ground state with 16.7% intensity, to the 6094 keV with 49% and to the 6728 keV with 34.3%, Fig. 5.4(f).

This reaction was also used to get the response function for the LaBr$_3$(Ce) detector at 7 MeV energy. The 6726 keV full energy γ-ray peak has 6331 counts. Its first escape peak has only 3708 counts (58.5% of the full energy peak) and the double escape peak 2131 counts (33.6% of the full energy peak). Similarly, the 6092 keV γ-ray transition has 9229 counts, the first escape peak 5535 (60%) and the second escape peak 2913 counts 31.5%. This response function can also be used to determine whether any sign of the 7010 keV γ-ray transition in ^{14}C is present in the Coulomb excitation experiment. The first and second escape peak ratios must be the same for the Coulomb excitation experiment. This data also gives confidence that we can unambiguously identify high energy γ-rays.

5.2.2 ^{13}C(d,d')^{13}C

The ^{13}C nucleus is excited in the ^{13}C(d,d')^{13}C reaction. By gating on the peaks labelled as ^{13}C$_{1,2,3}$ in Fig. 5.3 various spectra in Fig. 5.5 are obtained. The first $\frac{1}{2}^+$ state at 3089 keV is observed at channel 4050. It decays to the ground state by emitting one γ-ray transition with an energy of 3089 keV. This decay is shown in red in Fig. 5.5(c) and the γ-ray is indicated in Fig. 5.5(a).

The higher-lying $\frac{3}{2}-$ state at 3684 keV decays with the emission of a 3684 keV γ ray to the ground state with 99.25% intensity. The remaining 0.75% branch corresponds to a cascade of 595 keV γ-ray transition to the 3089 keV state which then decays to the ground state [68]. The resolution of the S2 detector is not good enough to distinguish between the 3684 keV and the 3853 keV states so the gate around channel 3100 selects both. It is also important to note that these states, labelled by ^{13}C$_{2,3}$ are very close to the 7342 keV state, as shown in Fig. 5.3 and some overlap occurs. The $\frac{5}{2}^+$ 3853 state decays to the ground state with 62.5% intensity, while the remaining 36.3% decays to the 3684 keV state and 1.2% to the 3089 keV level [68]. The decays are presented in Fig. 5.5(b). The 595 and 764 keV γ-rays with an intensity $\sim 1\%$ are too weak to be observed by accumulating data over a one-day measurement. The populated levels are marked in blue in the attached level scheme 5.5(c)

5.2.3 ^{13}C(d,α)^{11}B

The ^{11}B isotope is excited through the ^{13}C(d,α)^{11}B reaction. Similarly to ^{13}C, the peaks labelled in the spectra by ^{11}B$_{1,2,3}$ are gated on and the resulting γ-ray spectra shows which state the given transition originated from, see Fig. 5.6. The first $\frac{1}{2}^-$ state at 2125 keV which decays to the ground state is shown in Fig. 5.6(a). This state is marked in
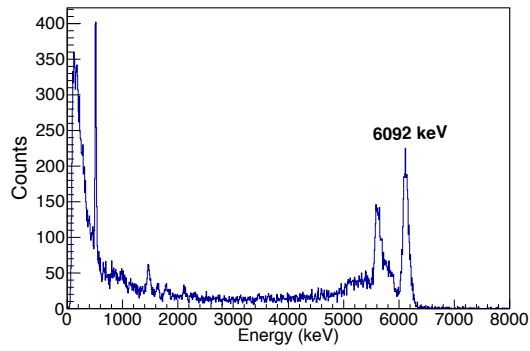
(a) Gating on ^{14}C 1^- in Fig. 5.3
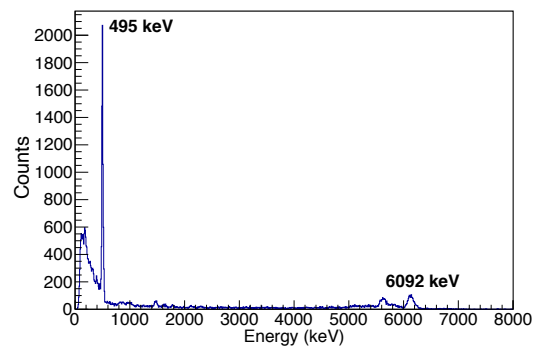
(b) Gating on ^{14}C 0^+ in Fig. 5.3
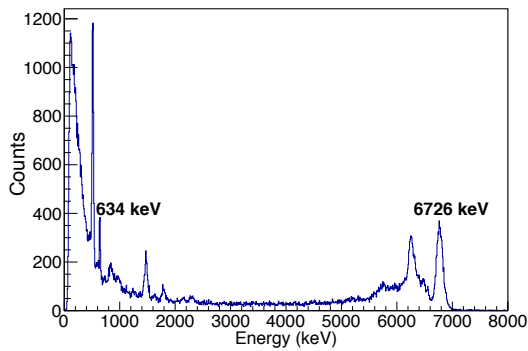
(c) Gating on ^{14}C 3^- in Fig. 5.3
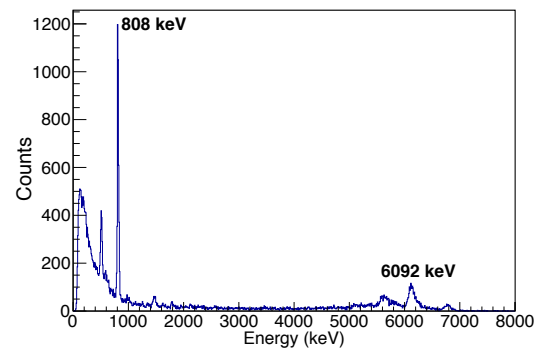
(d) Gating on ^{14}C 0^- in Fig. 5.3
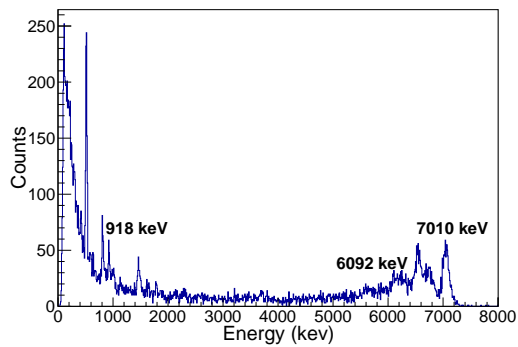
(e) Gating on ^{14}C 2^+ in Fig. 5.3
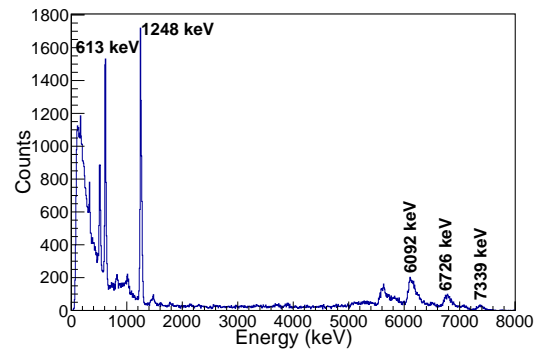
(f) Gating on ^{14}C 2^- in Fig. 5.3
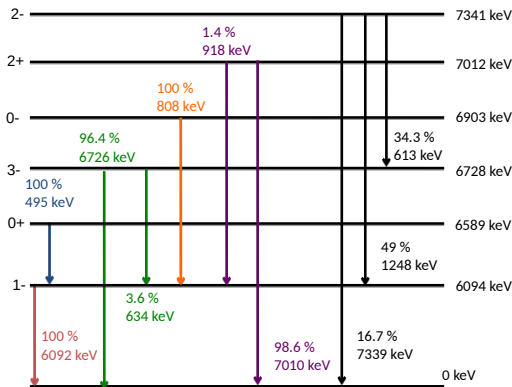
(g) Partial level scheme of ^{14}C

Figure 5.4: The γ-ray spectra from LaBr$_3$(Ce) detectors for the ^{13}C(d,p)^{14}C reaction with different particle gates indicated (panels a-f). The partial level scheme from Ref. [68] is shown in panel (g).

(a) Gating on $^{13}C_1$ in Fig. 5.3

(b) Gating on $^{13}C_{2,3}$ in Fig. 5.3

(c) Partial level scheme of ^{13}C
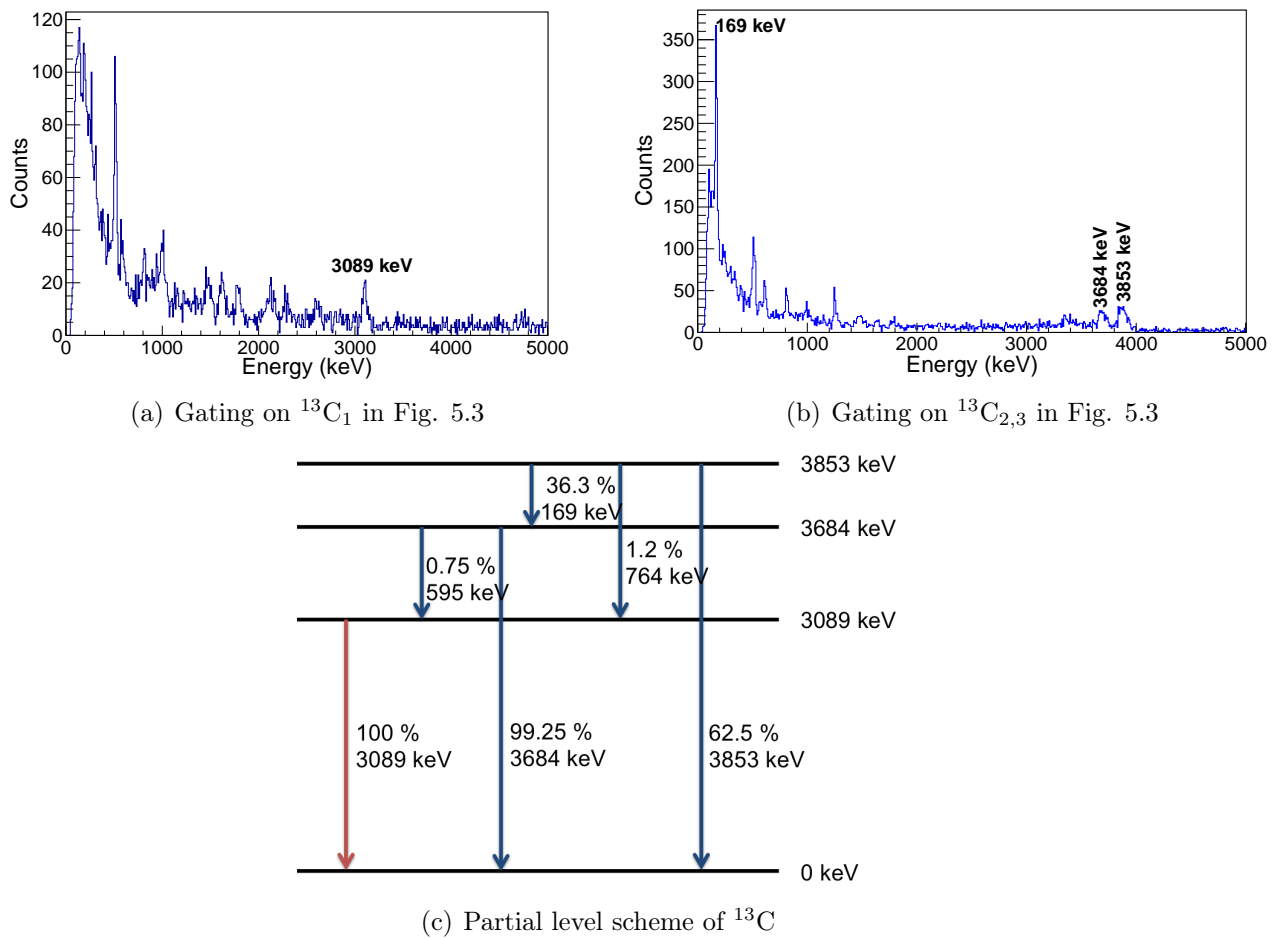
Figure 5.5: The γ-ray spectra from $LaBr_3(Ce)$ detectors for the $^{13}C(d,d')^{13}C$ reaction with different particle gates indicated (a,b). A partial level scheme from Ref. [68] is also shown (c).

red in the included levels scheme 5.6(d).

The $\frac{5}{2}^-$ state at 4444 keV which decays to the ground state is shown in Fig. 5.6(b). It is also marked in blue in the attached level scheme Fig. 5.6(d). Some minor overlap may occur due to the binning of the p-γ matrix, however for the purpose of identifying each transition the effect is negligible. The 5020 keV $\frac{3}{2}^-$ state decays to ground 85.6% and 14.4% to the $\frac{1}{2}^-$ state at 2125 keV [74]. The decay scheme is indicated in green in Fig. 5.6(d) and the corresponding γ-rays are presented in Fig. 5.6(c).

5.3 $^{194}Pt(^{12}C,^{12}C')^{194}Pt$

A ^{12}C beam of $E_{beam} = 48$ MeV energy with a charge state of 5^+ impinged on a $2mg/cm^2$ thick ^{194}Pt target to perform the safe Coulomb excitation reaction, $^{194}Pt(^{12}C,^{12}C')^{194}Pt$. This measurement was performed to provide a test case for the newly developed sorting code. A total beam time of 16 hours was used. A S3 detector was used and placed at

(a) Gating on $^{11}B_1$ in Fig. 5.3

(b) Gating on $^{11}B_2$ in Fig. 5.3

(c) Gating on $^{11}B_3$ in Fig. 5.3

(d) Partial level scheme of ^{11}B
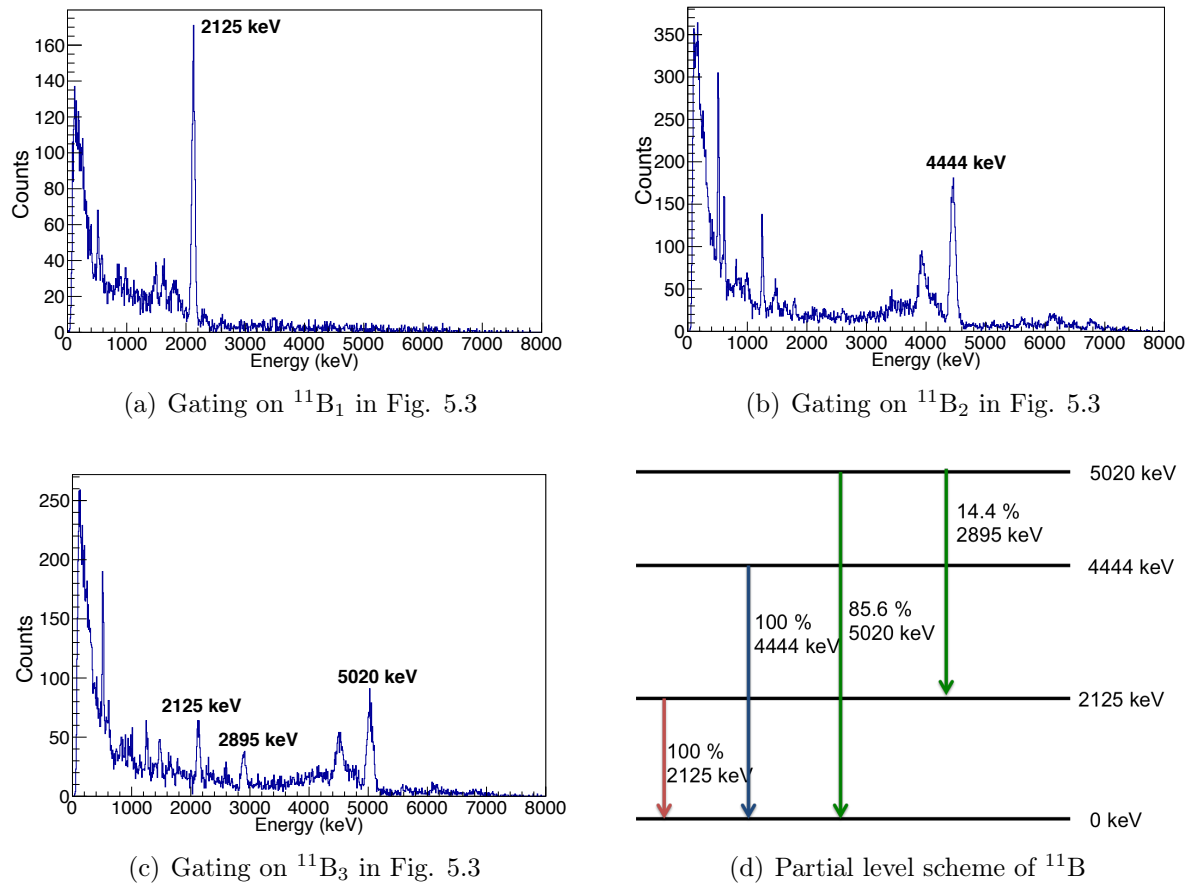
Figure 5.6: The γ-ray spectra from LaBr$_3$(Ce) detectors for the $^{13}C(d,\alpha)^{11}B$ reaction with different particle gates indicated (a,b,c). The partial level obtained from [74] scheme is shown also shown (d).

backward angles. It should be noted that the setup used in this experiment was identical to the main Coulomb excitation experiment performed with the ^{14}C beam.

The first excited 2^+ state in ^{12}C is placed at the energy of 4438 keV. The Doppler corrected, p-γ, background subtracted spectra from the Coulomb excitation of ^{12}C is shown in Fig. 5.7. No indication of ^{12}C is observed in the coincidence measurement, however, the singles spectrum presented in Fig. 5.8 shows that ^{12}C is indeed excited and the 2^+ state was populated, along with the ^{16}O and ^{208}Pb nuclei (presumably from the beam stop which is made of lead). The ^{12}C peak disappears when a p-γ coincidence gate is applied while the ^{194}Pt lines are enhanced. Indicating why no ^{12}C was observed in the p-γ data is not trivial. It seems likely that the backscatter cross section and efficiency of the available detectors were too low to observe any backscattered ^{12}C in such a short run (16 hours).
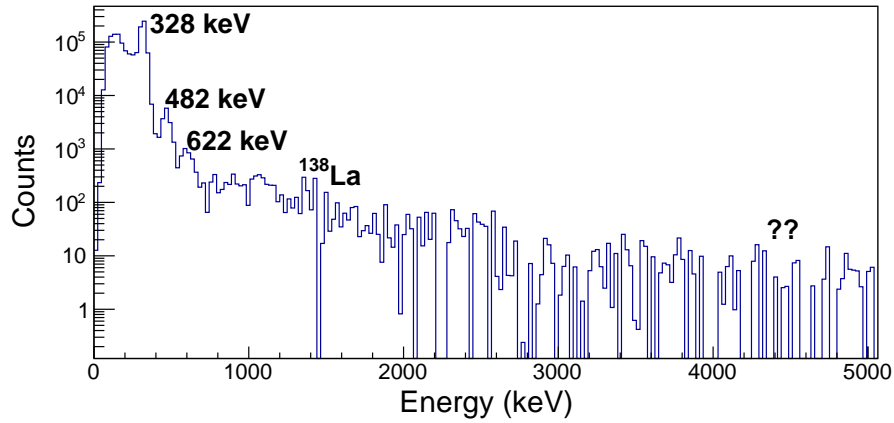
Figure 5.7: Doppler corrected, p-γ coincidence spectra from the $^{194}\text{Pt}(^{12}\text{C},^{12}\text{C'})^{194}\text{Pt'}$ reaction for all LaBr$_3$(Ce) detectors, rebinned to 20 keV/bin.
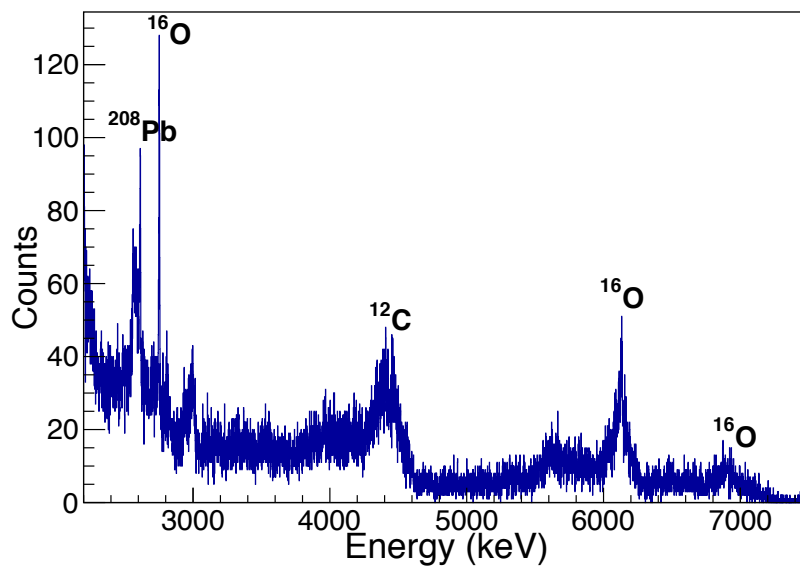
Figure 5.8: Singles γ-ray spectra from a single crystal HPGe detector from the $^{194}\text{Pt}(^{12}\text{C},^{12}\text{C'})^{194}\text{Pt'}$ reaction.

(a)   (b)
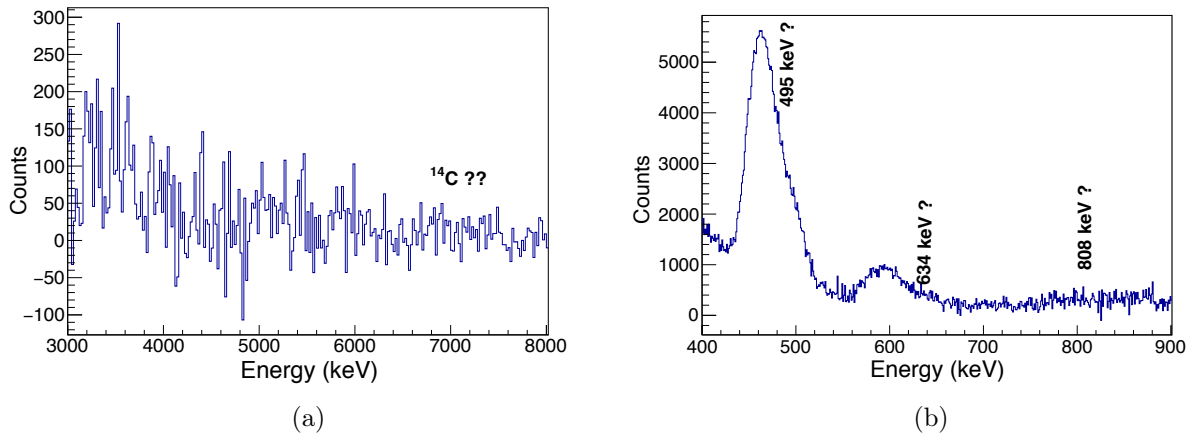
Figure 5.9: Doppler corrected, p-γ coincidence, background subtracted spectra from the Coulomb excitation of ^{14}C from all LaBr$_3$(Ce) detectors rebinned to 40 kev/bin for the high-energy range (a) and 1 keV/bin for the low-energy spectrum (b). The ^{14}C γ-rays are not observed.

5.4 ^{194}Pt(^{14}C,^{14}C')^{194}Pt

5.4.1 ^{14}C

The Doppler corrected, p-γ coincidence, background subtracted spectrum for the combined LaBr$_3$(Ce) detectors is shown in Fig. 5.9(a) for the high-energy range and in Fig. 5.9(b) for the low-energy range. For low statistic regions, such as at 7 MeV compression of the data (by increasing the bin width) is required to reflect the detector resolution. For this reason the spectra is rebinned to 40 keV/bin for Fig. 5.9(a). Various binnings between 1 keV/bin and 200 keV/bin was also tested and no peak could be identified in the 7 MeV region. No excitation of the 2^+ state in ^{14}C is observed in the p-γ coincidence spectra – only the de-excitation of states in ^{194}Pt is clearly visible.

Various γ-ray single transitions can be identified in the spectrum presented in Fig. 5.10. In Fig. 5.10(a) the singles spectrum of all the data collected in one LaBr$_3$(Ce) is shown. The energies of transitions are labelled using the following colour code: ^{14}C in black, ^{16}O in magenta and ^{28}Si in red. The ^{16}O contamination comes from the rust on the beam-stop and the ^{28}Si originates from the S3 Si detector. The $1^- \rightarrow 0_1^+$ transition with a 6092 keV γ-ray and the $3^- \rightarrow 0_1^+$ with 6726 keV γ-ray in ^{14}C are weakly populated. The 2^+ seems to be also populated but only very weakly, however since this is a singles spectrum, the peak at 7 MeV can also come from anywhere. All of these peaks disappear when a p-γ coincidence gate is applied, as previously shown in Fig. 5.9.

In Fig. 5.10(b) the singles γ-ray spectrum for the energies from 1.6 to 3.0 MeV from

one HPGe clover is shown. The γ-rays coming from ^{28}Si are shown in red, ^{16}O in green, ^{208}Pb in black and naturally occurring background ^{208}Tl is shown in magenta. There are many other peaks present in the spectrum, although the purpose of showing this figure is to indicate that the low-energy γ-rays originating from ^{16}O, ^{28}Si and ^{208}Pb are indeed observed in a singles spectrum. The origin of all the measured γ-rays was not studied further.

The low-energy single γ-ray transitions in the range between 400 and 850 keV for one HPGe clover detector is shown in Fig. 5.10(c). The low-energy γ-rays which could originate from ^{14}C are indicated with their energies. Possible ^{14}C transitions are $0_2^+ \rightarrow 1_1^-$ with 495 keV, $3_1^- \rightarrow 1_1^-$ with 634 keV and $0_1^- \rightarrow 1_1^-$ with 808 keV. The 634 keV peak could not be observed due to overlap with another transition. The small peaks of $E_\gamma = 495$ and 808 keV are weakly observed above the background level. This is an indication that ^{14}C may be populated, however the fraction of the ^{14}C particles moving backwards after the collision with the ^{194}Pt appears too small to be observed with sufficient statistics after a particle gate is applied.

To conclude, unfortunately no γ-rays from ^{14}C was observed in the p-γ coincidence spectra. This makes the analysis of the ^{194}Pt(^{14}C,^{14}C')^{194}Pt non trivial, this will be elaborated on in Chapter 6. The collected ^{194}Pt data can still be analysed using the Coulomb excitation code GOSIA to extract valuable information on the electromagnetic structure of this nucleus.

5.4.2 ^{194}Pt

The only information on the ^{194}Pt recoil angle comes from the binary partner, ^{14}C. The trajectory (angle) and energy of ^{194}Pt can be reconstructed using two body kinematics. From the kinematics calculations the average recoiling ^{194}Pt particle had ~ 10 MeV energy corresponding to $\beta \sim 1\%$. This average β can be used to perform a Doppler correction, shown in Fig. 5.11. Due to the poor resolution of the LaBr$_3$(Ce) detectors only the HPGe spectra could be used in the ^{194}Pt analysis. The non-corrected spectrum is shown in red and the Doppler corrected spectrum in blue. The speed of the recoiling ^{194}Pt is small and the Doppler correction has a very minor impact on the γ-ray spectrum. Fig. 5.12 shows the Doppler corrected p-γ coincidence, background subtracted spectrum with the γ-ray transitions of interest identified.

The purity of the target was measured by the Cambridge Isotope Laboratory company, Euriso-top [75], the results are shown in Tab. 5.3. From the purity of the target it can

(a) LaBr$_3$(Ce) Singles

(b) HPGe Singles

(c) HPGe Singles
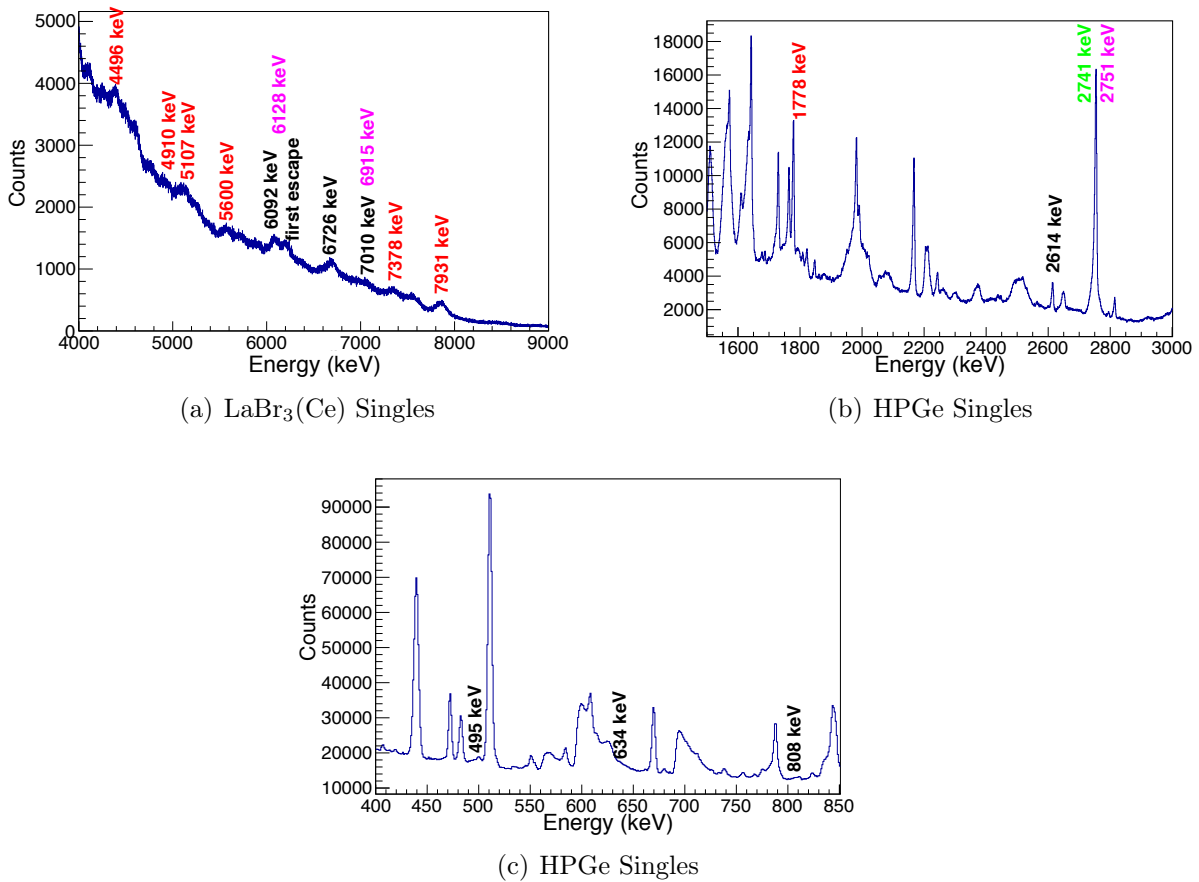
Figure 5.10: Singles γ-ray spectra of all data are shown in (a) where ^{14}C is shown in black, ^{16}O is in magenta and ^{28}Si in red. Singles γ-ray for one HPGe clover at high energy is shown in (b) where ^{28}Si is shown in red, ^{16}O in green, ^{208}Pb in black and ^{208}Tl in magenta. Singles γ-ray for one HPGe clover at low energy is shown in (c) where ^{14}C is shown in black.
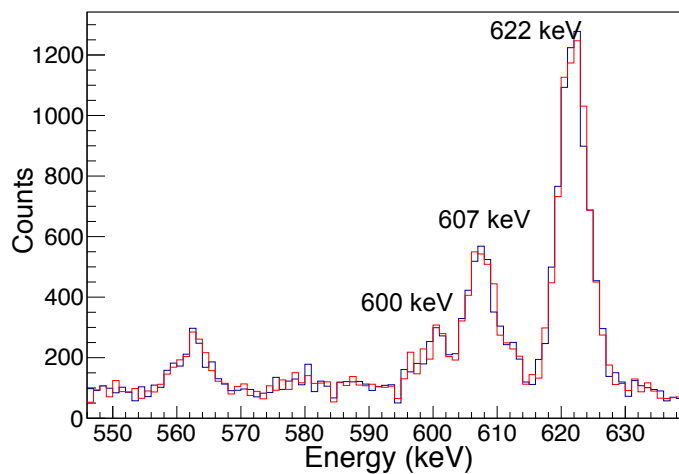
Figure 5.11: The summed Doppler corrected γ-ray spectrum (blue) from the target excitation of ^{194}Pt collected in all HPGe detectors. The non-Doppler corrected spectrum is shown in red.

Table 5.3: The isotopes and purity of the Pt isotopes in the Pt target as measured by Euriso-top [75].

Isotope	^{190}Pt	^{192}Pt	^{194}Pt	^{195}Pt	^{196}Pt	^{198}Pt
Purity	0.01 %	0.03 %	96.45 %	2.46 %	0.87 %	0.18 %

Table 5.4: The spin and parity of the initial, $I_{initial}$ and final, I_{final} levels for γ-rays depopulating states in ^{194}Pt are shown here. The energy of the levels and γ-rays are also indicated.

$I_{initial}$	$E_{initial}$ (keV)	I_{final}	E_{final} (keV)	E_γ (keV)
2^+_1	328	0^+_1	0	328
2^+_2	622	0^+_1	0	622
2^+_2	622	2^+_1	328	294
4^+_1	811	2^+_1	328	482
4^+_2	1229	4^+_1	811	418
4^+_2	1229	2^+_2	622	607
4^+_2	1229	2^+_1	328	901 (Observed weakly)
6^+_1	1411	4^+_1	811	600
3^-_1	1432	4^+_1	811	621
3^-_1	1432	2^+_2	622	810
3^-_1	1432	2^+_1	328	1104

Table 5.5: The spin and parity of the initial, $I_{initial}$ and final, I_{final} levels for γ-rays depopulating states in ^{195,196}Pt are shown here. The energy of the levels and γ-rays are also indicated.

Isotope	$I_{initial}$	$E_{initial}$ (keV)	I_{final}	E_{final} (keV)	E_γ (keV)
^{196}Pt	2^+_1	355	0^+_1	0	355
^{195}Pt	$\frac{3}{2}^-_3$	211	0^+_1	0	211
^{195}Pt	$\frac{1}{2}^-_1$	222	0^+_1	0	222 (Observed weakly)
^{195}Pt	$\frac{5}{2}^-_2$	239	0^+_1	0	239

be concluded that little contamination is present.

Due to the 2.46 % and 0.87 % presence of the ^{195}Pt and ^{196}Pt isotopes, their γ-ray transitions are also observed in the spectrum. The small percentage of ^{195,196}Pt present has little impact because the γ-ray energies from different isotopes can be resolved by the HPGe detectors. The γ-rays depopulating states in ^{194}Pt are listed in Tab. 5.4 and the γ-rays depopulating states and identified in the spectra of ^{195,196}Pt are listed in Tab. 5.5.

The p-γ coincidence spectrum is a good indication of which states are observed in the experiment, however to confirm which lines are coming from the isotope of interest a γ-γ
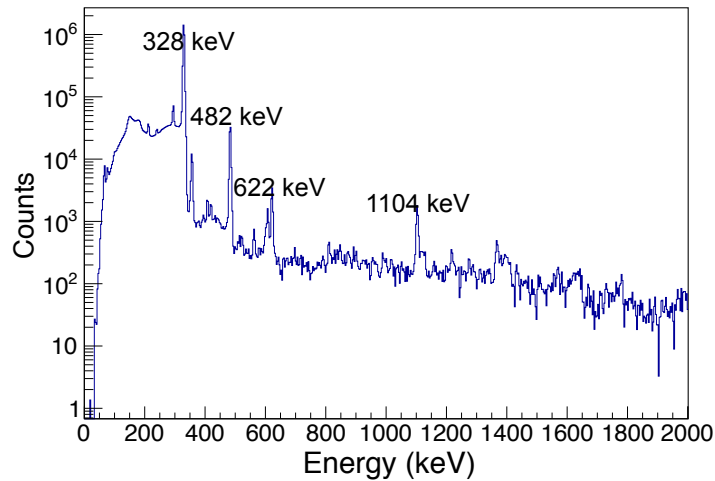
Figure 5.12: Doppler corrected, p-γ gated γ-ray spectra from all the HPGe detectors. The γ-rays of interest for ^{194}Pt are identified.

coincidence analysis is required. For example from the 2_2^+ state of ^{194}Pt, the nucleus can undergo the transitions:

- $2_2^+ \rightarrow 0_1^+$ emitting a 622 keV γ-ray,

- or $2_2^+ \rightarrow 2_1^+$ and $2_1^+ \rightarrow 0_1^+$ emitting a 294 and 328 keV respectively.

The partial level scheme indicating these transitions are shown in Fig. 5.13. From these transitions three γ-rays are emitted: 622 keV, 294 keV and 328 keV. These γ-rays are observed in the p-γ gated spectra, shown in Fig. 5.12 which means these γ-rays are in coincidence with the ^{14}C particles. It does not guarantee that they are emitted by ^{194}Pt. The $\gamma - \gamma$ gated spectra can be used as an additional test, for example when gating on the 328 keV γ-ray the 293.5 and 328 keV should be in coincidence and both must be observable in the $\gamma - \gamma$ gated spectra. A similar analysis is done for all the ^{194}Pt γ-rays of interest.

The statistics collected with the p-γ-γ coincidence condition, presented in Fig. 5.14(a), is insufficient to draw any conclusions therefore only γ-γ coincidence analysis could be performed, as shown in Fig. 5.14(b). Only those γ-rays observed in p-γ and various gated γ-γ coincidences are included in further analysis using the GOSIA code.
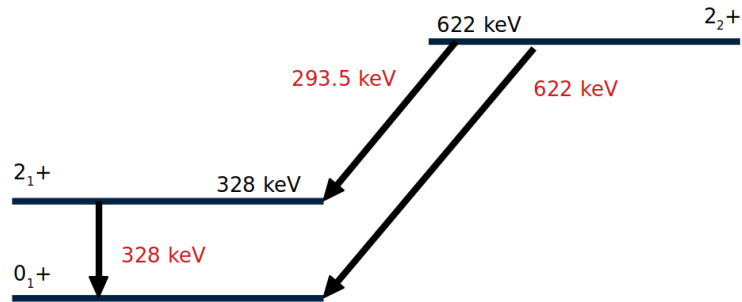
Figure 5.13: A partial level scheme of ^{194}Pt showing the possible transitions from the 2_2^+ to the 0_1^+ state. The level's energies are shown in black and the γ-ray energies are shown in red.
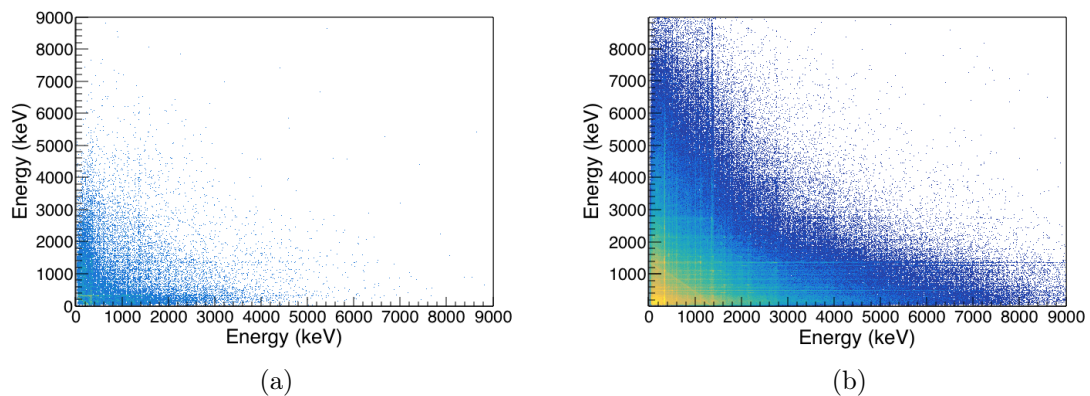
Figure 5.14: The p-γ-γ matrix does not have enough statistics (a) so the γ-γ coincidence matrix (b) is used to identify γ-rays that will be used in the Coulomb excitation analysis.

Chapter 6

GEANT4

GEANT4 [76, 77, 78] is a dedicated open source C++ toolkit that is used to simulate the interaction of different radiation types with matter. This simulation toolkit includes functionality for particle tracking, construction of complex experimental geometry, visualisation framework, application of physics models and radiation interaction with the detector material. The abstract functionality enables a high level of customisation to suit many different purposes. The physics processes included in the toolkit cover electromagnetic, hadronic and optical processes between energies of 250 eV to several TeV. It has been adopted in space, medicine, particle and nuclear physics segments.

In order to evaluate the amount of signal within the experimental background, a good estimation of the shape of the Doppler shifted distribution is required. The response function of the LaBr$_3$(Ce) material to the interaction of a Doppler shifted $2_1^+ \rightarrow 0_1^+$ transition of 7.01 MeV energy emitted by the ^{14}C can be simulated using the GEANT4 toolkit. The GEANT4 simulated experimental setup is presented in Fig. 6.1. Here, the same angles and distances are used as in the actual experiment.

6.1 Theory

In the simulated reaction, the 45 MeV ^{14}C beam collides with the ^{194}Pt target. The recoiling angles of ^{194}Pt are between $\theta_{lab} = 9.7°$ and 22.5° when the ^{14}C projectile is detected in the S3 array placed between $\theta_{lab} = 132°$ and 159°. The kinetic energy of the recoiling ^{194}Pt is between 9.7 and 11 MeV while the energy of ^{14}C is between 34 and 35.2 MeV. This two-body kinematics is illustrated in Fig. 6.2 and the calculation is performed using a dedicated C++ code written for this simulation. The recoiling or ejected nucleus undergoes an isotropic γ-decay while still moving with some residual kinetic energy. Below, a brief overview of the two-body kinematics is presented and a detailed description
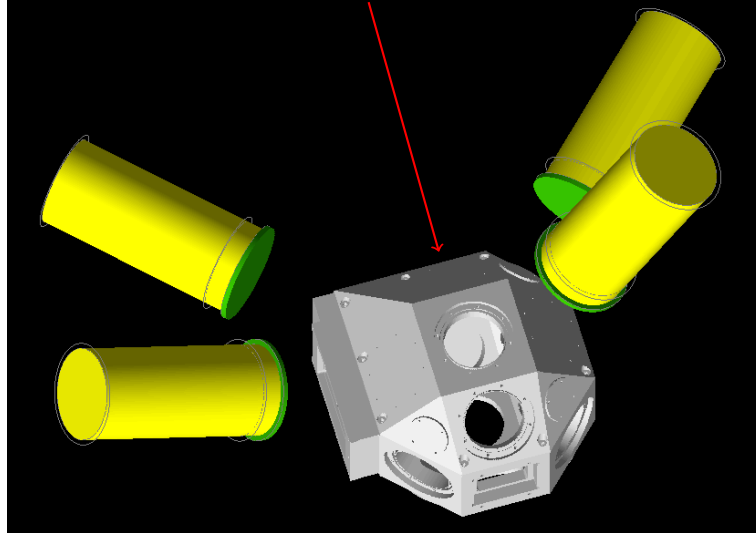
Figure 6.1: The simulated setup used in GEANT4. This setup mirrors the experimental setup and the red line indicates the beam direction.

can be found in Ref. [37].

Using the conservation of linear momentum the following equation can be obtained:

$$p_i = p_f cos(\theta) + p_a cos(\phi) \tag{6.1}$$

$$0 = p_f sin(\theta) - p_a sin(\phi). \tag{6.2}$$

Here p is linear momentum, the subscript f corresponds to the ejectile, a to the recoil and i to the incoming particle. From the conservation of energy law:

$$E_i + Q = E_f + E_a + E_x, \tag{6.3}$$

where Q is the Q-value, which is 0 for Coulomb excitation reactions since there is no exchange of nucleons between the projectiles and target nuclei and there is no change in mass. E is the sum of the kinetic energy and the rest mass energy and E_x is used for the particle excitation energy. The set of equations can be solved and the recoiling and ejectile energy and angle can be calculated. From the kinetic energy the velocity is calculated with Eq. 4.6.

The γ-rays are Doppler shifted by Eq. 2.38. For example, with $\alpha = 135°$, $\beta = 0.07$ and the emitted γ-ray and particle moving in the opposite direction, $E_\gamma = 7010$ keV is shifted to 6660 keV. If the γ-ray and particle is moving in the same direction then the γ-ray is shifted to $E_\gamma = 7480$ keV. In this example the Doppler shift spreads the γ-ray across 800 keV. Without Doppler correction this γ-ray will not be observable.
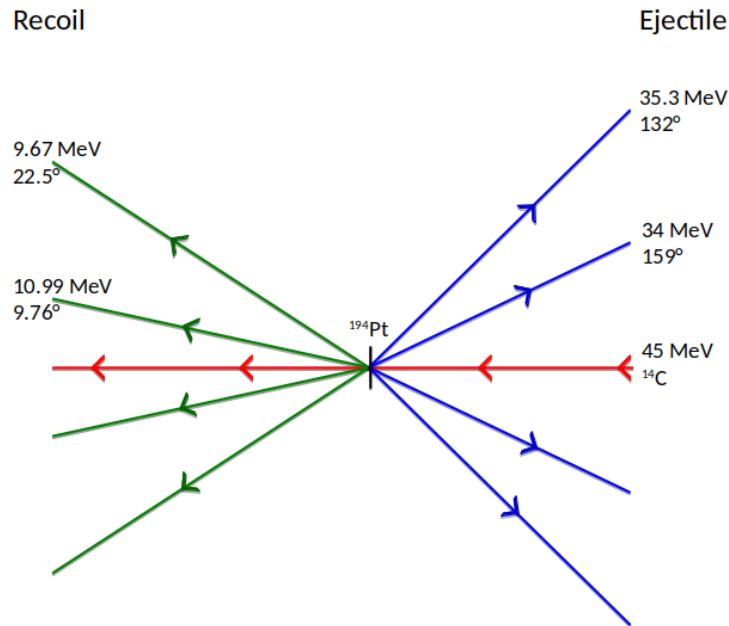
Figure 6.2: Two-body kinematics of the ^{14}C projectile on a ^{194}Pt target. The backscattered ^{14}C is shown in blue and the corresponding ^{194}Pt recoil is shown in green. The 45 Mev ^{14}C beam is shown in red.
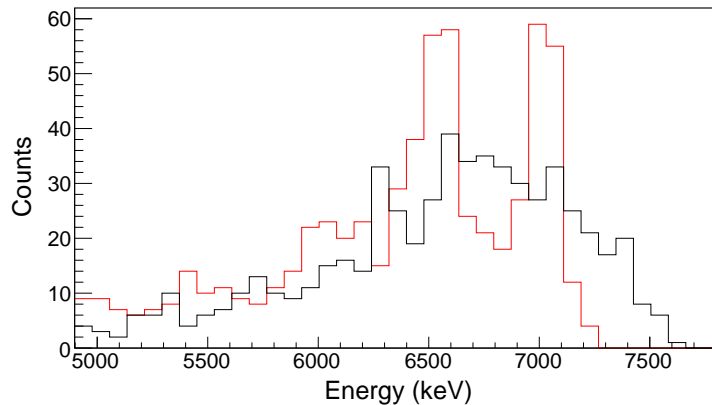
Figure 6.3: The Doppler shifted γ-rays are shown in black and the Doppler corrected γ-rays are shown in red for a LaBr$_3$(Ce) detector.

The Doppler shifted and corresponding Doppler corrected γ-ray spectrum was simulated for a LaBr$_3$(Ce) detector. The Doppler shifted γ-rays are shown in black in Fig. 6.3. The Doppler corrected γ-ray spectrum is shown in red. The importance of Doppler correction is highlighted by the fact that no peaks can be identified in the Doppler shifted spectrum, however the Doppler corrected spectrum has a clear 7.01 MeV peak.
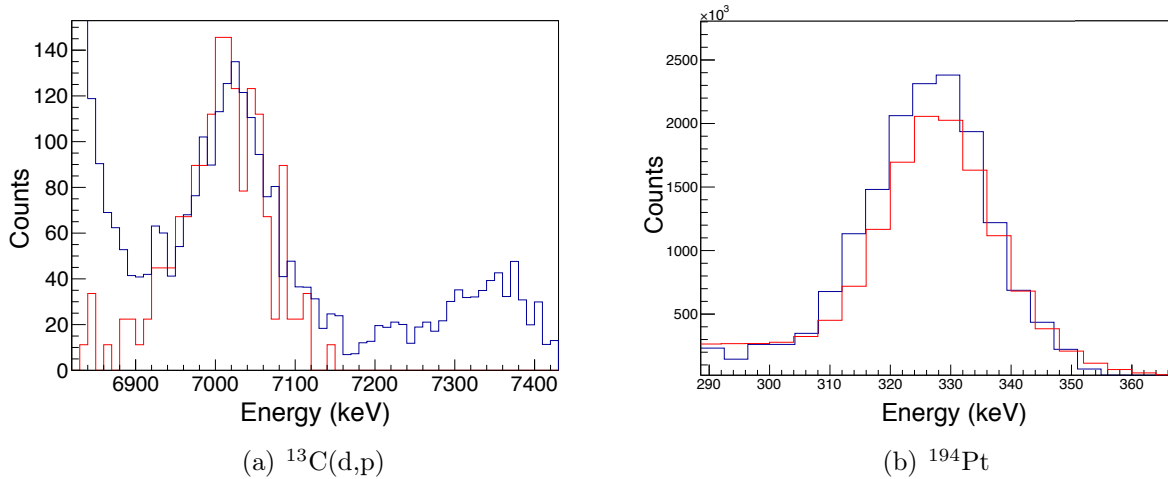
Figure 6.4: The GEANT4 γ-ray spectrum simulation (red) compared with experimental LaBr$_3$(Ce) γ-ray spectrum (blue). The high energy from the Doppler corrected ^{13}C(d,p) reaction is shown in (a) and the low energy from the p-γ gated, ^{194}Pt Coulomb excitation result is shown in (b).

6.2 Results

The simulated data are compared to the measured γ-ray spectrum from the combined LaBr$_3$(Ce) detectors. The γ-ray spectrum from the LaBr$_3$(Ce) for the ^{13}C(d,p)^{14}C reaction is shown in Fig. 6.4(a) and the 328 keV transition in ^{194}Pt is shown in Fig. 6.4(b). The energy resolution is reproduced and the simulations compare well with the experimental data for the purpose of obtaining the line shape. The line shape at 7 MeV is indicative of the overall response from the LaBr$_3$(Ce) detectors. The simulation did not include any experimental cross sections, hence only the line shape can be compared. The amplitude of the line shape can be fitted using a likelihood algorithm [79]: the amplitude is varied in small (0.01 keV) steps and for each step the χ^2 is calculated. The solution with the smallest χ^2 in the energy region of interest is kept as the best fit.

The rebinned ^{14}C γ-ray spectrum collected from the Coulomb excitation data is shown in Fig. 6.5. The background is fitted with an exponential function below 5 MeV and with a straight line above 7.5 MeV. The background is then subtracted from the region of interest.

The results of the simulation is compared to the background subtracted experimental data in Fig. 6.6. The green line is the background subtracted data and the blue line (which is not observable) is the non-subtracted data. On average ≈ 0.2 counts per bin is subtracted from the data in the region of interest, 6-8 MeV. This indicates that the various gates eliminate most of the background.
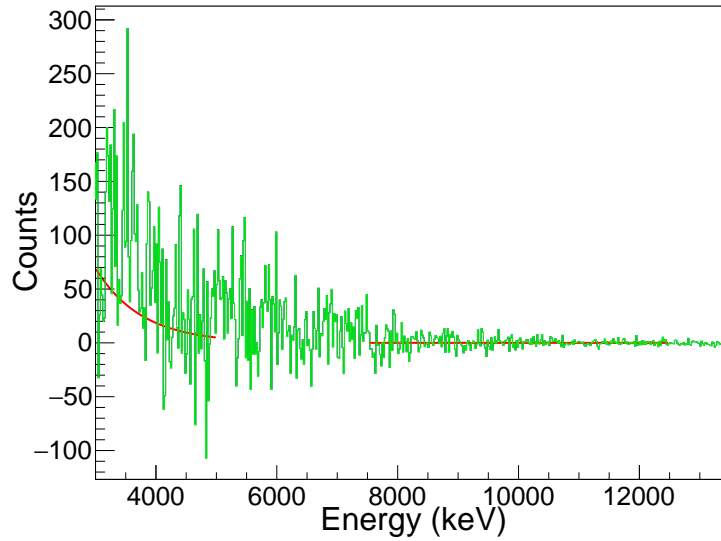
Figure 6.5: The rebinned, gated and Doppler corrected ^{14}C γ-ray spectrum collected from the Coulomb excitation data are shown in green for 20 keV per bin. The background fits are shown in red.

The simulated data is fitted to the experimental data with a likelihood approach using the amplitude as a free parameter. If the fit is applied to the 7.01 MeV region the best fit has a χ^2 of 284.7. The simulated $2_1^+ \to 0_1^+$ transition of ^{14}C shows clearly defined distributions which are not observed experimentally. The experimental counts in the 7.01 MeV peak (6.9 - 7.1 MeV) is 88. At first glace this may look like the 2_1^+ state of ^{14}C, however the amount of counts in the 6.5 MeV region (6.4-6.7 MeV) is 9. From the detector response it is visible that the first escape should contain $\approx 60\%$ of the counts in the full energy peak. This is not the case in the collected data and the counts may be statistical fluctuations.

The exact number of counts in the full energy region and first escape region may change depending on the binning and the width of the defined region, but the first escape region never contains $\approx 60\%$ of the counts of the full energy region. Additionally, no other possible ^{14}C transitions are observed. This further supports the conclusion that no ^{14}C is populated in the p-γ coincidence spectra from the current experiment.
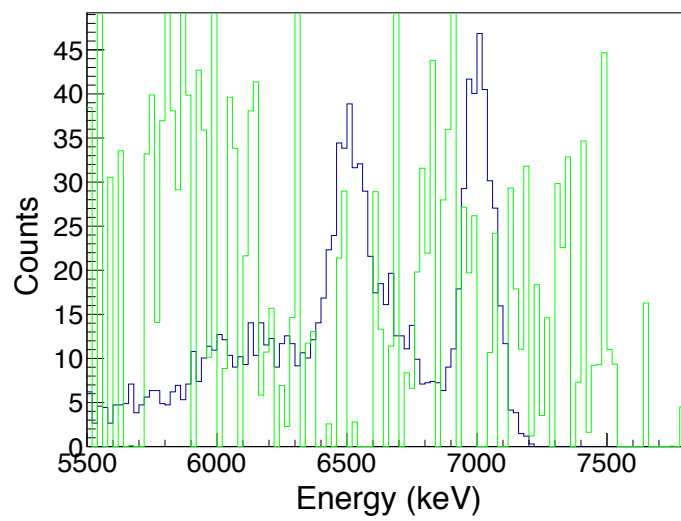
Figure 6.6: Simulation (blue) comparison with background subtracted ^{14}C experimental data (green) are shown in 20 keV per bin divisions.

Chapter 7

Coulomb excitation data analysis of ^{194}Pt

7.1   The GOSIA code

The Coulomb excitation data analysis was performed using the GOSIA code [19]. It is a Fortran program that was developed to analyse large Coulomb excitation data sets involving numerous transitions and many matrix elements. It provides an advanced tool for global minimisation of the χ^2 function to fit the set of matrix elements to the experimentally observed γ-ray yields. This allows for the extraction of information on the electromagnetic properties of the nucleus of interest. This code can minimise matrix elements and at the same time take into account the information provided by the user: the level scheme, known lifetimes, branching ratios, mixing ratios or previously measured quadrupole moments. The GOSIA code allows for a sophisticated error estimation which considers the correlated uncertainties of all matrix elements simultaneously. From such an advanced analysis and with sufficient statistics, the nuclear deformation for each individual state can be determined using the quadrupole sum rule method described in Chapter 2.7.

The χ^2 fitting function used in the GOSIA analysis is given by a following equation:

$$
\chi^2 = \frac{1}{N} \left(\sum_{I_e, I_d} w_{I_e, I_d} \sum_{k_{I_e, I_d}} \frac{1}{\sigma_k^2} (C_{I_e, I_d} Y_k^c - Y_k^e)^2 \right) +
$$
$$
\frac{1}{N} \left(\sum_j \left(\frac{Y_j^c(I_e, I_d)}{Y_n^c(I_e, I_d)} - u(I_e, I_d) \right)^2 \cdot \frac{1}{u^2(I_e, I_d)} \right) + \tag{7.1}
$$
$$
\frac{1}{N} \left(\sum_i w_i \sum_{n_i} (d_{n_i}^c - d_{n_i}^e)^2 \cdot \frac{1}{\sigma_{n_i}^2} \right),
$$

where:

- N is the number of all experimental data sets (the sum of all measured γ-ray yields, lifetimes, branching ratios, mixing ratios and known E2 matrix elements)

- I_e is the number of all analysed data sets defined by the user,

- I_d is the number of γ-ray detectors,

- Y^e, Y^c are the experimental and calculated γ-ray yields,

- w_{I_e,I_d} are the weights, selected for each experiment and detector separately,

- d^e, d^d are experimental and calculated spectroscopic information (lifetimes, branching ratios, mixing ratios and known E2 matrix elements),

- w is the weight of all spectroscopic data,

- σ is the experimental uncertainty (determined for every spectroscopic information separately),

- C_{I_e,I_d} is the normalisation coefficient (one for all the data sets),

- Y_n^e is the intensity of the normalisation transition,

- u_{I_e,I_d} is the so-called upper limit, the ratio of the weakest transition possible to be observed in the experiment to the normalisation transition, chosen by the user (in the work presented here it is the $2_1^+ \rightarrow 0_1^+$ transition of ^{194}Pt).

Statistical errors of the matrix elements are estimated after the χ^2 function has reached a global minimum. There are two steps in the error estimation process. First, the uncorrelated uncertainties are obtained by sampling each matrix element about the χ^2 surface minimum. A point is found where the total probability distribution is equal to 1σ. At the same time a multi-dimensional correlation matrix is built. For this matrix a global best fit χ^2 is found with respect to all parameters. The uncertainty can then be given by the region of the surface for which the total probability distribution is equal to 1σ. This region is defined by the total $\chi^2 = \chi^2 + 1$.

7.2   Results – ^{14}C

As discussed in Ch. 6 no ^{14}C excitation is observed, however the simultaneous χ^2 minimisation of ^{14}C and ^{194}Pt is performed in an attempt to calculate the upper limit of the B(E2: $2_1^+ \rightarrow 0_1^+$) using the GOSIA code. The 88 counts observed in the 6.9 - 7.1
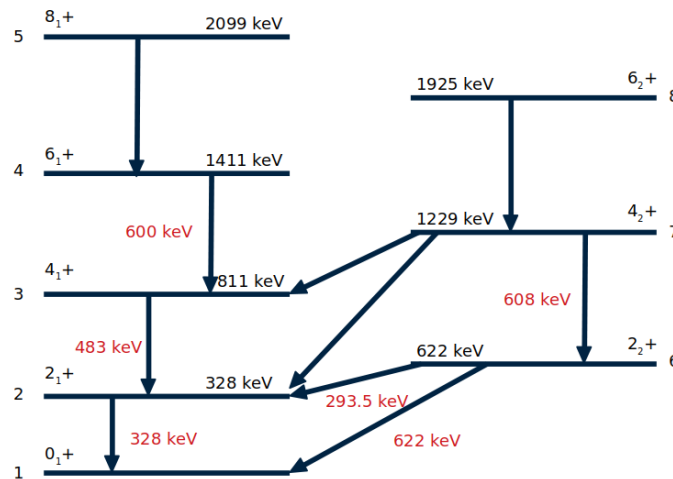
Figure 7.1: The level scheme of ^{194}Pt used in the present Coulomb excitation analysis using the GOSIA code. The values in red indicate γ-ray energies and those in black indicate the level energies. The arrows indicate de-excitations between levels. The spin and index used in the GOSIA analysis is indicated for each level individually.

MeV region is used as the "assumed" experimental γ-ray yield of the 2_1^+ state of ^{14}C. The global minimisation of the χ^2 function could not reproduce the matrix elements of ^{194}Pt and no limit could be placed on the B(E2: $2_1^+ \rightarrow 0_1^+$) of ^{14}C.

Since the 2_1^+ state is not observed in the Doppler corrected experimental γ-ray spectrum, the GEANT4 simulation suggests it is not hidden in the background and the GOSIA analysis cannot minimize the matrix elements of ^{194}Pt and ^{14}C no further analysis is done for ^{14}C.

7.3   Results – ^{194}Pt

The ^{194}Pt nucleus has been extensively studied using the Coulomb excitation technique [11, 12, 13, 14, 15, 16, 17] and the spectroscopic properties of the low-lying states are known.

The level scheme adopted for the GOSIA analysis is shown in Fig. 7.1. The γ-ray energies marked in red were observed in γ-γ and p-γ coincidences shown previously in Figs. 5.14(b) and 5.12. The 6_2^+ and 8_1^+ states where not populated but were included in the analysis as so-called buffer states. Such states are introduced to properly account for possible excitation of the higher states although the emission of γ-ray transition was impossible to be observed. The levels presented in black were included in the GOSIA analysis. The levels are indexed following the GOSIA input assignment.

The experimental p-γ data was divided into subsets using the information on the scattering angle, θ. The total θ range covered by the particle detector is between 132.6°-159.4°. Three different angular divisions: no division, 2 and 4 angular ranges, were introduced to find the optimum number of subsets in order to minimise the effect of statistical uncertainty on the observed yields and maximise the sensitivity to the secondary order effects, such as the spectroscopic quadrupole moments. The ranges were selected as follows:

- 1 range: 132.6°-159.4° (full detector, no division)

- 2 ranges: (132.6°-143.2°) and (144.4°-159.4°)

- 4 ranges: (132.6°-137.9°), (137.9°-143.2°), (143.2°-151.3°) and (151.3°-159.4°)

The division into 4 θ ranges provided more experimental points to fit as the same γ-ray yields were observed in all subsets, but this leads to low intensity lines with big uncertainties which affected the precision of the analysis. The approach with full θ range was acceptable, however the best results were obtained with two θ angular ranges. Therefore this division was kept and used for the analysis.

7.3.1 Spectroscopic information

A set of known spectroscopic information was introduced in the analysis to constrain the fit of the matrix elements in order to reproduce the observed experimental γ-ray yields in the most accurate way. The spectroscopic information include half lives, branching ratios, mixing ratios and known experimental matrix elements. The experimental γ-ray yields used in the Coulomb excitation analysis are also presented in this section.

7.3.1.1 Half lives

One of the most important experimental information that help to perform a normalisation to the known data points is the half live of the excited state. The 2_1^+ half life value was taken from Ref. [11] as it was the most recent measurement and similar to those of Refs. [14, 16]. The half life of the 4_1^+ state was taken as the average obtained in two experiments, [12, 11]. The other half lives were taken from Ref. [17] for 6_1^+, 8_1^+, 4_2^+ and 6_2^+ states and from Ref. [15] for the 2_2^+ state.

The half lives obtained from this work are compared to the known half lives in Tab. 7.1. Those used in the analysis are marked in bold. The evaluated half lives are in good agreement with previously known values shown in Tab. 7.1. The half life of 8_2^+ does not

agree well with the previously measured one, however this state was not observed in the present experiment and has been introduced in the GOSIA analysis as a buffer state.

Table 7.1: Half lives determined in this work compared to the known half lives of ^{194}Pt. The lifetimes which were used as the known spectroscopic data in the present analysis using the GOSIA code are shown in bold. The calculated half lives are obtained from B(E2: $2_1^+ \to 0_1^+$) values from Coulomb excitation, the centroid shift method (CSM), Doppler shift attenuation method (DSAM) and recoil distance method (RDM).

Level	Half life (ps) This work	Half life (ps) Others	Method
2_1^+	41.9(5)	**41.6(6)**	Calculated [11]
		45.0(24)	RDM [12]
		37.7(18)	Calculated [13]
		50.5(22)	RDM [80]
		41.8(5)	Calculated [14]
		34.7(35)	CSM [15]
		41.8(29)	Inelastic α scattering [16]
4_1^+	3.6(2)	**3.7(2)**	RDM [12]
		4.4(7)	Calculated [11]
		4.85(139)	DSAM [17]
6_1^+	1.2(5)	**1.6(5)**	DSAM [17]
8_1^+	0.76(30)	**1.11(35)**	DSAM [17]
2_2^+	26(4)	**35(4)**	CS method [15]
4_2^+	3.8(6)	**3.8(6)**	DSAM [17]
6_2^+	1.2(2)	**1.3(2)**	DSAM [17]

7.3.1.2 Branching ratios

The experimentally known branching ratios used in the present analysis were adopted from Ref. [81]. The fitted branching ratios are compared to the known ones as presented in Tab. 7.2. The agreement between the known data and the GOSIA fit is very good and within 1σ.

7.3.1.3 Mixing ratios

The only mixing ratio value in ^{194}Pt is known for the $2_2^+ \to 2_1^+$ transition: $\delta(E2/M1) = 15(2)$ [81]. The value obtained in the GOSIA analysis is equal to 14.88 and is within 1σ

Table 7.2: Known branching ratios from Ref. [81] compared to the calculated branching ratio for each transition in ^{194}Pt. The variance between the known and calculated branching ratios is given by σ.

Transition	γ-ray intensity (%) Ref. [81]	γ-ray intensity (%) This work	σ
$2_2^+ \rightarrow 0^+$	13.69(23)	13.3	0.2
$2_2^+ \rightarrow 2_1^+$	100		
$4_2^+ \rightarrow 4_1^+$	14.4(14)	14.3	0.1
$4_2^+ \rightarrow 2_1^+$	12.2(8)	12.3	0.1
$4_2^+ \rightarrow 2_2^+$	100		
$6_2^+ \rightarrow 4_1^+$	12(4)	11.9	0.0
$6_2^+ \rightarrow 4_2^+$	100		
$6_2^+ \rightarrow 6_1^+$	6(4)	7.1	0.3

agreement.

7.3.1.4 Experimental matrix elements

In the present analysis the information on the known matrix elements from Ref. [18] were introduced in the input files as additional constraints. The initial set of matrix elements were adopted from previous measurements, however in the course of the analysis, the χ^2 fit of the matrix elements to the experimental data was performed. Overall, the extracted set of matrix elements from this work are in good agreement with the previous works. The full set of matrix elements obtained from the analysis will be discussed in Sec. 7.3.2. The Q_{sp} given as input, compared the obtained Q_{sp} from this work are shown in Table 7.3.

Table 7.3: Known spectroscopic moments Q_{sp} of ^{194}Pt given as input compared to the calculated Q_{sp} for each transition. The variance between the experimental and calculated values are indicated by σ.

Level	Q_{sp} (e.b.) Ref. [18]	Q_{sp} (e.b.) This work	σ
2_1^+	$0.41^{0.06}_{-0.05}$	$0.4^{0.05}_{-0.05}$	0.16
4_1^+	$0.75^{0.1}_{-0.1}$	$0.7^{0.1}_{-0.1}$	2.1e-2
6_1^+	$0.2^{0.07}_{-0.19}$	$0.18^{0.14}_{-0.14}$	1.8e-3
2_2^+	$-0.30^{0.09}_{-0.03}$	$-0.29^{0.07}_{-0.08}$	0.23
4_2^+	$-0.05(11)$	$-0.05^{0.1}_{-0.1}$	2.2e-2

7.3.1.5 Experimental yields

The p-γ yields are obtained by integrating the background subtracted γ-ray spectra for all HPGe detectors. It should be noted that the 428 keV peak had a bigger FWHM (5.1 keV) compared to neighbouring peaks, for example the 443 keV from ^{152}Eu has a FWHM of 3.5 keV. Some contamination is suspected for this line and because it was impossible to resolve this region, even using the known branching ratios, this line was not included in the analysis. All other transitions are pure and show no indication of contamination.

The yields used in the analysis are efficiency corrected. The following efficiency function obtained using Eq. 4.4 was applied for the combined HPGe γ-ray detectors:

$$
\epsilon(E) = 9.01 \times 10^{-2} + 0.57 \log(E_\gamma) - 5.15 \times 10^{-2} \log(E_\gamma)^2 -
$$
$$
1.43 \times 10^{-2} \log(E_\gamma)^3 + 1.52 \times 10^{-3} \log(E_\gamma)^4. \tag{7.2}
$$

The γ-ray yields observed in the present experiment are presented in Tab. 7.4. These yields are compared to the fitted ones obtained using the extracted set of matrix elements in Tabs. 7.5 and 7.6. The fitted yields do not have uncertainties since they are obtained from a fit, instead the variance σ between the experimental and reproduced yields is given in Tab 7.4. The experimental data is well reproduced within the experimental uncertainties by the calculated yields.

Table 7.4: The reproduced and experimental yields for each considered transition in ^{194}Pt. The variances between the experimental and reproduced yields are given by σ.

Transition	E_γ (keV)	Experimental yield	Reproduced yield	σ
		$\theta = 144.4 - 159.4$		
$2_1^+ \to 0_1^+$	328	2.2e6 (1.1e5)	2.2e6	0.0
$4_1^+ \to 2_1^+$	483	7.7e4 (7.7e3)	7.2e4	0.6
$6_1^+ \to 4_1^+$	600	6.1e2 (3.1e1)	6.3e2	1.0
$2_2^+ \to 2_1^+$	294	6.3e4 (3.2e3)	5.9e4	1.2
$4_2^+ \to 2_2^+$	608	2.8e3 (1.4e2)	2.8e3	0.3
		$\theta = 132.6 - 143.2$		
$2_1^+ \to 0_1^+$	328	3.5e6 (1.8e5)	3.8e6	1.2
$4_1^+ \to 2_1^+$	483	1.1e5 (1.1e4)	1.1e5	0.1
$6_1^+ \to 4_1^+$	600	1.0e3 (5.1e2)	9.5e2	1.3
$2_2^+ \to 2_1^+$	294	8.7e4 (4.3e3)	8.9e4	0.4
$4_2^+ \to 2_2^+$	608	4.4e3 (2.2e2)	4.3e3	0.6

7.3.2 Electric quadrupole transition strengths and spectroscopic moments.

Experimental matrix elements, electric quadrupole transition strengths B(E2: $2_1^+ \to 0_1^+$), and spectroscopic moments Q_{sp}, obtained in the course of the present analysis, reproducing known spectroscopic information available for ^{194}Pt are presented in Tab. 7.5 for the ground state band and in Tab. 7.6 for the γ-band. The matrix elements of the values in bold where given as input to constrain the fit. These tables contain the matrix elements which were extracted with an uncertainty smaller than 70% allowing for a discussion of the electromagnetic properties of ^{194}Pt.

The matrix elements of the $2_1^+ \to 0_1^+$ and $6_1^+ \to 4_1^+$ transitions are measured with increased precision compared to previous measurements. The obtained values of the spectroscopic quadrupole moments of 2_1^+ and 4_1^+ states are very well reproduced in the present analysis. The value of the $Q_{sp}(2_2^+)$ has been obtained with a reduced uncertainty in comparison to the previous values reported in Refs. [18, 82].

The matrix elements for transitions de-exciting the 8_1^+ and 6_2^+ buffer states have high uncertainties because these lines were not observed experimentally, therefore the fit of those matrix elements was performed based only on the spectroscopic information known from the previous experiments [17]. Similarly, only one of the 3 γ-ray decays from the 4_2^+ state is observed in the γ-ray spectra. Interestingly, the unobserved $4_2^+ \to 2_1^+$ and $4_2^+ \to 4_1^+$ transitions' matrix elements agree within the error bars with previous measurements from Ref. [83], however the $4_2^+ \to 6_1^+$ and $4_2^+ \to 2_2^+$ matrix elements do not agree with previous measurements [18]. The $2_2^+ \to 2_1^+$ and $2_2^+ \to 0_1^+$ matrix element values are bigger than those from any other measurement, due to the increased matrix element value of the $4_2^+ \to 2_2^+$ transition that populates the 2_2^+ state.

7.3.2.1 Relative signs of matrix elements

To check the sensitivity on the sign of the matrix elements, several tests were performed. As an example, the ratio of $\frac{2_2^+ \to 2_1^+}{2_1^+ \to 0_1^+}$ yields was simulated using the GOSIA code between 0-180° for different signs of the $2_2^+ \to 2_2^+$ matrix element, as shown in Fig. 7.2 for the range between 100 and 180°. The value of the $2_2^+ \to 2_2^+$ matrix element is equal to -0.4 (e.b.) in Refs. [18, 83]. The experimental yield ratio is indeed very close to the simulation indicating that the analysis is sensitive to the sign of this matrix element.

Further checks of the sensitivity on the sign of matrix elements were performed using the minimisation procedure. The χ^2 analysis was performed for 1 iteration for a given matrix element with a certain sign which was then changed and 1 iteration of minimisation was

Table 7.5: Experimental matrix elements $< I_i||E2||I_f >$, electric quadrupole transition strengths B(E2: $2_1^+ \rightarrow 0_1^+$), and spectroscopic moments Q_{sp}, for this and other work. These properties describe the low-lying electromagnetic structure of ^{194}Pt – the ground state band. The matrix elements are from Coulomb excitation (Coulex), Recoil distance method (RDM) and Doppler shift attenuation method (DSAM).

Transition	$< I_i\|\|E2\|\|I_f >$ (e.b.) This work	B(E2) (W.u.) This work	B(E2) (W.u.) Other work	Method
$2_1^+ \rightarrow 0_1^+$	$+1.290^{0.01}_{-0.01}$	$49.9^{0.8}_{-0.8}$	$\mathbf{43.8^{3.6}_{-1.2}}$	Coulex [18]
			56.3(25)	Coulex [84]
			46.5(30)	RDM. [12]
			48.6(4)	Coulex [83]
$4_1^+ \rightarrow 2_1^+$	$+2.38^{0.07}_{-0.05}$	$94.3^{5.7}_{-3.9}$	$(+)\mathbf{62.4^{1.2}_{-0.9}}$	Coulex [18]
			85.1(45)	RDM [12]
			70.7(49)	Coulex [17]
			67.3(34)	Coulex [83]
$6_1^+ \rightarrow 4_1^+$	$+2.63^{0.06}_{-0.07}$	$79.8^{3.6}_{4.2}$	$(+)\mathbf{97^{6.8}_{-2.7}}$	Coulex [18]
			48(12)	Coulex [17]
			72(22)	DSAM [17]
$8_1^+ \rightarrow 6_1^+$	$+2.99^{0.46}_{-1.06}$	$78.8^{26.2}_{-46.0}$	$(+)\mathbf{83.6^{5.6}_{-8.4}}$	Coulex [18]
			53.8(178)	DSM [17]
State	$< I_i\|\|E2\|\|I_f >$ (e.b.) This work	Q_{sp} (e.b.) This work	Q_{sp} (e.b.) Other work	Method
2_1^+	$+0.52^{0.07}_{-0.07}$	$0.4^{0.05}_{-0.05}$	$\mathbf{0.41^{0.06}_{-0.05}}$	Coulex [18]
			0.62(16)	Coulex [14]
			0.45(7)	Coulex [85]
			0.48(13)	Coulex [86]
4_1^+	$+0.98^{0.14}_{-0.13}$	$0.7^{0.1}_{-0.1}$	$\mathbf{0.75^{0.1}_{-0.1}}$	Coulex [18]
			0.45(90)	Coulex [83]
6_1^+	$+0.26^{0.21}_{-0.19}$	$0.18^{0.14}_{-0.14}$	$\mathbf{0.20^{0.07}_{-0.19}}$	Coulex [18]

performed. If the χ^2 remained unchanged then it indicates that the analysis was not sensitive to the sign of a given matrix elements. For example, when investigating the sensitivity to the sign of the $4_2^+ \rightarrow 4_1^+$ matrix element, the χ^2 did not change when the matrix element sign was inverted.

When the same test was performed for the $2_2^+ \rightarrow 2_1^+$ matrix element, the χ^2 value was equal to 1.35 with a positive sign. When the sign was changed to negative the χ^2 value changes to 7.2. This shows that the analysis is sensitive to the polarity of the matrix

Table 7.6: Experimental matrix elements $< I_i||E2||I_f >$, transition strengths B(E2: $2_1^+ \to 0_1^+$) and B(M1), and spectroscopic moments, Q_{sp}, for this and other works. These properties describe the low-lying electromagnetic structure of ^{194}Pt – the γ band. The matrix elements are from Coulomb excitation (Coulex), $\gamma - \gamma$ directional correlation ($\gamma - \gamma$ DC) and Doppler shift attenuation method (DSAM).

Transition	$< I_i\|\|E2\|\|I_f >$ (e.b) This work	B(E2) (W.u.) This work	B(E2) (W.u.) Other work	Method
$2_2^+ \to 0_1^+$	$+0.112^{0.003}_{-0.002}$	$0.38^{0.02}_{-0.02}$	$+\mathbf{0.24(1)}$	Coulex [18]
			$0.21(3)$	Coulex [17]
			$0.24(1)$	Coulex [83]
$2_2^+ \to 2_1^+$	$+2.01^{0.05}_{-0.05}$	$121.1^{6.1}_{-6.1}$	$(+)\mathbf{69^1_{-2}}$	Coulex [18]
			$86.6(105)$	Coulex [17]
			$63.5(22)$	Coulex [83]
$2_2^+ \to 4_1^+$	$+0.26^{0.67}_{-0.4}$	$2.0^{2.4}_{-1.4}$	$+\mathbf{1.9^{2.7}_{-0.9}}$	Coulex [18]
$4_2^+ \to 2_1^+$	$+0.303^{0.01}_{-0.01}$	$1.5^{0.1}_{-0.1}$	$+\mathbf{0.8(8)}$	Coulex [18]
			$1.5(150)$	Coulex [83]
$4_2^+ \to 4_1^+$	$+2.1^{0.2}_{-0.1}$	$73.4^{14.7}_{-6.8}$	$+\mathbf{38^3_{-2.5}}$	Coulex [18]
			$130(74)$	Coulex [83]
$4_2^+ \to 6_1^+$	$+0.1^{0.3}_{-0.3}$	$0.2^{2.5}_{-2.5}$	$+\mathbf{0.43^{0.38}_{-0.43}}$	Coulex [18]
$4_2^+ \to 2_2^+$	$+2.28^{0.12}_{-0.05}$	$86.6^{9.3}_{-3.8}$	$(+)\mathbf{53^{2.7}_{-1.7}}$	Coulex [18]
			$42(20)$	Coulex [17]
			$26.8(9.2)$	DSAM [17]
			$104(66)$	Coulex [83]
$6_2^+ \to 4_1^+$	$+0.19^{0.03}_{-0.37}$	$0.42^{0.14}_{-0.8}$	$\pm\mathbf{0.58^{0.08}_{-0.1}}$	Coulex [18]
$6_2^+ \to 4_2^+$	$+1.8^{0.2}_{-0.2}$	$37.4^{8.7}_{-8.7}$	$(+)\mathbf{50.4^{5.4}_{-3.4}}$	Coulex [18]
			$42(9)$	DSAM [17]

State	$< I_i\|\|E2\|\|I_f >$ (e.b.) This work	Q_{sp} (e.b.) This work	Q_{sp} (e.b.) Other work	Method
2_2^+	$-0.37^{0.09}_{-0.09}$	$-0.29^{0.07}_{-0.08}$	$-0.30^{0.09}_{-0.03}$	Coulex [18]
			$-0.5(4.5)$	Coulex [83]

Transition	$< I_i\|\|M1\|\|I_f >$ (e.b.)	B(M1)(W.u.)	B(M1) (W.u.)	
$2_2^+ \to 2_1^+$	$0.033^{0.006}_{-0.003}$	$0.032^{0.013}_{-0.006}$	$+\ 0.024^{0.027}_{-0.008}$	Coulex [18]
			$0.02^{0.0.009}_{-0.005}$	$\gamma - \gamma$ DC [87]

element. It is important to note that the 2_2^+ has a M1 contribution. Therefore the M1 matrix element $2_2^+ \to 0_1^+$ polarity must also be changed.
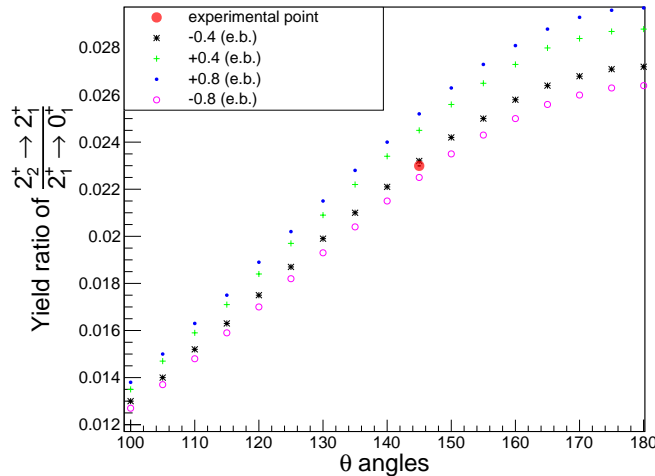
Figure 7.2: The calculated yield ratios between 100-180° for different matrix element values shown by the symbols. The experimental yield ratio is shown by the filled red circle.

7.4   Quadrupole deformation parameters

As explained in Chapter 2.7, the expectation values of the quadrupole rotational invariants $\langle Q^2 \rangle$ and $\langle Q^3 \cos(3\delta) \rangle$ describe the deformation of individual states in both the intrinsic and laboratory frames. This formalism is implemented in the SIGMA code [88, 52] and can be used to determine the quadrupole deformation parameters from the set of matrix elements obtained from the traditional GOSIA analysis.

The $\langle Q^2 \rangle$ invariants calculated in this work and compared to Ref. [18] are illustrated in Fig. 7.3. The $\langle Q^3 \cos(3\delta) \rangle$ invariants are shown in Fig. 7.4. These values are also tabulated in Tab. 7.7. Surprisingly, the $\langle Q^2 \rangle$ invariant of the 2_1^+ state resulting from the present analysis is larger than the value reported in Ref. [18]. This is due to a bigger E2 matrix element corresponding to the $2_2^+ \rightarrow 2_1^+$ transition which was determined in this work. Similarly, the $\langle Q^3 \cos(3\delta) \rangle$ invariant of the 0_1^+ state is larger due to the larger E2 matrix element from the $2_2^+ \rightarrow 0_1^+$ transition.

The current result indicates a rather stable γ deformation along the ground state band with γ between $\approx$ 39-41°. The β value varies between states, for example from the 0_1^+ to the 2_1^+ it changes from $\approx$ 0.14 to 0.17. The obtained results of the $\langle Q^2 \rangle$ parameters for the 2_2^+ and 4_2^+ states are consistent with the literature reported in Ref. [18]. However, the uncertainties of the newly determined values are significantly reduced providing strong constraints on $\langle Q^2 \rangle$. The level of statistics was, however, insufficient to determine the values of the triaxiality parameter for the states in the γ band.

As discussed in Chapter 2, a positive $\langle Q^3 \cos(3\delta) \rangle$ invariant indicates that the nucleus in
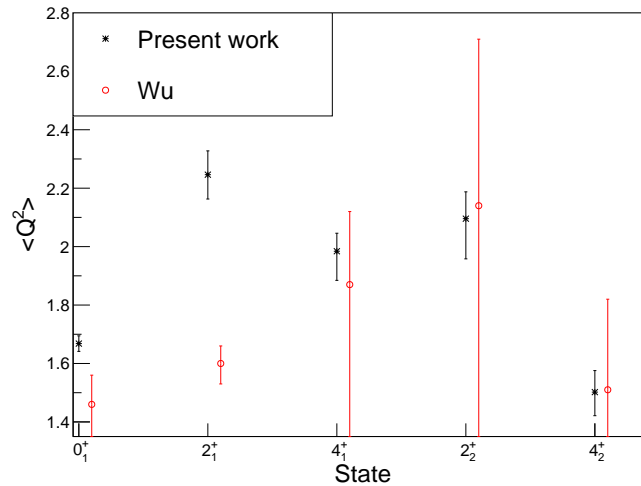
Figure 7.3: $\langle Q^2 \rangle$ invariants determined in this work (black) compared to values obtained in Ref. [18] (red).
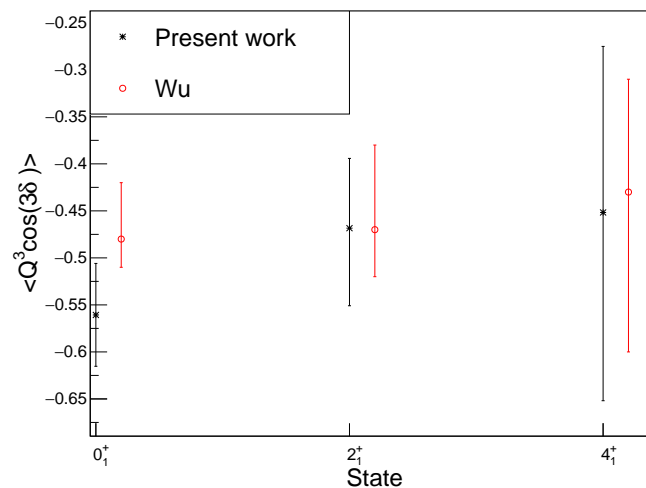
Figure 7.4: $\langle Q^3 \cos(3\delta) \rangle$ invariants determined in this work (black) and compared to values obtained in Ref. [18] (red).

a given state is prolate, negative that it is oblate and zero that it is spherical or maximum triaxial. From the current measurement it can be concluded that ^{194}Pt is triaxial oblate in the 0_1^+, 2_1^+ and 4_1^+ states. This is in agreement with theoretical works from Refs. [6, 7] where it is predicted that Pt evolves from prolate deformed $^{180-186}$Pt to γ-soft ^{188}Pt and triaxial ^{190}Pt to oblate $^{192-198}$Pt to spherical ^{204}Pt.

The $\langle Q^3 \cos(3\delta) \rangle$ and $\langle Q^2 \rangle$ parameters give information on the shape of the charge distribution of the nucleus. The shape of the mass distribution (given by the β and γ deformation parameters) can be approximated from the charge distribution as discussed in Ch. 2. The β deformations of states in ^{194}Pt are shown in Fig. 7.5 and the γ deformation of states are shown in Fig. 7.6. The γ deformation parameter is $\approx 40°$ while the

Table 7.7: β and γ deformation parameters calculated from rotational invariants $\langle Q^2 \rangle$ and $\cos(3\delta)$ for states in ^{194}Pt.

Spin	$\langle Q^2 \rangle / e^2 b^2$	β	$\cos(3\delta)$	$\gamma(°)$
		This work		
0^+_1	$1.67^{0.03}_{-0.03}$	$0.14^{0.1e-2}_{-0.1e-2}$	$-0.56^{0.05}_{-0.05}$	$41.4^{1.3}_{-1.2}$
2^+_1	$2.25^{0.08}_{-0.08}$	$0.17^{0.3e-2}_{-0.3e-2}$	$-0.47^{0.08}_{-0.0742}$	$39.3^{1.6}_{-1.7}$
4^+_1	$1.98^{0.10}_{-0.06}$	$0.16^{0.2e-2}_{-0.4e-2}$	$-0.45^{0.20}_{-0.18}$	$38.9^{4.0}_{-4.0}$
2^+_2	$2.10^{0.14}_{-0.09}$	$0.16^{0.5e-2}_{-0.4e-2}$		
4^+_2	$1.50^{0.08}_{-0.07}$	$0.14^{0.4e-2}_{-0.3e-2}$		
Spin	$\langle Q^2 \rangle / e^2 b^2$	β	$\cos(3\delta)$	$\gamma(°)$
		Wu [18]		
0^+_1	$1.46^{0.12}_{-0.10}$	$0.13^{0.5e-2}_{-0.5e-2}$	$-0.48^{0.03}_{-0.06}$	$39.6^{1.3}_{-0.6}$
2^+_1	$1.56^{0.07}_{-0.06}$	$0.14^{0.3e-2}_{-0.3e-2}$	$-0.47^{0.05}_{-0.09}$	$39.3^{2.0}_{-1.1}$
4^+_1	$1.87^{0.69}_{-0.25}$	$0.15^{0.03}_{-0.01}$	$-0.43^{0.17}_{-0.12}$	$38.4^{2.6}_{-3.5}$
2^+_2	$2.14^{0.82}_{-0.57}$	$0.16^{0.02}_{-0.03}$		
4^+_4	$1.51^{1.46}_{-0.31}$	$0.14^{0.02}_{-0.06}$		

Figure 7.5: β deformation of states in ^{194}Pt. The black data is calculated from the present work and the red data is obtained in Ref. [18].

β deformation varies between 0.14-0.17.

7.4.0.1   Comparison to theoretical models

The HF+BCS γ-deformation calculations for ^{194}Pt [8], shown in Fig. 7.7, has a shallow minimum between ≈ 30-$40°$, which is in good agreement with the results from this work.

The Davydov-Filippov rigid asymmetric rotor model [82, 89] can be used to calculate
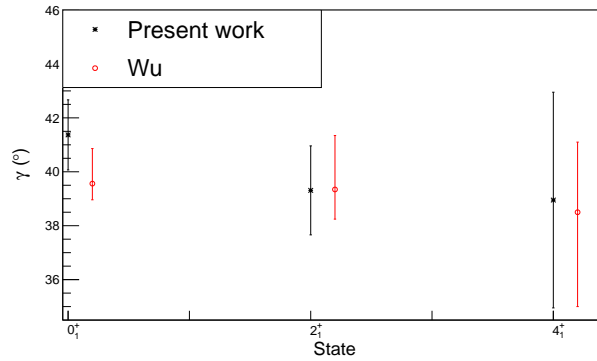
Figure 7.6: γ deformation parameters for states in ^{194}Pt. The black data is calculated from the present work and the red data is obtained from Ref. [18].
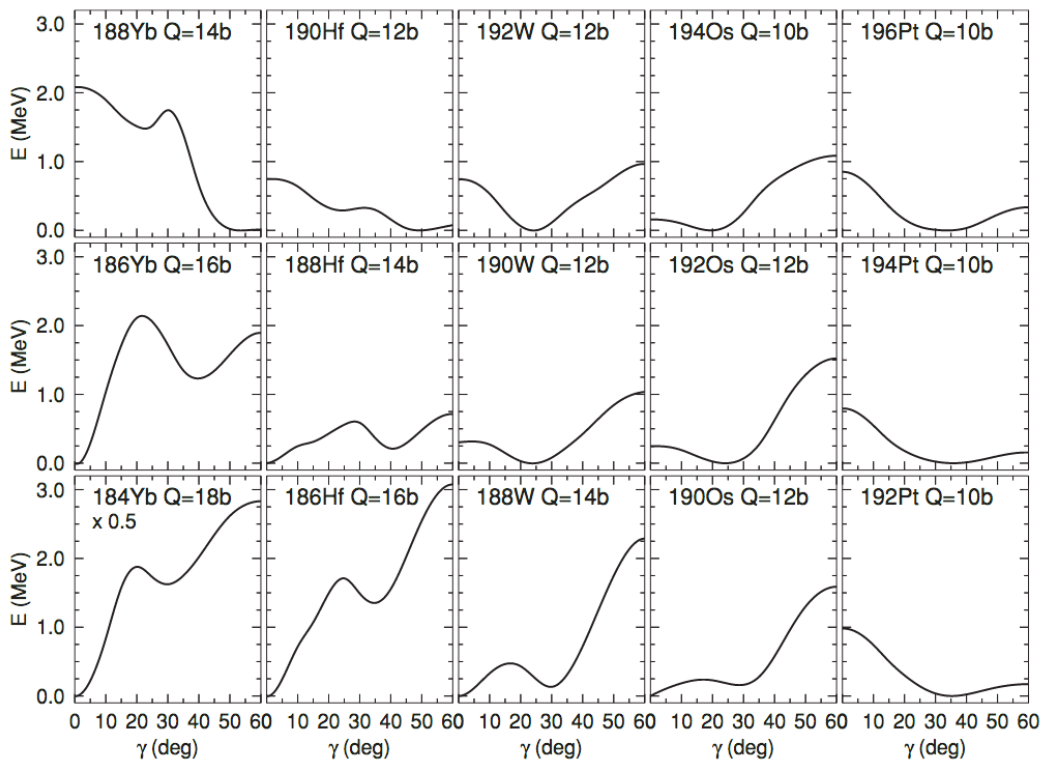
Figure 7.7: HF+BCS calculations of γ deformation parameters [8] for isotopes of Yb, Hf, W, Os and Pt. The γ deformation of ^{194}Pt has a minimum between 30° - 40°, indicating that ^{194}Pt is triaxial oblate.

energies of states, reduced matrix elements and deformation of states in even-even nuclei.

This model was applied to the 2_1^+ and 2_2^+ states of ^{194}Pt. The matrix element for the transition $2_1^+ \rightarrow 0_1^+$ from Ref. [18] was given as an input parameter. The γ deformation parameter and matrix elements obtained are shown in Tabs 7.8 and 7.9. Overall they are in good agreement and follow the trends of the results obtained from the GOSIA analysis, providing additional confidence in the accuracy of the work.

Table 7.8: Davydov-Filippov calculations compared to the Coulomb excitation analysis results for the deformation parameters for the 2_1^+ state.

Deformation parameter	GOSIA analysis	Davydov-Filippov
$\gamma(°)$	$39.4^{1.6}_{-1.7}$	32.6
β	$0.170^{0.003}_{-0.003}$	0.15

Table 7.9: Davydov-Filippov calculations compared to the Coulomb excitation analysis results for the selected transitional matrix elements ($2_1^+ \rightarrow 0_1^+$ and $2_2^+ \rightarrow 2_1^+$) and diagonal matrix elements (2_1^+ and 2_2^+).

Transition	GOSIA analysis	Davydov-Filippov
$2_1^+ \rightarrow 0_1^+$	$1.29^{0.01}_{-0.01}$	1.3
$2_2^+ \rightarrow 2_1^+$	$2.01^{0.05}_{-0.05}$	1.49
Level	GOSIA analysis	Davydov-Filippov
2_1^+	$0.52^{0.07}_{-0.07}$	0.52
2_2^+	$-0.40^{0.09}_{-0.09}$	-0.52

Chapter 8

Conclusion

8.1 ^{194}Pt

The Coulomb excitation of the $2_1^+, 4_1^+, 6_1^+, 2_2^+$ and 4_2^+ states of ^{194}Pt were observed in $p - \gamma$ coincidences. The matrix elements of these states' transitions were determined and they agree overall with previous measurements from Refs. [11, 12, 13, 14, 15, 16, 17]. Although no new matrix elements were calculated, the uncertainties are lowered for some of the transitions providing significant constraints. The matrix elements of the $2_1^+ \rightarrow 0_1^+$ and $6_1^+ \rightarrow 4_1^+$ transitions are measured with increased precision compared to previous measurements. The obtained values of Q_{sp} of the 2_1^+ and 4_1^+ states are very well reproduced in the present analysis. The value of the $\mathrm{Q}_{sp}(2_2^+)$ has been obtained with a reduced uncertainty in comparison to the previous values from Refs. [18, 82]. The reduced matrix elements obtained for the 2_1^+ states' relevant transitions from this work also agree with the Davydov-Filippov theoretical results and trends.

From the quadrupole invariant parameters $< Q^3 \cos(3\delta) >$ and γ deformation parameter extracted from this measurement, it can be concluded that ^{194}Pt is triaxial oblate in the 0_1^+, 2_1^+ and 4_1^+ states. The overall $\gamma \sim 40°$ deformations obtained from this work are in good agreement with the theoretically calculated $\gamma \sim 30 - 40°$ from Refs. [6, 7, 8] and the Davydov-Filippov calculation.

From the quadrupole invariant parameters $< Q^2 >$ and β deformation parameters it can be concluded that ^{194}Pt is deformed in the 0_1^+, 2_1^+ and 4_1^+ states. The β deformation in the range of 0.13-0.17 obtained from this work is in good agreement with the Davydov-Filippov calculation of 0.15.

The deformation parameters obtained in this work supports the prediction of Pt isotopes evolving from prolate deformed $^{180-186}$Pt to γ-soft ^{188}Pt and triaxial ^{190}Pt to oblate

$^{192-198}$Pt to spherical ^{204}Pt.

8.2 ^{14}C

In Ref. [90] the authors report on a ^{194}Pt(^{12}C,^{12}C')^{194}Pt' Coulomb excitation reaction performed at the TRIUMF laboratory in Canada. This measurement was performed using the TIGRESS array [91, 92] coupled to the silicon particle detector placed at forward angles. After 72 hours of data taking with the beam intensity of 5×10^8 pps, approximately 1150 counts were observed in the 4.4 MeV peak corresponding to the $2_1^+ \rightarrow 0_1^+$ transition with an estimated absolute efficiency of 1.6% at 4.4 MeV.

An attempt to extrapolate the measured cross section from Ref. [90] to the excitation energy of 7 MeV for the experimental setup presented in this work is shown in Tab. 8.1. The beam current, absolute efficiency, target thickness, beam time, B(E2: $2_1^+ \rightarrow 0_1^+$) and angular coverage are compared. Taking all these experimental factors into account an estimated 900 ($\approx$ 50 per day) counts are expected in the γ-ray decay of the 2_1^+ state of ^{14}C.

Table 8.1: The experimental properties from Ref. [90] are compared to the current experimental setup.

Property	Ref. [90]	Present work
Beam current (pps)	5×10^8	1.8×10^{10}
Absolute efficiency (%)	1.6 (at 4.4 MeV)	0.18 (at 7 MeV)
Target thickness (mg/cm^2)	3	2
Beam time (days)	3	17
Angular coverage	31-60°	132-159°
B(E2: $2_1^+ \rightarrow 0_1^+$) (e^{2}fm^4)	8 (for ^{12}C)	4 (for ^{14}C)
	Ref. [90]	Present work
Count estimate	1150 (at 4.4 MeV)	$\approx$ 900 (at 7 MeV)

The Coulomb excitation of ^{14}C was not observed in the $p - \gamma$ coincidence data. The software developed to analyse the data was extensively tested and exhaustive measures where taken to ensure that ^{14}C is indeed not populated in the excited states. Many factors play a role in the observation of ^{14}C and identifying one is difficult. It seems possible that the B(E2: $2_1^+ \rightarrow 0_1^+$) value calculated from the previously reported width [3] is not accurate. It could indicate a strong single-particle character of the 2_1^+ state at 7.01 MeV with a much reduced B(E2: $2_1^+ \rightarrow 0_1^+$). The B(E2: $2_1^+ \rightarrow 0_1^+$) of even-even Z=6 isotopes
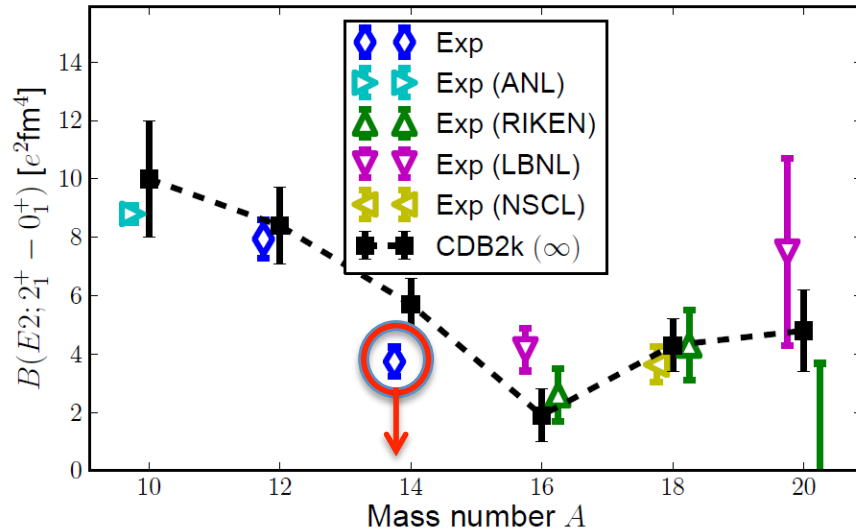
Figure 8.1: No-core shell model calculations (black data points connected by a dashed line) of even-even Carbon isotopes Ref. [33]. The B(E2: $2_1^+ \to 0_1^+$) value in ^{14}C is highlighted. The current Coulomb excitation results suggest that this value could be smaller than indicated.
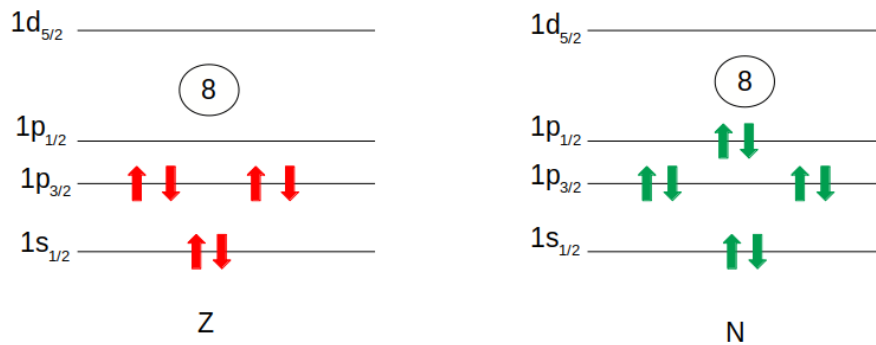
Figure 8.2: A possible representation of the filling scheme for neutrons and protons of ^{14}C.

are shown again in Fig. 8.1.

In its ground state ^{14}C has a filled neutron shell with N=8, and a filled $1p_{3/2}$ orbit with Z=6, just two protons short of a filled Z=8 shell. The filled orbitals for the ground state of ^{14}C are presented in Fig. 8.2. It can be speculated that ^{14}C should be the most spherical-like (and correspondingly, have the smallest B(E2: $2_1^+ \to 0_1^+$)) of the Z=6 isotopes, because it is the closest to having two filled shells.

A smaller B(E2: $2_1^+ \to 0_1^+$) will indicate that ^{14}C is not collective and theoretical works from Refs. [31, 33] suggest that the 2_1^+ state of ^{14}C is dominated by protons. This means a particle-hole excitation of the protons from the p3/2 to the p1/2 state is required to populate the 2_1^+ state.
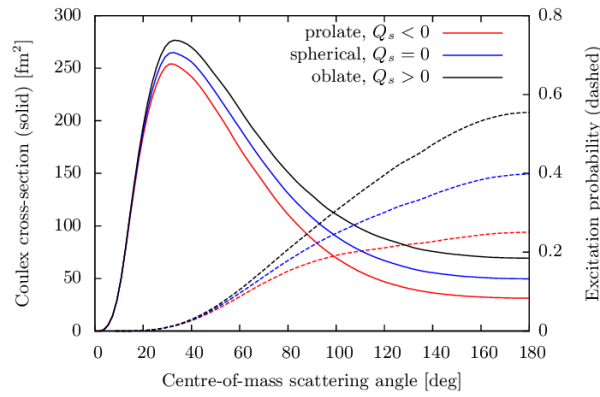
Figure 8.3: Coulomb excitation probabilities are shown by dashed lines and the product of the Coulomb excitation probability and the Rutherford cross section taken directly from [93] is shown by the solid line for ^{120}Sn(^{184}Hg,^{184}Hg')^{120}Sn'.

8.2.1 Future outlook

A significant amount of information is obtained to pave the way for a future measurement of the B(E2: $2_1^+ \rightarrow 0_1^+$) value of ^{14}C. Another attempt can be made to Coulomb excite ^{14}C in improved experimental conditions. General experimental conditions that should be considered are:

- The Coulomb fore is $\propto$ Z and by using a heavier target like ^{208}Pb, the cross-section will increase compared to a ^{194}Pt target.

- The angular dependence of the scattered particle is $\propto \sin^4(\theta/2)$ and will have a large impact on the cross section. For example the product of the Coulomb excitation probability and the Rutherford cross section from Ref. [93] is shown by the solid line for ^{120}Sn(^{184}Hg,^{184}Hg')^{120}Sn' in Fig. 8.3. A particle detector at forward angles will increase the particle efficiency, however the large amount of particles scattering forward will damage a particle detector over time.

- The interaction time for back-scattered particles are longer and have a larger excitation probability as shown by the dashed line in Fig. 8.3. Detecting a large amount of particles that are not Coulomb excited is not useful, similarly detecting too few particles is not useful. A compromise between excitation probability and the probability to detect a particle is needed.

- More γ-ray detectors closer to the target can increase the efficiency, however the increased solid angle will also increase the Doppler broadening which may be detrimental to identify decays from weakly populated high-lying states.

Taking the general experimental condition improvements into account, possible detector scenarios at iThemba LABS are:

1. A possible measurement scenario is to detect particles and γ-rays in coincidence. For example, a Si particle detector at forward angles and the 23 large volume $LaBr_3(Ce)$ detectors of the African $LaBr_3(Ce)$ Array, ALBA which is projected to be fully operational in 2020. The efficiency will be greatly increased due to the increase in the number of γ-ray detectors and by having a particle detector at $\theta_{lab} = 60 - 80°$ would be a good compromise between cross section and Coulomb excitation probability.

2. Another possible measurement scenario is to use a magnetic spectrometer to detect the amount of particles excited to the 2_1^+ state. For example, this can be performed with the K600 magnetic spectrometer [94] at iThemba LABS with a ^{14}C target or at FSU with the same ^{194}Pt target and ^{14}C beam. From the particle excitation the number of particles which have been Coulomb excited to the 2_1^+ state can be directly measured. From this the B(E2: $2_1^+ \rightarrow 0_1^+$) value can be calculated.

3. By including some γ-ray detectors along with a spectrometer p-γ coincidences can also be made, however this is not necessarily required. For example, this can be performed with the K600 magnetic spectrometer [94] at 0° coupled to HPGe and $LaBr_3(Ce)$ detectors. In this scenario, the experiment can run with digital electronics in a trigger-less mode detecting single particles and p-γ coincidences. The challenge of using a spectrometer is that with the current experimental setup at iThemba and FSU, the focal-plane detector of the magnetic spectrometer is in air and not effective with heavy particles. The current development at the K600 on low pressure gaseous detectors will enable the effective detection of Z=6 particles, albeit projected to be completed in 2020.

A ^{14}C target with the heaviest beam available is a possible beam and target combination. Coulomb excitation is related to Z and the heaviest ion beam available at iThemba LABS is Xe (Z=54). With sufficient intensity and measurement duration a Xe beam and ^{14}C target can still be utilized with measurement scenario 1. Another beam and target combination is a ^{14}C beam and heavy target, for example ^{208}Pb, as mentioned earlier. This will provide a larger Coulomb excitation cross section due to the high Z of the target. In general it is easier to accelerate a stable smaller nucleus to higher intensities. It may be possible to procure a ^{14}C beam at iThemba LABS by using CO_2 ^{14}C enriched gas, however ^{14}C is not stable and the radiation safety concerns must first be addressed. During the experiment ^{14}C residue can contaminate the beam line, magnets etc. and with a half life of 5700 years this produces a dangerous work environment. This combination of beam and target can be used with either scenario 1 or 2.

If the B(E2: $2_1^+ \rightarrow 0_1^+$) is smaller as this work suggests, it would mean the lifetime is larger than the reported 9 fs. This makes the direct lifetime measurement of the 2_1^+ possible with the Doppler shift attenuation method. The B(E2: $2_1^+ \rightarrow 0_1^+$) can then be calculated from the lifetime. This approach still has the deal with the low efficiency of γ-ray detectors at 7 MeV. An attempt to measure the lifetime has been made with the Doppler shift attenuation method in Refs. [95, 96] and only upper limits of <7 fs and <120 fs could be obtained. Due to the expected short lifetime and inefficient γ-ray detection at 7 MeV, this approach is not trivial.

Whatever approach is used, it is clear that experimental information on ^{14}C is highly desirable as it will provide a critical piece for a complete understanding of the structural evolution of the carbon isotopic chain.

Chapter 9

Summary

The experiment was setup and performed at Florida State University for the following experimental measurements:

- Safe Coulomb excitation reactions: ^{194}Pt(^{14}C,^{14}C')^{194}Pt and ^{194}Pt(^{12}C,^{12}C')^{194}Pt.

- γ-ray calibration up to 4.8 MeV: ^{nat}Zn(p,x)^{xx}Ga reaction.

- γ-ray calibration and absolute efficiency up to 7.01 MeV: ^{13}C(d,p)^{14}C transfer reaction.

The C++/ROOT software used to analyse the data was developed and tested successfully.

Unfortunately no excitation of states in ^{14}C is observed in the $p - \gamma$ coincidence data. This is confirmed by the simulated response function of the LaBr$_3$(Ce) material to the interaction of a Doppler shifted $2_1^+ \rightarrow 0_1^+$ transition of ^{14}C using GEANT4. This could indicate that the 2_1^+ state of ^{14}C is not very collective, but shows strong single-particle character and that the lifetime should be longer than the previously reported one in Ref. [3]. The information obtained in this study will be very useful for any future attempts to measure the B(E2: $2_1^+ \rightarrow 0_1^+$).

Simultaneously, many states in ^{194}Pt are successfully excited. From the Coulomb excitation of ^{194}Pt a rich set of matrix elements were deduced. The matrix elements of the $2_1^+ \rightarrow 0_1^+$ and $6_1^+ \rightarrow 4_1^+$ transitions and the $Q_{sp}(2_2^+)$ are measured with increased precision. Deformation parameters $\gamma \sim 40°$ and $\beta \sim 0.13 - 0.17$ have been obtained and are in general agreement with other theoretical and experimental work. From the current measurements it can be concluded that ^{194}Pt is triaxial oblate. This is in agreement with theoretical work from [6, 7] using Beyond Mean Field, Hartree-Fock-Bogoliubov and Interactive Boson Model studies that predict the evolution of Pt from prolate deformed $^{180-186}$Pt to γ-soft ^{188}Pt and triaxial ^{190}Pt to oblate $^{192-198}$Pt to spherical ^{204}Pt.

Appendices

Appendix A

GOSIA inputs

The individual GOSIA options (the commands given in capital letters) and their explanation can be found in Ref. [20]. The input files used in the GOSIA analysis with brief comments are given here for reproduction purposes.

The GOSIA input: Minimization is used when fitting the matrix elements to the experimental Coulomb excitation yields. This input file contains the additional spectroscopic information discussed in Ch. 7 that is used to constrain the fit. The GOSIA input: Yields contain the efficiency corrected experimental yields.

A.1   GOSIA input: Minimization

```
OP,FILE
22 3 1 !Output file
194pt_mini.out
9 3 1 !Output: OP,GDET (GE detector information (solid angle attenuation
   ↪ factors)). Input: OP, YIEL, OP, INTI, OP, MAP, OP, MINI, OP, ERRO[
   ↪ diagonal, corr]
gdet.f9
8 3 1 !Output: OP,GDET (if first value in OP,GDET is negative) Input: OP,
   ↪  RAW
gdet.f8
7 3 1 !Output:OP, MAP. Input: OP, MINI, OP, ERRO[diagonal, corr]
map.f7
3 3 1
194Pt.yield
4 3 1 !Output: OP, CORR. Input: OP, MAP, OP, MINI, OP, ERRO[ diagonal,
   ↪ corr]
```

```
194Pt.corr
12 3 1 !Output: OP, MINI, Input: OP,ERRO[diagonal, corr]
194Pt.me
0 0 0 !end of the current command
OP,TITL !This creates the title of the experiment
14C beam on 194Pt target
OP,GOSI !GOSIA Information about the nucleus, same syntax as OP,COUL
LEVE !Level scheme:index, parity, spin, energy (MeV)
1,1,0,0.0
2,1,2,0.328
3,1,4,0.811
4,1,6,1.41181
5,1,8,2.09953
6,1,2,0.622
7,1,4,1.229487
8,1,6,1.925
0,0,0,0!End of the current command
ME !Matrix elements: final level, initial level, ME, lower limit, upper
    ↪ limit
2 0 0 0 0 !E2 transitions
1 2 1.208 0.0001 2.0
1 6 0.0888 -3.0 3.0
2 2 0.54 -3.0 3.0
2 3 1.935 0.0001 3.0
2 6 1.517 0.0001 3.0
2 7 0.25 -3.0 3.0
3 3 1.00 -3.0 3.0
3 4 2.90 0.0001 4.0
3 6 0.25 -3.0 3.0
3 7 1.51 -3.0 3.0
3 8 0.224 -3.0 3.0
4 4 0.28 -3.0 3.0
4 5 3.08 0.0001 4.0
4 7 0.16 -3.0 3.0
4 8 1.14 -3.0 3.0
6 6 -0.4 -3.0 3.0
6 7 1.784 0.0001 3.0
7 7 -0.07 -3.0 3.0
```

```
7 8 2.09 0.0001 3.0
7 0 0 0 0 !M1 transitions
2 6 0.028 -3.0 3.0
3 7 0.19 -3.0 3.0
0 0 0 0 0 !End of the current command
EXPT !Experimental parameters
2 78 194 !number of experiments, Z, A
6 14 43.75 152 3 1 0 0 360 0 1 !Zn, An, Ep, th_lab, Mc, Ma, IAX, phi1,
    ↪ phi2, IKIN, LN
6 14 43.75 138 3 1 0 0 360 0 2 !Zn, An, Ep, th_lab, Mc, Ma, IAX, phi1,
    ↪ phi2, IKIN, LN
CONT !Control keys for printing the output
INT,2.
1,1000
2,1000
SPL,1.
EFF,2.
1,0
2,0
CRF,
LCK,
0 0
WRN,3.
PRT,
0 0
END,

OP,YIEL !Yields
    0
    20 4 !number of energies, multipolarity
    0.1 0.2 0.3 0.4 0.5 0.6 0.7 0.8 0.9 1 1.1 1.2 1.3 1.4 1.5 1.6 1.7 1.8
        ↪  1.9 2.0 !energy mesh points
    1 !E1
    0.41 0.070 0.0261 0.0134 0.00826 0.00566 0.00416 0.00321 0.00257
        ↪ 0.00212 0.00178 0.001546 0.001385 0.001282 0.001218 0.001182
        ↪ 0.001165 0.001162 0.001170 0.001185 !Internal conversion
        ↪ coefficients for different multipolarities.
    2 !E2
```

4.90 0.359 0.098 0.0438 0.0248 0.01610 0.01143 0.00860 0.00676
    ↪ 0.00547 0.00454 0.00384 0.00331 0.00291 0.00259 0.00234 0.00214
    ↪ 0.00198 0.00186 0.001754 !Internal conversion coefficients for
    ↪ different multipolarities.
3 !E3
117.9 3.04 0.494 0.1651 0.0787 0.0457 0.0299 0.0212 0.01593 0.01244
    ↪ 0.01001 0.00825 0.00694 0.00593 0.00515 0.00452 0.00402 0.00361
    ↪ 0.00328 0.0030 !Internal conversion coefficients for different
    ↪ multipolarities.
7 !M1
6.67 0.934 0.30 0.1407 0.0780 0.0484 0.0325 0.0231 0.01710 0.01309
    ↪ 0.01029 0.00827 0.00679 0.00568 0.00483 0.00418 0.00368 0.00328
    ↪ 0.00297 0.00272 !Internal conversion coefficients for
    ↪ different multipolarities.
4,4 !number of detectors for each experiment
1 2 3 4 !Detector ID for exp1
90 180 180 90 !Theta
299 311 49 28 !Phi
1 2 3 4 !Detector ID for exp2
90 180 180 90 !Theta
299 311 49 28 !Phi
2 1 !for normalisation
1 !EXP1
0.100
1
1 !EXP2
0.100
1
4
5 1.0 !branching ratios: initial state, final_1, initial state,
    ↪ final_2, branching ratio, error
    6 1 6 2 0.1369 0.023
    7 3 7 6 0.144 0.014
    7 2 7 6 0.122 0.008
    8 3 8 7 0.12 0.04
    8 4 8 7 0.06 0.04
7 1.0 !Life times: state index, lifetime (ps) uncertainty
    2 60.46 0.87

```
        3 5.34 0.29
        4 2.31 0.72
        5 1.59 0.43
        6 50.5 5.8
        7 5.5 0.9
        8 1.88 0.29
    1 1.0 !Mixing ratios: Initial state, final state, mixing ratio,
      ↪ uncertainty
        6 2 15.0 2.0
    5 1.0 !Known matrix elements: multipole, Initial state, final state,
      ↪ matrix element, uncertainty
        2 2 2 0.54 0.07
        2 3 3 1.00 0.13
        2 4 4 0.28 0.20
        2 6 6 -0.40 0.09
        2 7 7 -0.07 0.14
OP,RAW ! Raw, uncorrected gamma yields, i.e. yields not corrected for
    ↪ detector efficiencies.
1
0 0 0 0 0 0 -50 0
0 0 0 0 0 0 -50 0
0 0 0 0 0 0 -50 0
0 0 0 0 0 0 -50 0
1
4
1 2 3 4
2
0 0 0 0 0 0 -50 0
0 0 0 0 0 0 -50 0
0 0 0 0 0 0 -50 0
0 0 0 0 0 0 -50 0
1
4
1 2 3 4
0
OP,REST
0,0
OP,MINI !IMODE, NPTL, CHILIM, CONV, TEST, LOCKF, NLOCK, IFBL, LOCKS,DLOCK
```

```
2100,50,0.000001,0.000001,1.1,1,0,1,0,0.00001
OP,EXIT
```

A.2   GOSIA input: yields

```
1 1 78 194 45 5 1.0 !Experiment ID, Z, A, beam energy, number of yields
2 1 2224350 111217 !final state, initial state, efficiency corrected
    ↪ counts, error
3 2 77045 7705
4 3 611 31
6 2 63007 3150
7 6 2797 140
2 1 78 194 45 5 1.0 !Experiment ID, Z, A, beam energy, number of yields
2 1 2501341 125067 !final state, initial state, efficiency corrected
    ↪ counts, error
3 2 77461 7746
4 3 723 36
6 2 61244 3062
7 6 3147 157
```

Bibliography

[1] "National nuclear data center," (Accessed 2019-1-12), `www.nndc.bnl.gov`.

[2] Projects IQ, (Accessed 2019-03-20), `http://fsunuc.physics.fsu.edu/nrb\_model/nrb\_model.html`.

[3] H. Crannell *et al.*, Proc. Int. Conf. Nucl. Struct. (1972), Sendai, Japan, K. Shoda, H. Ui, Eds., Res. Rep. Lab. Nucl. Sci. Tohoku Univ. 5, Suppl. 375.

[4] H. Ikuko and B. Mottelson, arXiv e-print **arXiv:1107.5248v2** (2012).

[5] L. Roblede, R. Rodríguez-Guzmán, and P. Sarriguren, J. Phys. G: Nucl. Part. Phys. **36**, 115104 (2009).

[6] K. Nomura *et al.*, Phys. Rev. **C 83**, 014309 (2011).

[7] P. R. John *et al.*, Phys. Rev. **C 90**, 021301 (2017).

[8] P. Sarriguren, R. Rodríguez-Guzmán, and L. Roblede, Phys. Rev. **C 77**, 064322 (2008).

[9] P. R. John *et al.*, Phys. Rev. **C 95**, 064321 (2014).

[10] I. Hamamoto and B. R. Mottelson, Phys. Rev. **C 79**, 034317 (2009).

[11] S. Raman, C. W. Nestor, and P. Tikkanen, At. Data Nucl. Data Tables **78**, 1 (2001).

[12] N. Johnson *et al.*, Phys. Rev. **C 15**, 1325 (1977).

[13] W. Milner *et al.*, Nucl. Phys. **A 177**, 1 (1972).

[14] J. Glenn, R. Pryor, and J. Saladin, Phys. Rev. **188**, 1905 (1969).

[15] I. Berkes *et al.*, Phys. Rev. **C 6**, 1098 (1972).

[16] F. Baker *et al.*, Phys. Rev. Lett **37**, 193 (1976).

[17] K. Stelzer *et al.*, Phys. Lett. **B 70**, 297 (1977).

[18] C. Wu *et al.*, Nucl. Phys. **A 607**, 178 (1996).

[19] D. C. T. Czosnyka and C. Wu, Bull. Am. Phys. Soc. **28**, 745 (1983).

[20] D. Cline *et al.*, *GOSIA user manual for simulation and analysis of coulomb excitation experiments* (University of Rochester, 2012).

[21] N. Imai *et al.*, Phys. Rev. Lett. **92**, 062501 (2004).

[22] Z. Elekes *et al.*, Phys. Lett. **B586**, 34 (2004).

[23] H. Ong *et al.*, Phys. Rev. **C 73**, 024610 (2006).

[24] M. Wiedeking *et al.*, Phys. Rev. Lett. **100**, 0152501 (2008).

[25] M. Petri *et al.*, Phys. Rev. **C 86**, 044329 (2012).

[26] H. Ong *et al.*, Phys. Rev. **C 78**, 014308 (2008).

[27] A. Wousmaa *et al.*, Phys. Rev. Lett **105**, 132501 (2010).

[28] P. Voss *et al.*, Phys. Rev. **C 86**, 011303(R) (2012).

[29] M. Petri *et al.*, Phys. Rev. Lett. **107**, 102501 (2011).

[30] H. Sagawa *et al.*, Phys. Rev. **C 70**, 054316 (2004).

[31] A. Macchiavelli *et al.*, Phys. Rev. **C 90**, 067305 (2014).

[32] H. Ma *et al.*, Phys. Lett. **B 688**, 150 (2010).

[33] C. Forssen *et al.*, J. Phys. **G 40**, 055105 (2013).

[34] A. Winther and K. Alder, *Coulomb Excitation* (Academic, New York, 1966).

[35] K. Alder and A. Winther, *Electromagnetic Excitation, Theory of Coulomb Excitation with Heavy Ions* (North Holland, Amsterdam, 1975).

[36] D. Rowe and J. Wood, *Fundamentals of Nulcear Models*, 1st ed. (World Scientific, 2010).

[37] K. Krane, *Introductory Nuclear Physics* (John Wiley and sons, 1988).

[38] A. Messiah, *Quantum Mechanics*, 2nd ed. (North Holand, 1965).

[39] E. Ha and D. Cha, Phys. Rev. **C 75**, 057304 (2007).

[40] M. Klintefjord *et al.*, Phys. Rev. C **93**, 054303 (2016).

[41] S. Sels *et al.*, Phys. Rev. C **99**, 044306 (2019).

[42] P. Delaroche *et al.*, Phys. Rev. C **81**, 014303 (2010).

[43] K. Kitao *et al.*, Nucl. Data Sheets **96**, 241 (2002).

[44] B. Singh and J. Chen, Nucl. Data Sheets **147**, 1 (2018).

[45] F. McGowan, Proc. of the Heavy-ion summer study group. **1**, 38 (1969), oak Ridge National Laboratory.

[46] A. Bohr and B. Mottelson, *Nuclear Structure* (Benjamin, New York, 1969).

[47] E. P. Wigner, The collected works of Eugene Paul Wigner , 608 (1951).

[48] A. J. Ferguson, *Angular correlation methods in gamma-ray spectroscopy* (North Holland Publishing Company, 1965).

[49] D. Griffiths, *Introduction to electrodynamics*, 3rd ed. (Pearson Benjamin Cummings, 2008).

[50] K. Hadyńska-Klęk, *Badanie struktury kolektywnej w izotopach wapnia metodą wzbudzeń kulombowskich*, Ph.D. thesis, University of Warsaw (2013).

[51] K. Kumar, Phys. Rev. Lett. **28**, 249 (1972).

[52] D. Cline, Annu. Rev. Nucl. Part. Sci. **36**, 683 (1986).

[53] J. Srebrny and D. Cline, Int. J. Mod. Phys. **E 20**, 422 (2011).

[54] G. Caskey *et al.*, Nucl. Instr. and Methods **157**, 1 (1978).

[55] Florida State University, (Accessed 2018-12-07), `http://fsunuc.physics.fsu.edu/nrb\_model/nrb\_model.html`.

[56] XIA, Instruments That Advance The Art, (Accessed 2019-07-27), `www.xia.com/dgf_pixie-16.html`.

[57] CAEN, *Digital Pulse Processing in Nuclear Physics* (2001), `https://www.caen.it//documents/News/32/WP2081_digitalpulseprocessing_03.pdf`.

[58] Micron Semiconductor Ltd, (Accessed 2019-06-01), `www.micronsemiconductor.co.uk/product/s3`.

[59] G. Knoll, *Radiation detection and measurement*, 4th ed. (John Wiley and sons, 2010).

[60] Lab-training, (Accessed 2018-12-07), `Lab-Training.com`.

[61] A. Lavagno, G. Gervino, and A. Scarfone, Nucl. Meth. in Phys. Res. Sec. **A 718**, 504 (2013).

[62] M. Zhuravleva *et al.*, IEEE Nuclear Science Symposium Conference Record (2013), 10.1109/NSSMIC.2013.6829669.

[63] Physics and Radio-Electronics, (Accessed 2018-12-07), `http://www.physics-and-radio-electronics.com/electronic-devices-and-circuits/semiconductor/hole.html`.

[64] Semesters In, (Accessed 2018-12-07), `http://semesters.in/v-i-characteristics-of-p-n-junction-diode-notes-for-electronics-engineering-1st-year`.

[65] R. Brun and F. Rademakers, Proceedings, AIHENP'96 Workshop, Lausanne, Sep. 1996, Nucl. Inst. and Meth. in Phys. Res **A 389**, 81 (1997).

[66] A. Artna-Cohen, Nucl. Data Sheets **79**, 1 (1996), data extracted from the ENSDF database.

[67] C. Baglin *et al.*, Nucl. Instrum. and Meth. in Phys. Res. Sec. **A 481**, 365 (2002).

[68] F. Ajzenberg-Selove, J. H. Kelley, and C. D. Nesaraja, Nucl. Phys. **A 523** (1991).

[69] P. R. Menge *et al.*, Nucl. Instrum. and Methods in Phys. Res. **A 579**, 6 (2007).

[70] R. Lasseri and A. Mogini, NPAC lab projects (2014).

[71] R. Rosson, J. Lahr, and B. Kahn, Health Phys. **101**, 703 (2011).

[72] A. Owens *et al.*, Nucl. Instr. Meth. **A 574**, 110 (2007).

[73] K. Mathieson *et al.*, Nucl. Instrum. and Methods in Phys. Res. **A 487**, 113 (2002).

[74] J. H. Kelley and C. G. Sheu, Nucl. Phys. **A 880** (2012).

[75] Cambridge Isotope Laboratories Inc., (Accessed 2019-07-06), `https://www.eurisotop.com`.

[76] S. Agostinelli *et al.*, Nucl. Instr. and Methods in Phys. Res. **A 506**, 250 (2003).

[77] A. Allison *et al.*, IEEE Transactions on Nuclear Science **53**, 270 (2006).

[78] J. Allison *et al.*, Nucl. Instrum. and Methods in Phys. Res. **A 835**, 186 (2016).

[79] S. Ross, *A first course in probability*, 8th ed. (Pearson education, 2010).

[80] R. Nord, *Recoil-distance measurement*, Ph.D. thesis, Univ. of Wisconsin (1971).

[81] B. Singh, Nucl. Data Sheets **107**, 1531 (2006), data extracted from the ENSDF database, revision of April 2006.

[82] A. Davydov and G. Filippov, Nucl. Phys. **8**, 237 (1958).

[83] C. Baktash *et al.*, Phys. Rev. **C 18**, 131 (1978).

[84] W. Milner *et al.*, Nucl. Phys. **A 177** (1971).

[85] J. Sprinkle *et al.*, Bull. Amer. Phys. Soc. **22**, 545 (1977).

[86] G. Gyapong *et al.*, Nucl. Phys. **A 458**, 165 (1986).

[87] K. Krane and R. Steffen, Phys. Rev. **C 3**, 240 (1971).

[88] D. Cline and C. Flaum, Proc. Int. Conf. on Nucl. Struct. Studies using Electron Scatt. and Photoreaction, Sendai (1972), k. Shoda and H. Ui (eds.) Tohoku Univ.

[89] L. Proćhniak and P. Napiorkowski, HIL Annual Report 2015 , 82 (2016).

[90] M. K. Raju *et al.*, Phys. Lett. **B 777**, 250 (2018).

[91] G. Ball *et al.*, Nucl. Phys. **A 787**, 118 (2007).

[92] H. Scraggs *et al.*, Nucl. Instrum. and Meth. in Phys. Res. Sec. A **543**, 431 (2005).

[93] M. Zielińska *et al.*, Eur. Phys. Jour. **A 52**, 99 (2016).

[94] R. Neveling *et al.*, Nucl. Instrum. and Meth. in Phys. Res. **A 29**, 654 (2011).

[95] M. Throop, Phys. Rev. **179**, 1011 (1969).

[96] J. H. H. Grawe and K. Kandler, Z. Phys. **A276**, 351 (1976).